Gesellschaft für Anlagen- und Reaktorsicherheit (GRS) gGmbH

Schwertnergasse 1
50667 Köln
Telefon +49 221 2068-0
Telefax +49 221 2068-888

Boltzmannstraße 14
85748 Garching b. München
Telefon +49 89 32004-0
Telefax +49 89 32004-300

Kurfürstendamm 200
10719 Berlin
Telefon +49 30 88589-0
Telefax +49 30 88589-111

Theodor-Heuss-Straße 4
38122 Braunschweig
Telefon +49 531 8012-0
Telefax +49 531 8012-200

www.grs.de

ISBN 978-3-910548-41-1

Gesellschaft für Anlagen-
und Reaktorsicherheit
(GRS) gGmbH

HYMNE

Hydrogeological Modelling at a Regional Scale

Anke Schneider (GRS)
Niklas Conen (G-CSC)
Anne Gehrke (GRS)
Julian Hilbert (G-CSC)
Markus Knodel (G-CSC)
Klaus-Peter Kröhn (GRS)
Michael Lampe (TechSim)
Lukas Larisch (TechSim)
Babett Lemke (G-CSC)
Arne Nägel (G-CSC)
Tim Schön (G-CSC)
Felix Salfelder (TechSim)
Martin Stepniewski (G-CSC)
Gabriel Wittum (G-CSC)
Hong Zhao (GRS)

November 2023

Remark:

This report refers to the research project contract No. 02E11809A-B which has been funded by the German Federal Ministry for Economic Affairs and Energy (BMWi).

The work was conducted by Gesellschaft für Anlagen- und Reaktorsicherheit (GRS), the Goethe Center for Scientific Computing of the Goethe University Frankfurt (G-CSC) and TechSim UG as RD-Contractor of GRS.

The authors are responsible for the content of the report.

GRS - 750
ISBN 978-3-910548-41-1

Keywords

Groundwater, Density-driven Flow, Fracture Flow, Hydrogeology, Long-Term Safety Assessment, Modelling, Multigrid

Acknowledgement

This report summarizes the work in the joint project “Hydrogeological Modelling at a Regional Scale“ (HYMNE) of the project partners from the Goethe-Center for Scientific Computing (G-CSC) at the University of Frankfurt, the Techsim UG and the GRS. The project was funded by the German Federal Ministry for Economic Affairs and Energy (BMWi) under the contract no’s 02E11809A, and 02E11809B. We would like to thank all our colleagues who contributed to this final report and to the successful conclusion of the project.

Our very special thanks is due to Dmitry Logashenko (KAUST, Saudi Arabia) who helped us with his advice and support throughout the entire project. Finally, we would like to express our thanks to the collegues of the Repository Safety Research Division of GRS that were not directly concerned with the project, for their consultation.

Abstract

The code d³f++ was developed for the modelling of density-driven flow and nuclide transport in the far field of repositories for radioactive waste in deep geological formations. It can be used in porous media as well as in fractured rock or clay, for modelling salt and heat transport and for models with free groundwater surfaces.

The growing demands on groundwater flow and transport modelling require constant further development of the computer codes. Every potential repository site in Germany has been affected by permafrost conditions within the last 100,000 years. With the aim of enhancing d³f++ for the modelling of permafrost phenomena, the implemented equations were extended to include models for thawing and freezing processes. The new development was successfully tested by two benchmarks from the INTERFROST project.

Regional models with a free groundwater surface lead to a growing importance of an efficient model calibration. Therefore, a new tool for inverse modelling was implemented, tested and applied to a first large-scale 3D model. The level set method for modelling free groundwater surfaces was further stabilized, especially for large-scale models with density influence (1,000 km²). An ongoing process is the improvement of the robustness and efficiency of the multigrid solver. Parts of the code were restructured for this purpose.

As an alternative method for phreatic groundwater flow, a phase field model was introduced in d³f++, based on the Richards equation, that was generalized for density-dependent problems. Additionally, this model was adapted to make it also applicable to models with discrete, low-dimensional fracture networks.

Drainage through large networks of receiving waters plays a decisive role in the water balances of almost all regional models. It mainly depends on the water level, but often only the discharge of the main rivers is known. For this reason, a model based on the Saint Venant equation was implemented to enable the simulation of the water flow in the rivers.

An important part of the work was the application of d³f++ to two large-scale 3d models, the Äspö Site Descriptive Model (SDM), and the former candidate site Kraví Hora in the Czech Republic.

Zusammenfassung

Der Code d³f++ wurde für die Modellierung von Dichteströmung und Nuklidtransport Im Fernfeld von Endlagern für gefährliche Stoffe in tiefen geologischen Formationen entwickelt. Er kann sowohl in porösen Medien als auch im Kluftgestein oder Ton, für die Modellierung von Salz- und Wärmetransport sowie für Modelle mit freier Grundwasseroberfläche eingesetzt werden.

Die wachsenden Anforderungen an die Grundwasserströmungs- und Transportmodellierung erfordern eine ständige Weiterentwicklung der benutzten Rechenprogramme. Jeder potenzielle Endlagerstandort in Deutschland war innerhalb der letzten 100.000 Jahre von Permafrost-Bedingungen betroffen. Mit dem Ziel, d³f++ für die Modellierung von Permafrost-Phänomenen zu ertüchtigen, wurden die implementierten Gleichungen um Modelle für Auftau- und Gefriervorgänge erweitert. Die Neuentwicklung wurde anhand zweier Benchmarks aus dem INTERFROST-Programm erfolgreich getestet.

Regionalmodelle mit freier Grundwasseroberfläche machen eine effiziente Modellkalibrierung immer wichtiger. Deshalb wurde ein neues Tool zur inversen Modellierung implementiert, getestet und auf ein erstes großräumiges 3d-Modell angewandt. Das Level-Set-Verfahren zur Modellierung der freien Grundwasseroberfläche wurde insbesondere für großflächige Modelle mit Dichteeinfluss (1 000 km²) weiter stabilisiert. Ein ständiger Prozess ist die Verbesserung von Robustheit und Effizienz der Mehrgitterlöser. Ein Teil des Codes wurde dafür umstrukturiert.

Als alternative Methode für die phreatische Grundwasserströmung wurde ein auf der Richardsgleichung basierendes Phasenfeldmodell in d³f++ eingeführt. Dazu wurde die Gleichung auf dichteabhängige Probleme erweitert und verallgemeinert. Das Modell wurde so angepasst, dass es auch in Modellen mit diskreten, niederdimensionalen Kluftnetzwerken verwendet werden kann. Die Entwässerung durch umfangreiche Netze von Vorflutern spielt für die Wasserbilanzen fast aller Regionalmodelle eine entscheidende Rolle. Sie hängt hauptsächlich vom Wasserspiegel der Vorfluter ab, bekannt ist aber häufig nur der Abfluss. Deshalb wurde ein auf der Saint Venant-Gleichung basierendes Modell des Abflusses über die Vorfluter implementiert.

Ein bedeutender Teil der Arbeiten bestand in der Anwendung von d³f++ auf zwei großräumige 3d Anwendungsfälle, das Äspö Site Descriptive Model (SDM) und den potenziellen Endlagerstandort Kraví Hora in der Tschechischen Republik.

Content

1 Introduction

Long-term safety assessment for a radioactive waste repository requires a comprehensive system understanding and a proven and efficient set of instruments. Qualified high-performance tools are necessary to model groundwater flow and transport of radionuclides. These tools have to be able to describe all relevant processes concerning nuclide transport through the host rock and the overlying geological formations in feasible computing times.

Successful numerical groundwater flow and transport modelling is based on a profound hydrogeological knowledge. A growing amount of data and including more and more relevant physical processes lead to an increasing degree of approximation of the model representation to the real. The demands for accuracy and grid resolution are growing. Additionally, the problem of data uncertainties is ever more faced by stochastic modelling. All these requirements induce a growing complexity of the numerical models. On the other hand, proper definition of boundary conditions makes it necessary to choose the model boundaries correspondent to hydrogeological structures as watersheds. This leads to regional-scale models covering thousands of square kilometers. Climate changes are also to be regarded. Additionally, according to the German safety case requirements for heat-generating radioactive waste, an assessment time of one million years is regarded. All this implies a substantially increase of computational effort and makes it necessary to employ the most advanced hardware, and cutting-edge numerical solvers have to be used.

In 1994, GRS decided to develop its own code to describe groundwater flow and contaminant transport in the geosphere. Currently, the code d³f++ ("distributed density-driven flow") is the result of a series of BMBF- and BMWi-funded development and qualification projects since that time (see e.g. /FEI 99/, /FEI 04/, /SCH 12/, /SCH 13/, /SCH 16/, /SCH 20/), and it has been successfully applied in a large number of other projects, see e. g. /NOS 12/, /JOB 16/, /SCH 17/, /SCH 22/. All this work was funded by the Federal Ministry of Education and Research (BMBF) and by the Federal Ministry of Economics and Technology (BMWi), respectively.

The code d³f++ enables the simulation of density-driven groundwater flow in areas with complex hydrogeological structures, also on a regional scale, and the calculation of the transport of radionuclides and other pollutants in groundwater with all interactions that are relevant for repository safety research. It can be used both in sedimentary rock and

in fractured media. The programme is based on the UG4 code package (G-CSC, University of Frankfurt, /VOG 13/). The application of state-of-the-art numerical methods, especially parallel adaptive multigrid methods, and the resulting effective use of high-performance computers allow very fine grid resolutions and thus a high accuracy of the models with acceptable computing times. These methods are unique features of d³f++.

However, the growing extension and complexity of the models require steadily further speed-up and robustness of the solvers. At the other hand, recent scientific advances in the field of numerics have to be adopted, and code adaptions are crucial for profiting of new hardware developments. In order to achieve a broad applicability of d³f++ it is necessary to make further improvements. This also includes adaptations to new developments in computing technology, data interfaces to modern information systems or databases, improvements in preprocessing and the generation of computational grids, as well as adaptations to the requirements resulting from the processing of new fields of application.

More and more, model calculations are required on a regional scale and, as in the current SÚRAO models and the Äspö Site Descriptive Model (SDM), a correct modelling of the free groundwater surface is essential. In d³f++ a level-set method /FRO 12/ is used to describe situation and movement of phreatic surfaces. This method was originally developed for small, academic examples, and a lot of further work was necessary to stabilize it and to make it usable for models with an area of hundreds or thousands square kilometers. This work is described in chapter 4.3.

In the case of crystalline rock models, e. g. the Äspö-SDM model (see Chapter 5.1), it cannot be ruled out that the groundwater surface may sink into the fractured rock. In the GRUSS project /SCH 20/ it has proved almost impossible to combine the level-set method with lower dimensional discrete fracture models. Therefore, a second free surface model, based on Richard's equation combined with density-driven flow, was developed and implemented as described in chapter 4.4.

Another problem is, that in many of these models drainage by the receiving waters plays a crucial role for the groundwater balance. River draining was already implemented in d³f++ during the H-DuR project /SCH 16/. But the water levels of the rivers are generally not known or only known at a few gauging stations. In some cases, the runoff via the receiving waters can be quantified by measures or by using appropriate

surface runoff models. This information, on the other hand, could not be used for d³f++ to date. Therefore, a river flow model has been developed as described in chapter 2.3.

An intelligent, efficient model calibration plays an essential role, especially in the reliability of forecasts. Chapter 2.1 describes the implementation and the successful application of a new inverse modelling tool.

Modelling to simulate groundwater flow under freezing or thawing conditions is currently gaining increasing importance in the field of repository safety research, also on an international scale. All potential sites for a nuclear waste repository in Germany have been under permafrost conditions during the last 100.000 years. It has to be assumed that this will also happen in the future during the lifetime of any geological repository. Chapter 3 addresses the topic of modelling groundwater flow under permafrost conditions. The motivation and physical as well as mathematical models are discussed, the implementation is explained and model results of two benchmarks of the INTERFROST /GRE 18/ program are presented.

The growing extension and complexity of the models as well as the new features required the enhancement, further speed-up and improvement of the robustness of the numerical solvers. Chapter 4 outlines various advancements in this field.

A demonstration of the capability and efficiency of d³f++ in regional-scale modelling is important for a broad acceptance and application of the code. Chapter 5 outlines the application of d³f++ to two groundwater flow models in crystalline rock at a regional scale, the Äspö Site Descriptive Model and Kraví Hora, one of the former candidate sites in the Czech Republic.

Members of the joint project

Goethe Center for Scientific Computing (G-CSC), University of Frankfurt
Kettenhofweg 139, 60325 Frankfurt
Babett Lemke, Dr. Arne Nägel, Prof. Gabriel Wittum, Niklas Conen, Julian Hilbert, Tim Schön, Martin Stepniewski

Gesellschaft für Anlagen- und Reaktorsicherheit (GRS) gGmbH
Geological disposal division,
Th.-Heuss-Str. 4, 38122 Braunschweig
Anke Schneider, Anne Gehrke, Dr. Klaus-Peter Kröhn, Dr. Hong Zhao

and as RD-Contractor of GRS

TechSim UG,
Hebelstraße 5, 75249 Kieselbronn
Benjamin Wittum, Markus Knodel, Michael Lampe, Lukas Larisch, Felix Salfelder

2 Improvement of the applicability of d³f++

2.1 Governing equations for density driven flow in partially saturated media

In the last project period, the applicability of d³f++ has been broadened widely. One key feature is the extension to flow in unsaturated or partially saturated media. This concept is elaborated in greater detail in Section 4.4.

At this point, the governing equations are stated /BEA 10/, /CON 22a/, CON 22b/. Expressing the conservation of the fluid and the salt mass respectively in terms of fluid pressure p and salt mass fraction ω as primary variables yields

$$\begin{aligned} &\partial_t(\Phi S\rho\omega) + \nabla\cdot(\rho\omega\boldsymbol{q} - S\rho\boldsymbol{D}\nabla\omega) = 0, \\ &\partial_t(\Phi S\rho) + \nabla\cdot(\rho\boldsymbol{q}) = 0, \end{aligned} \qquad (2.1)$$

with Darcy's law

$$\boldsymbol{q} = -\frac{\boldsymbol{K}k}{\mu}(\nabla p - \rho\boldsymbol{g}), \qquad (2.2)$$

and Scheidegger's tensor

$$\boldsymbol{D} = \Phi S\boldsymbol{D}_{mol} + \boldsymbol{D}_{mec}(\boldsymbol{q}). \qquad (2.3)$$

Here, the density $\rho = \rho(\omega)$ and the viscosity $\mu = \mu(\omega)$ are given by non-linear material laws. The porosity Φ, the permeability $\boldsymbol{K}$, the gravity $\mathbf{g}$ and the sources q_V are constant or depend on space only.

Furthermore,

$$S = S(p) \quad and \quad k = k(S(p)) \qquad (2.4)$$

are the saturation and the relative permeability of the porous medium, respectively. These functions are usually given by constitutive relations. An in-depth discussion is provided in Sections 2.4 and 4.4.

For $S = k = 1$ in (2.4) the classic system for density driven flow is recovered.

2.2 Inverse modelling and calibration

For subsurface problems on the regional scale, not all model parameters are known a-priori. The following subtasks provides methods and tools to identify these parameters and to calibrate models towards given data. The concrete case outlined below assumes that measurements of the groundwater table have been given. In a second step, varying model parameters such as porosities, permeabilities, recharge and/or well pumping rates are then calibrated to provide a fit to the data. The abstract theoretical framework and the underlying software is described in Section 2.2.1. Experiments and a field scale application are provided in Section 2.2.2. This section summarizes some key findings from /SCH 20a/.

2.2.1 Optimization algorithms

In the following, let $\vec{\boldsymbol{d}}$ denote a vector containing data from measurements, e.g., the level of the groundwater table measured at certain wells and certain point in time. It is assumed that a corresponding data set $\vec{\boldsymbol{m}}(\boldsymbol{\theta})$ can be generated in a simulation that is performed using a vector of parameters $\boldsymbol{\theta}$. The goal is to find parameters θ that provide a best fit to the data.

2.2.1.1 Minimization Problem

Let $\vec{r} := \vec{m}(\theta) - \vec{d}$ denote the residual, which indicates the mismatch between model response m and data d. The unconstrained minimization problem is to find an optimal value

$$\theta^* := \operatorname{argmin} L(\theta)$$

that minimizes the mismatch in form of a least-squares problem:

$$L(\theta) := \frac{1}{2}\left|\left|\vec{m}(\theta) - \vec{d}\right|\right|^2 = \frac{1}{2}\left|\left|\vec{\mathrm{r}}(\theta)\right|\right|^2 \qquad (2.5)$$

Here $\vec{m}(\theta)$ is the result from a parameter dependent simulation and $\vec{d}$ is a data vector that should be matched, e.g., obtained from field measurement. Note, that the minimum of (2.5) is in general not unique. Hence all algorithms discussed below aim at finding a local minimum.

To that end, we are now reviewing different iterative methods. Based on the update formula

$$\theta = \theta + p$$

with a suitable search direction p different algorithms can be derived. Using the Jacobian

$$J := \frac{\partial \mathrm{r}(\theta)}{\partial \theta} = \frac{\partial \mathrm{m}(\theta)}{\partial \theta},$$

the following linearizations hold:

$$m(\theta + p) = m(\theta) + \frac{\partial m(\theta)}{\partial \theta} p, \qquad r(\theta + \mathrm{p}) = r(\theta) + \frac{\partial \mathrm{r}(\theta)}{\partial \theta} p$$

Given parameters θ, a local quadratic model L is given by

$$\mathrm{L}(\theta + p) \approx L(\theta) + \frac{\partial \mathrm{L}(\theta)}{\partial \theta} \mathrm{p} + \frac{1}{2} \mathrm{p}^{\mathrm{T}} \mathrm{H}\, \mathrm{p}$$

where

$$\frac{\partial \mathrm{L}(\theta)}{\partial \theta} = J^T r, \qquad \mathrm{H} = J^T J + \mathrm{S}, \qquad \mathrm{S}_{ij} = \sum_k r_k \frac{\partial^2 \mathrm{r}_k(\theta)}{\partial \theta_i \, \partial \theta_j}$$

Based on this representation, various methods can be derived. The algorithms differ in choice of the direction p:

- The **gradient method** relies on the negative gradient:

  $$p = -J^T r.$$

- The **Gauß-Newton method** is based on the assumption $\mathrm{L}(\theta + p) = 0$, and computes a descent direction p using the corresponding the normal equation:

  $$(J^{\mathrm{T}} J)\, \mathrm{p} = -J^T r. \qquad (2.6)$$

- The **Levenberg-Marquardt algorithm** is a compromise of the aforementioned methods. Here

  $$(J^{\mathrm{T}} J + \lambda I)\, \mathrm{p} = -J^T r.$$

For $\lambda \gg 1$ this leads to a (scaled) gradient method, whereas for $\lambda \ll 1$ obviously a Gauß-Newton scheme is recovered. In a practical implementation, λ can be computed automatically.

- For **limited memory BFGS method,** p is derived from the formula:

  $\mathrm{B\ p} = -J^T r.$

  The special trick here is to select B as a symmetric positive definite matrix, that is constructed as a sequence of rank-1-updates approximating H. The method can be adjusted, such that box constraints of the form $\underline{\theta_i} \leq \theta_i \leq \overline{\theta_i},\ i = 1 \ldots p$ can be included (LM-BFGS-B)

The search direction p obtained by any of the methods usually yields a constraint, but is is not optimal in general. Hence, the direction should be rescaled with a real number β, such that

$L(\theta + \beta\ \mathrm{p}) < \mathrm{L}(\theta)$

The optimal value $\beta*$ minimizing the left hand side is not known. However, it may be computed heuristically. One simple approach to generate a finite set of values, e.g.,

$\beta(\mathrm{k}) = 2^{-\mathrm{k}}, \mathrm{k} = 0, \ldots \mathrm{N}.$

Among those, the one yielding the smallest value $L(\theta + \beta_k\ \mathrm{g})$ is selected. This is a simple line search, which can be conducted in parallel. However, more sophisticated versions have been implemented as well /SCH 20a/.

Algorithm GaussNewtonMethod()
Input: Initial guess $\vec{\theta}^{(1)}$
1. Compute d
2. For i=1, …, i_{max}:
   a. Compute Jacobian $J(\theta_i)$
   b. Compute $L_i := L(\theta_i)$
   c. If (L_i < eps L_0) return θ_i
   d. Compute QR decomposition J=QR
   e. Solve (2.2) in two steps:
      w = Q^T d
      R p = -w
   f. Determine optimal step length β
   g. Set $\theta_{i+1} = \theta_i + \beta p$

2.2.1.2 Design and Components

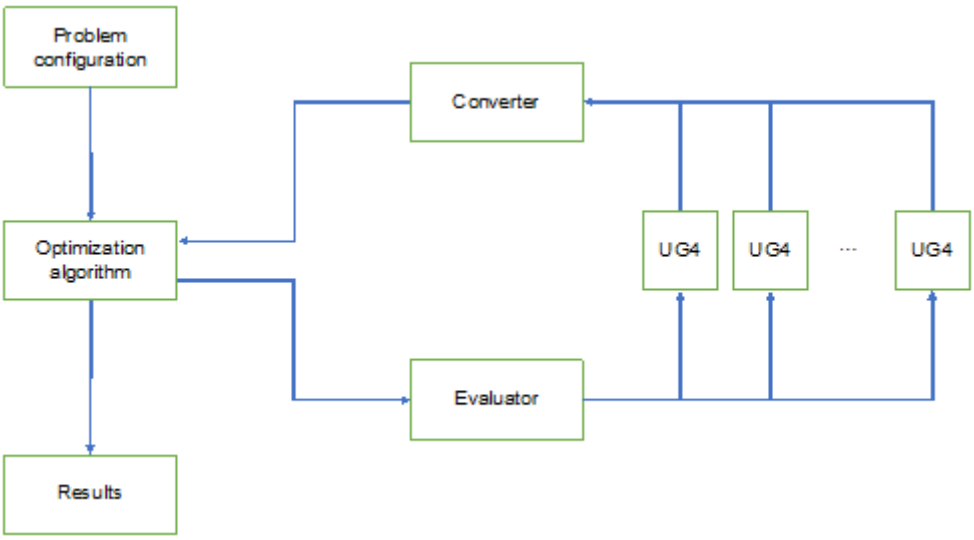

Fig. 2.1 Sketch of the optimization loop (redrawn from /SCH 20a/)

The parameter estimator has been implemented in a modular fashion, see Fig. 2.1. The implementation is based on Python. As mentioned earlier, for the optimization, different methods can be selected, e.g. Gauß-Newton method, Levenberg-Marquardt and limited memory BFGS.

Evaluator

Evaluator objects are responsible for triggering parameter dependent simulations $S: \theta \rightarrow S(\theta)$. The primary instance is the class `ClusterEvaluator`, which has been designed for parallel execution on clusters with a batch scheduling system, such as Slurm /SLURM/. For execution on local workstations and laptops, a class `LocalEvaluator` provides similar functionality.

Communication between Python and UG4 /VOG 13/ is established via a file interface. Input parameters are provided in a file `parameters.txt`, which is follows LUA syntax and is included as in inline form in the LUA source code. Double evaluations are avoided by caching all evaluation request. Moreover, a flag for invalid evaluations is supported and allows handling both invalid input parameters as well as invalid results and failed simulations.

Simulations in UG4

For each simulation run $S = S(\theta)$ the height of the free surface is determined by a C++-class `FSFileMeasurer`. At a given time t, e.g., given by the last successful time step, the class evaluates the position z of the level-set function for a given set of coordinates in the x,y-plane. The function returns tuples (t, x, y, z), which are concatenated in a file in binary or text representation.

Conversion and interpolation

Given a simulation run S, measurements of the free surface height are given at discrete times $\{t_i\}$ resulting from the adaptive time-stepping strategy. The field data to compare to is given either at discrete points $\{T_j\}$ in time or in equilibrium in the limit $t \to \infty$.

The first case is treated by a class `FreeSurfaceTimeDependentEvaluation`. In this case, let $\vec{m}_j = \left(\varphi_S(T_j, x_k)\right)$ and $\vec{y}_j = \left(\varphi(T_j, x_k)\right)$ denote vectors representing the free-surface height in simulation and field data measurements at time T_j respectively. For the simulation, this data is obtained by linear interpolation from the point set $\{t_i\}$, if necessary. This yields block vectors

$$\vec{m} := (\vec{m}_j), \vec{d} := (\vec{d}_j)$$

which can be used to formulate the minimization problem.

More important is the limit case $t \to \infty$, which is covered by a class `FreeSurfaceEquilibriumEvaluation`. Since the temporal evolution towards the steady state is unkown, it must be detected in the simulation. To that end, changes are detected based on the quantity

$$c(i) := \left\| \frac{\vec{m}_i - \vec{m}_{i-1}}{\tau_i} \right\| \approx \left\| \frac{\partial \vec{m}}{\partial t}(t_i) \right\| \qquad (2.7)$$

which approximates the Euclidian norm of the derivative of the measurement w.r.t time. If the system approaches a steady-state $\lim_{i \to \infty} c(i) = 0$ holds. Hence, relative changes can be evaluated using the measure

$$\rho(n) \coloneqq \frac{c(n)}{\max\limits_{i=1,\dots,n} c(i)} < 1$$

Given a user-defined tolerance $\rho_{TOL} \ll 1$, the simulation should be aborted, if $\rho(n) < \rho_{TOL}$ or $c(n) < \rho_{TOL} \max\limits_{i=1,\dots,n} c(i)$. In this case,

$$\vec{m} := \vec{m}_\infty, \vec{d} := \vec{d}_\infty$$

Where $\vec{m}_\infty = \left(\varphi_S\left(t_{final}, x_k\right)\right)$ is the simulated data form the final time step and $\vec{d}_\infty$is the field data reference.

2.2.1.3 Evaluating the Jacobian

The optimization algorithms must evaluate the Jacobian of the residual w.r.t. the parameters, i.e.,

$$J(\theta) = \begin{pmatrix} \frac{\partial r_1}{\partial \theta_1}(\theta) & \cdots & \frac{\partial r_1}{\partial \theta_b}(\theta) \\ \vdots & \ddots & \vdots \\ \frac{\partial r_{n_v}}{\partial \theta_1}(\theta) & \cdots & \frac{\partial r_{n_v}}{\partial \theta_b}(\theta) \end{pmatrix} \in \mathbb{R}^{n_v \times b}$$

As the exact derivatives are not available, the terms are using finite differences: For a given parameter vector θ, and a small parameter ε define the variation in the i-th component by

$$\theta^\varepsilon(i,\varepsilon) \coloneqq \begin{cases} (\theta_1, \theta_2, \dots, (1+\varepsilon)\theta_i, \dots, \theta_b)^T, \text{ if } \theta_i \neq 0, \\ (\theta_1, \theta_2, \dots, \varepsilon, \dots, \theta_b)^T, \text{if } \theta_i = 0\,. \end{cases}$$

Denoting the forward difference approximation of the derivative w.r.t the i-th component by

$$\delta_i^+ \vec{r}(\theta) \coloneqq \begin{cases} \frac{m\left(\theta^\varepsilon(i,\varepsilon)\right) - m(\theta)}{\varepsilon\theta_i}, \text{ if } \theta_i \neq 0\,, \\ \frac{m\left(\theta^\varepsilon(i,\varepsilon)\right) - m(\theta)}{\varepsilon}, \text{ if } \theta_i = 0\,. \end{cases}$$

yields the following approximation of the Jacobian $J^{+}(\theta) = (\delta_1^{+}\vec{r}(\theta), \ldots, \delta_{\mathrm{b}}^{+}\vec{r}(\theta)) \in \mathbb{R}^{n_v \times b}$, which has an accuracy of O(ε).

Similarly, the central difference approximation

$$\delta_{\mathrm{i}}^{\mathrm{c}}\vec{r}(\theta) := \begin{cases} \dfrac{m\left(\theta^{\varepsilon}(i,\varepsilon)\right) - m\left(\theta^{\varepsilon}(i,-\varepsilon)\right)}{\varepsilon\theta_i}, \text{ if } \theta_i \neq 0\,, \\ \dfrac{m\left(\theta^{\varepsilon}(i,\varepsilon)\right) - m\left(\theta^{\varepsilon}(i,-\varepsilon)\right)}{\varepsilon}, \text{ if } \theta_i = 0\,. \end{cases}$$

yields $J^{c}(\theta) = (\delta_1^{\mathrm{c}}\vec{r}(\theta), \ldots, \delta_{\mathrm{b}}^{\mathrm{c}}\vec{r}(\theta)) \in \mathbb{R}^{n_v \times b}$, which is O($\varepsilon^2$) accurate.

Assembling the linear system requires (b+1) evaluations of r for the forward differences and (2b+1) evaluations of r for the central differences respectively. However, the evaluations are independent and can be performed in parallel. The wall clock time using the `ClusterEvaluator` is thus bound by largest time required for a single evaluation.

2.2.1.4 Sensitivity

The i-th column of the Jacobian J specifies, how the model m depends on the parameter θ_i. Following /JOH 02/, we introduce

$$\sigma(\mathrm{m},\mathrm{i}) = \frac{\theta_{\mathrm{i}}}{\|\mathrm{m}(\theta)\|}\delta_{\mathrm{i}}^{+}\mathrm{r}(\theta) \qquad (2.8)$$

2.2.2 Numerical Experiments

2.2.2.1 Experiment 1: Pumping Experiment into a Box

For the first test, water is pumped into a container, which is concealed on the lateral sides and on the bottom, but open on the top. The geometry is given by a square of 1m x 1m. This is modelled by the domain $\Omega = [0,1] \times [0,1]$ with no-flux and Dirichlet (with p=0) boundary conditions respectively. The goal is to calibrate the position of the free surface. This setup will also be used in subsequent experiments, unless it is stated otherwise.

In Experiment 1a, and all density effects are neglected. Porosity and permeability are assumed to be homogeneous. The free surface is initially located at a height of 0.1 m.

A pump injecting fresh water with a strength of q=0.0001 m³/s is placed in proximity of the lower left corner at the position x = $(0.1, 0.05)^T$.

Regression results (high sampling density): The objective for calibration is obtained after a simulation run over 10 s. Reference values are $\psi = 0.1$ and $\kappa = 1 \times 10^{-11}$ m². In equidistant 50 time-steps (with step size dt=0.2 s), the free surface height has been recorded at 5 equidistant spatial locations. This is a high sampling density and results in a data set with a total on nv=250 recorded points. The results are shown in Tab. 2.1.

Tab. 2.1 Experiment 1: Gauß-Newton convergence (250 sampling points)

Iteration	$\boldsymbol{\kappa}$ [m²]	$\boldsymbol{\psi}$	β	**Objective**
0	$1.0 \cdot 10^{-10}$	0.2	0.3333	$1.553 \cdot 10^{-5}$
1	$2.178 \cdot 10^{-11}$	0.1317	0.6667	$5.591 \cdot 10^{-4}$
2	$1.023 \cdot 10^{-11}$	0.1026	0.8889	$6.227 \cdot 10^{-6}$
3	$1.003 \cdot 10^{-11}$	0.1002	-	$4.366 \cdot 10^{-8}$

Regression results (small sampling density): For the problem at hand, using a high number of sampling points is not necessary. To illustrate this, the experiment has been repeated using only nv=3 points obtained at the final time from three points from an equidistant distribution in space. Results are shown in Tab. 2.2.

Tab. 2.2 Experiment 1: Gauß-Newton convergence (3 sampling points)

Iteration	$\boldsymbol{\kappa}$ [m²]	$\boldsymbol{\psi}$	β	**Objective**
0	$1.0 \cdot 10^{-10}$	0.2	0.3333	$1.553 \cdot 10^{-5}$
1	$1.429 \cdot 10^{-11}$	0.1272	0.7778	$4.481 \cdot 10^{-6}$
2	$1.006 \cdot 10^{-11}$	0.1001	0.8889	$1.961 \cdot 10^{-11}$
3	$1.001 \cdot 10^{-11}$	0.1	1.0	$1.809 \cdot 10^{-13}$
4	$1.0 \cdot 10^{-11}$	0.1	–	$8.989 \cdot 10^{-16}$

Sensitivity: As described in Section 2.2.1.4, the columns of the Jacobian represent sensitivity information. This is visualized in Fig. 2.2. For the purpose of visualization, an increased sampling density with 50 equidistant points has been used in the spatial direction:

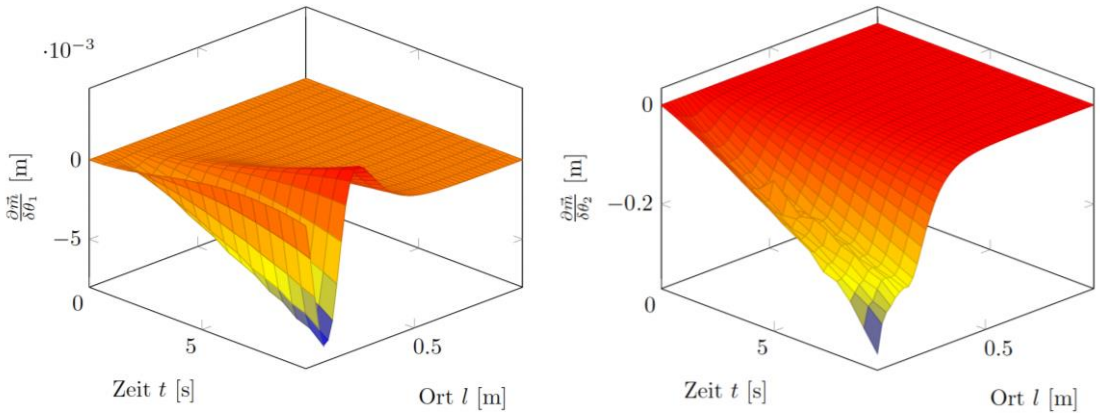

Fig. 2.2 Experiment 1a: Sensitivity information for permeability (left) and porosity (right), source: /SCH 20a/

The results can be interpreted as follows:

- An increase in permeability yields an increased flow away from the source. Hence, the free surface moves downward in the direct proximity of the source. However, as mass is conserved, the surface moves upward in the larger neighborhood.
- An increase in porosity yields a decrease in the whole domain. This is due to the fact, that the storage capacity of the medium increases, which effectively slows down the movement of the surface.
- Both effects increase monotonously as time advances.

2.2.2.2 Experiment 2: Elbe 2D

The last experiment uses a 2D cross section obtained from a real-world geometry treated in the NAWAK project /WOL 18/. The setup is illustrated in Figure 2.3: The geometry consists of five layers differing in permeability and porosity. The horizontal extension is ~ 9km, the vertical thickness ~100 m. While small hills impose a watershed and limit the domain on the left, the terrain falls towards the sea on the right side. The boundary conditions are Dirichlet condition for hydrostatic pressure on the right side and a Neumann zero on the left side and on the bottom. On the top surface, a recharge with rate $r=\gamma r_0$ has been prescribed based on experimental historical data r_0 from the year 2011. The scaling factor γ provides some flexibility. In the middle of the domain at the position x=4.75 km, a well extracts water in a line segment in a depth between z=-14 and -34 m. The extraction rate is $q=10^{-6}$ m^3/s.

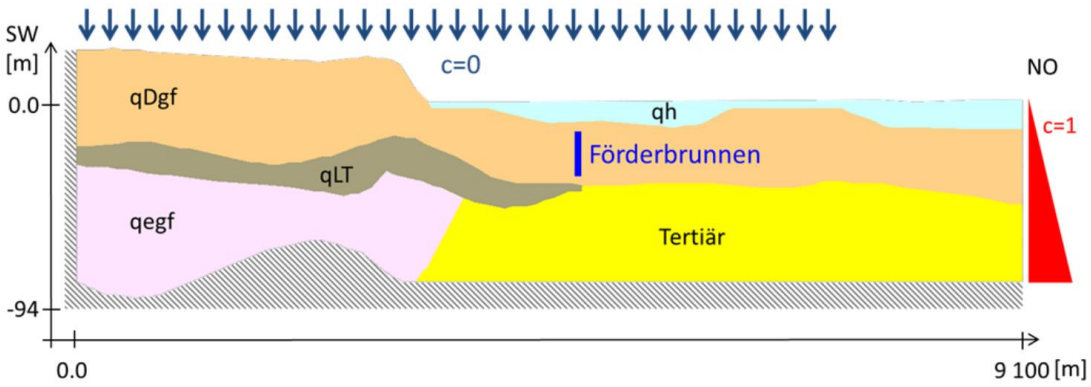

Name	qDgf	Tertiär	qh	qLT	qegf
Layer	Sand	Sediment	Fine sand	Clay	Coarse sand
Permeability [m²]	**$5 \cdot 10^{-12}$**	$5 \cdot 10^{-15}$	10^{-13}	**$5 \cdot 10^{-16}$**	$5 \cdot 10^{-13}$
Porosity [1]	0.2	0.1	0.1	0.05	0.15

Fig. 2.3 Experiment 4: Cross section and model parameters in the subdomains /WOL 18/, /SCH 20a/

Tab. 2.3 Experiment 2: Gauß-Newton convergence (50 equidistant points)

Iteration	**Permeability κ_qDgf [m²]**	**Permeability κ_qLT [m²]**	**Extraction q [m³/s]**	**Recharge scal. γ [1]**	**Line search β**	**Objective**
0	$2.7 \cdot 10^{-12}$	0.2	$5.43 \cdot 10^{-7}$	1.0	0.333	3.192
1	$2.341 \cdot 10^{-12}$	$2.935 \cdot 10^{-17}$	$4.622 \cdot 10^{-7}$	0.8467	0.5556	2.9686
2	$3.948 \cdot 10^{-12}$	$2.977 \cdot 10^{-17}$	$6.894 \cdot 10^{-7}$	1.346	0.6667	$2.17 \cdot 10^{-2}$
3	$3.923 \cdot 10^{-12}$	$1.425 \cdot 10^{-16}$	$7.292 \cdot 10^{-7}$	1.4424	0.7778	$1.83 \cdot 10^{-2}$
4	$3.961 \cdot 10^{-12}$	$4.849 \cdot 10^{-16}$	$8.048 \cdot 10^{-7}$	1.4553	$1.0 \cdot 10^{-2}$	$6.33 \cdot 10^{-3}$
5	$3.961 \cdot 10^{-12}$	$4.823 \cdot 10^{-16}$	$8.049 \cdot 10^{-7}$	1.4554	$1.111 \cdot 10^{-4}$	$6.33 \cdot 10^{-3}$
6	$3.961 \cdot 10^{-12}$	$4.823 \cdot 10^{-16}$	$8.049 \cdot 10^{-7}$	1.4554	---	$6.33 \cdot 10^{-3}$

In the experiment, the model has been calibrated for a steady state using the detection mechanism from Eq. 2.7. Free parameters are: permeabilities for qDgf and qLT, the extraction rate $q=10^{-6}$ m³/s and the recharge scaling $\gamma=2$. As illustrated in Tab 2.3, these parameters are identified correctly:

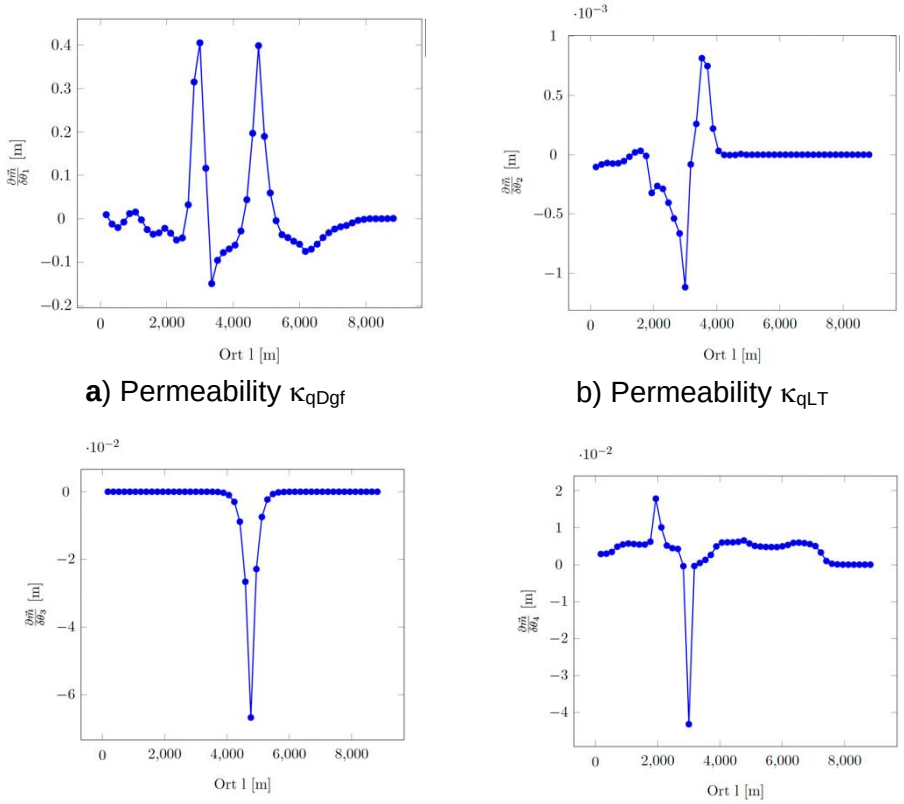

a) Permeability κ_{qDgf} b) Permeability κ_{qLT}

c) Extraction rate q d) Recharge

Fig. 2.4 Benchmark “Elbe 2D”: Sensitivity of the free surface w.r.t model parameters: (a) permeabilities of qDgf and (b) qLT, (c) pump rate, (d) recharge /SCH 20a/.

In equilibrium, the sensitivity of the free surface w.r.t the model parameters, can be investigated (cf. Fig 2.4):

- The permeability of the pDgf layer has big impact on the position of the free surface in particular in the area of the step an is most pronounced between x=2900 m and x=4700 m (cf. Figure 2.3). An increased permeability raises the free surface, which is plausible, as water flows from the left to the right in this region.
- The impact of the permeability of the qLT layer is less pronounced: An increased permeability renders a flow from the left to the right in the direction of the well. However, as the layer is located underneath the well, the free surface sinks down.
- An extraction by pumping lowers the groundwater table in the vicinity of the well.

- Recharge increases the groundwater level. The reason for the sharp drop at x=3000 m remains unclear.

2.2.2.3 Application: Seawater intrusion model Sandelermöns

As a first real application, the inverse modelling tool was used for the calibration of the ground water model Sandelermöns, see /SCH 22/, where the permeability parameters are estimated from a given set of datapoints for the measurement of the groundwater level.

Sandelermöns is a coastal groundwater study area in the northwest of Germany and covers an area of about 1,000 km² as shown in Fig. 2.5. Almost half of the model region next to the North sea coast is low-lying and formed part of the North Sea several hundred years ago, resulting in saline groundwaters in the aquifers. The south-western part of the model region consists of moraines and the remarkable recharge rates lead to a rich amount of fresh groundwater. In the model area exist three waterworks, Sandelermöns, Feldhausen and Kleinhorsten.

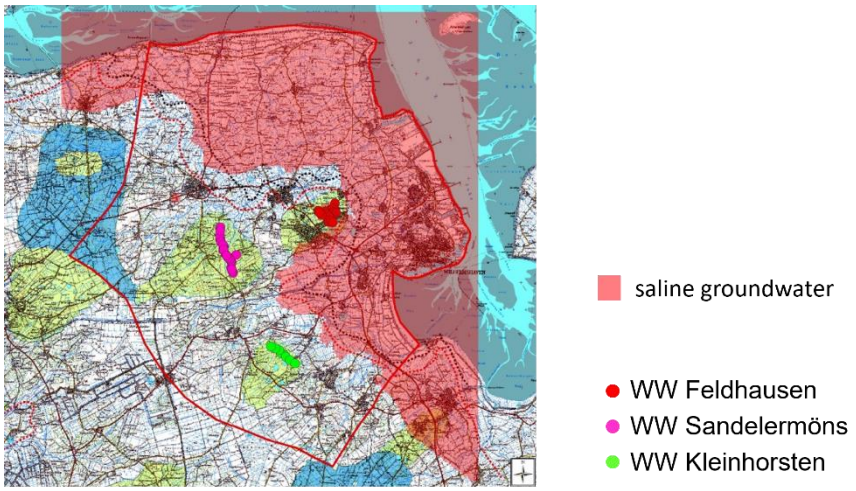

Fig. 2.5 Sandelermöns model area including the wells of the three waterworks and area of saline groundwaters

The complex 3d hydrogeological model was set up by the Oldenburg-Ostfriesian Water Company (OOWV). Six formations are distinguished. The top of the model consists of thin layers of Lauenburg clay, dune sands and silty materials. In the middle exists a continuous layer of melt-water sands and a small field of Tergast clay, followed by a thick layer of fluvial sands at the bottom. Fig. 2.6 shows the hydrogeological model created and the start values for the permeabilities and porosities.

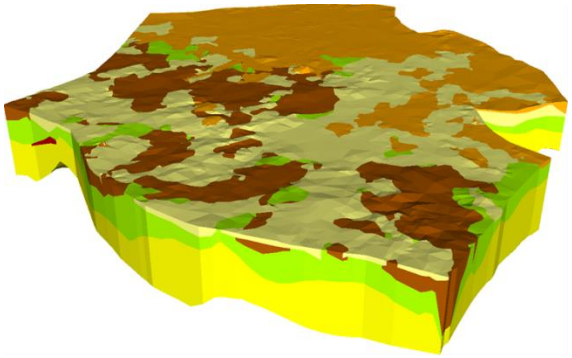

	unit	permeability [m²]	porosity [-]
	silt	$1 \cdot 10^{-12}$	0.1
	sands	$1 \cdot 10^{-10}$	0.2
	Lauenburg clay	$1 \cdot 10^{-13}$	0.05
	melt-water sands	$4 \cdot 10^{-11}$	0.2
	Tergast clay	$1 \cdot 10^{-13}$	0.05
	fluvial sands	$2.8 \cdot 10^{-11}$	0.2

Fig. 2.6 Hydrogeological model of the Sandelermöns region, 30x scaled in vertical direction

The south-western boundary of the model is located on a watershed and therefore assumed to be impermeable. The salt concentration is set to zero. The north-western and south-eastern boundaries are chosen perpendicular to the water table isohypses and therefore also regarded as impermeable for groundwater flow. The coastal boundary is equipped with a hydrostatic pressure for seawater and a salt concentration of 35 kg/m^3. For the bottom of the model geological knowledge suggests almost impermeable clayey formations. On the upper boundary, the boundary with free groundwater table, a Dirichlet boundary condition $p = 0$ is set for the pressure. The concentration is also set to zero.

The north-eastern region of the model domain is characterized by a dense net of small draining ditches and rivers conducting water to the coastal pumping stations in the dikes to keep the groundwater level below land surface. This drainage plays a crucial role in the hydraulic regime and had to be incorporated in the model. Regrettably there exists only little information about the water levels of the receiving streams in the Sandelermöns region as well as the pumping rates of the coastal stations. Missing information was replaced by reasonable assumptions to meet the natural hydraulic regime by a careful calibration process.

Furthermore, the 51 pumping wells of the waterworks and 36 private wells were included into the model. The initial condition for the free groundwater table is estimated by averaging and interpolating the data of 284 measuring points and wells for 2017. The initial condition for the salt concentration is based on geoelectromagnetic data provided by the Leibniz Institute for Applied Geology. Time dependent groundwater recharge data were computed by the Braunschweig Technical University using the hydrological model PANTA RHEI /KRE 15/, distinguishing 147 polygons. The complete model is

visualized in Fig. 2.7. For calibration of the groundwater table, the time dependent data were averaged for the year 2017. The Levelset Method /FRO 12/ was used for the modeling of the free groundwater surface.

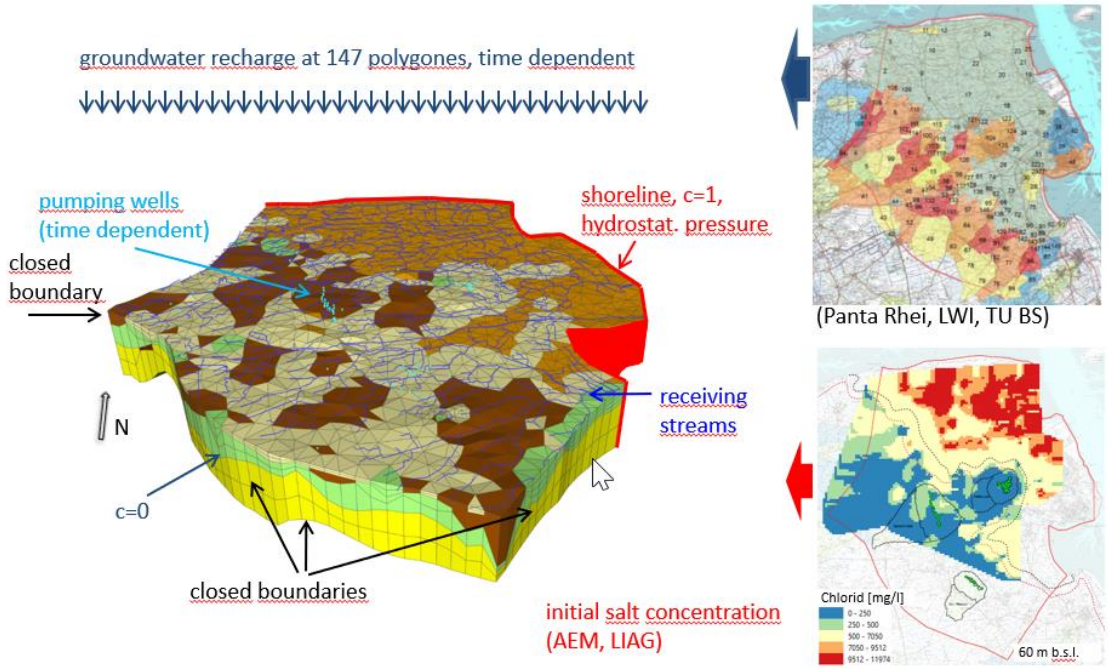

Fig. 2.7 Sandelermöns model with prism grid, boundary conditions, receiving streams (blue) and pumping wells (light blue);
right: groundwater recharge on 147 polygons and initial salt concentration

The model calibration started with the initial and boundary conditions as described above. The coarse grid consisted of 21,304 prism elements. Simulations were performed on grid level 2 consisting of 1,363,456 elements. In a first step, it took about 20 years of model time until the fluid volume in the model had reached a steady state. Factors influencing this volume are the initial groundwater level, sea level, recharge rates, river drainage and pumping rates.

The model reacts mostly sensitive against variations in sea level, represented by the hydrostatic pressure boundary condition at the north-eastern boundary. River drainage relatively to the recharge rates is much more influencing the results than well pumping. In addition, the permeability of the layers has a big impact on the groundwater levels. Theses sensitivities form a problem because of the poor knowledge about groundwater levels in the coastal zone as well as river drainage.

To test the newly developed calibration tool, the permeability of the layers was chosen to calibrate the model. A residual function was established based on the difference of the simulated and the measured data at 269 wells. After some tests, it was found that the permeabilities of layer 2, layer 3 and layer 4 are mostly influencing the groundwater table, whereas the permeabilities of other layers have minor influence. Therefore, the permeabilities of these layers built up the parameter set to calibrate the model.

For each iteration step, parameter sets consisting of start values, minimum and maximum values were defined in d^{3}f++, and a simulation started for a model time of 20 years. Based on the resulting residuals, the Jacobian was evaluated, and a search direction for the parameter variation was computed. The parameters were varied within a factor set along this direction to find the best factor for the minimum of the residual function. This iteration step was repeated until the residual function could not be decreased anymore. Tab. 2.4 compiles the start, minimum and maximum values and the resulting calibrated permeability values after 10 iteration steps.

Tab. 2.4 Permeability as result of model calibration

layer number		unit	permeability [m^2]			
			start	minimum	maximum	calibration
2		sands	$1 \cdot 10^{-10}$	$1 \cdot 10^{-13}$	$1 \cdot 10^{-7}$	$5.1 \cdot 10^{-11}$
3		Lauernburg clay	$1 \cdot 10^{-13}$	$1 \cdot 10^{-15}$	$1 \cdot 10^{-10}$	$7.2 \cdot 10^{-13}$
4		melt-water sands	$4 \cdot 10^{-11}$	$4 \cdot 10^{-15}$	$4 \cdot 10^{-7}$	$1.7 \cdot 10^{-11}$

Fig. 2.8 shows the simulated groundwater surface after a model time of 20 years as a result of the calibration process. In the scatter plot on the right simulated groundwater levels are compared with measured data. The Nash-Sutcliffe coefficient reaches 0.78. Four points (read, blue, black and purple) from different regions are chosen to compare between the simulated groundwater levels and the measured data during the model time of 20 years.

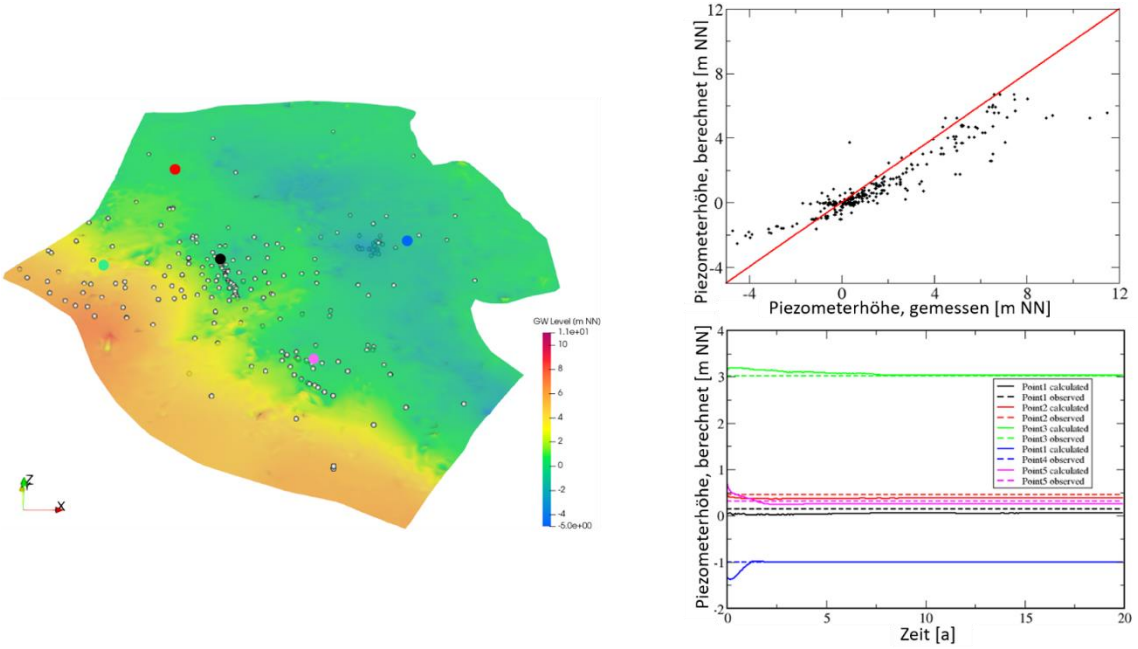

Fig. 2.8 Simulated groundwater level with gauge wells;
right: comparison of measured and simulated data during calibration after a model time of 20 years

In this calibration test of Sandelermöns, the permeabilities of three layers were chosen as calibration parameters. The residual function was computed from the differences of the simulated and the measured groundwater table at the gauge wells. Using the new inverse modeling tool, the calibration of the model could be significantly improved. In consideration of the lack of data and the still relatively coarse grid the calibration results are rather good and plausible. Nevertheless, the residual function can also be built up from the differences of the simulated and measured salt concentrations, in combination with the groundwater table differences. In addition, the river drainage can also be used as a parameter for further calibration.

2.3 Coupling with rivers

For the simulation of models on regional scale a coupling with surface flow is an important requirement. The existing framework supported rivers in static form only, i.e., the height of the water level was provided explicitly as user provided data. In the novel framework, this was replaced by a dynamic approach. Here, the river networks have been described by the Saint-Venant equations. The novel module supports coupling to subsurface flow using phreatic groundwater surfaces (cf. Section 4.4.) To that end, additional identification and mapping algorithms using kd-trees have been implemented. This section summarizes some key findings from /HIL 22/.

2.3.1 Saint-Venant Equations

The Saint-Venant equations describe 1-D incompressible flow in open channels and are a restriction of the 2-D shallow water equations.

$$\frac{\partial A}{\partial t} + \frac{\partial vA}{\partial x} = 0 \qquad (2.9)$$

$$\frac{\partial v}{\partial t} + \frac{\partial}{\partial x}\left(\frac{1}{2}v^2\right) + g\frac{\partial(h+z_s)}{\partial x} = \frac{\partial}{\partial x}\left(\nu_t \frac{\partial v}{\partial x}\right) - \frac{\lambda}{8}\frac{U}{A}|v|v \qquad (2.10)$$

where velocity v and wetted cross-section A are the unknown variables of the system. Other parameters are properties of the channel and geometry: (h+z_s) is the free surface elevation, represented by the sum of water level h and height of the channel bed z_s. U describes the wetted perimeter. Together with wall roughness parameter λ, the wall sheer stress can be estimated. Further are ν_t and g the diffusive and gravitational constants, respectively.

The Saint-Venant equations are implemented as a Finite Volume discretization on a grid consisting of line segments. These may form channel networks via junctions as an extension of the 1d model.

2.3.2 Validation Experiments for Saint-Venant

In the following experiments, the Saint-Venant equations are compared to the normal water level h_n as a reference. h_n is the water level of a sufficiently long channel with constant flow and properties. First, consider the cutout of a straight river with constant

elevation change (Fig. 2.9a). Inflow is set on the left boundary as a Dirichlet boundary condition. As expected, the normal water level is established over the course of the channel. Problems with h_n as a predictor arise with variable geometry and properties of the channel. This can be seen by the discrepancy between h_n and the simulated water level in Fig. 2.9b. Here, a depression in the channel bed should fill with water until it can flow freely across the boundary. A solution with the Saint-Venant equations predicts this behaviour as expected.

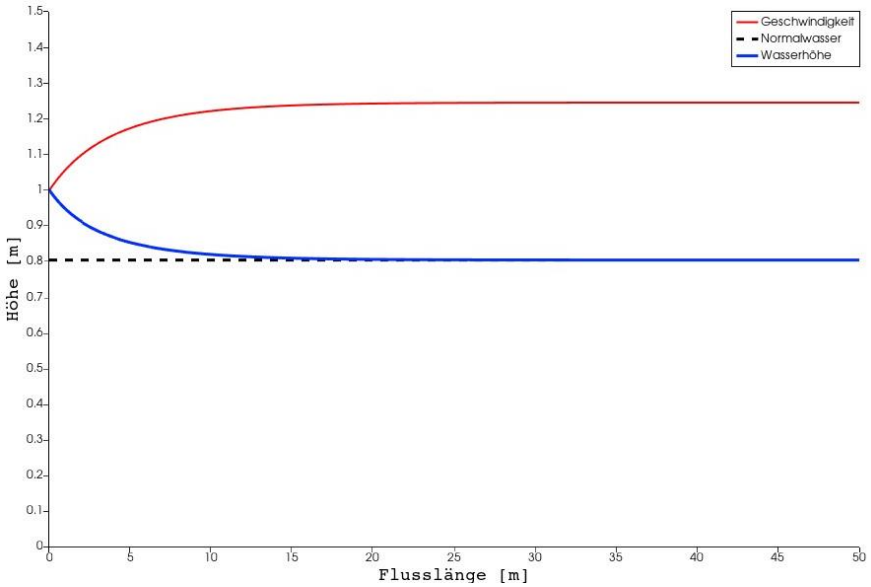

a) Straight channel with elevation gradient 0.02 and inflow Q = 6 m³/s. Velocity v [m/s] shown in red.

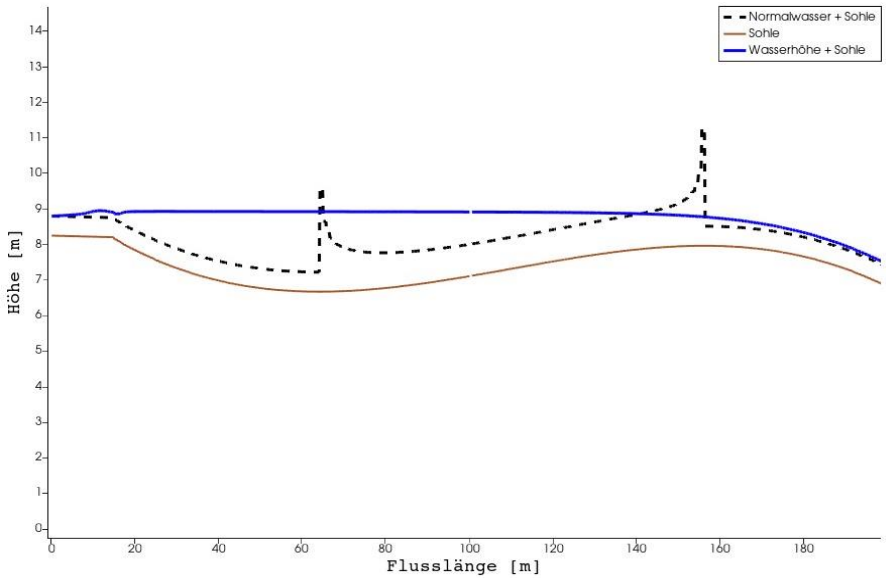

b) Channel with changing channelbed (brown).

Fig. 2.9 Solution of the Saint-Venant equations for different channels. Illustrated are water level h (blue) and normal water level h_n (dashed).

The union of two channel segments should have consistent flow above and below the junction. To verify this, flow is calculated on a y-shaped grid where two minor channels lead into the main channel. As can be seen in Fig. 2.10, the outflow in the main channel is the sum of inflow across the minor channels. Mass is conserved, but this approach may lead to local inconsistencies of v and A around the joint.

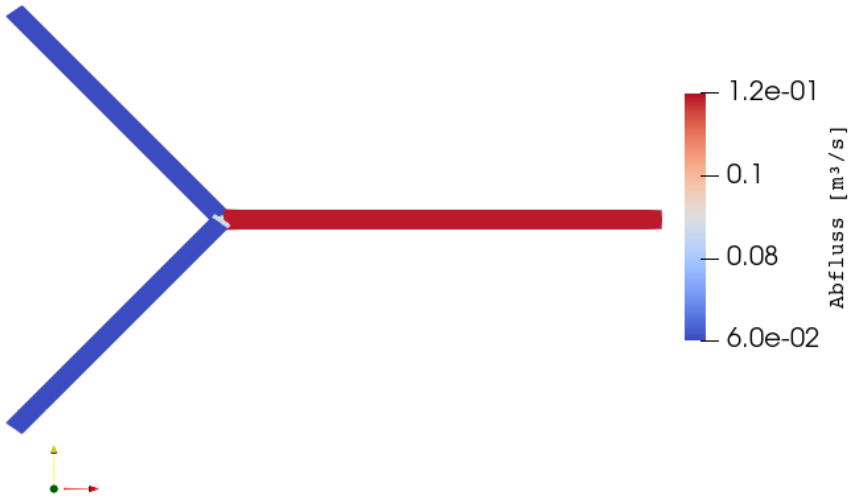

Fig. 2.10 Union of two channels minor channels on the left side of the region. Plotted is the flow in [m^3/s].

2.3.3 Coupling of Surface and Subsurface

The Saint-Venant equations is a good candidate for modelling surface runoff over regions in form of river networks. To achieve this, a (weak) coupling approach between surface and subsurface is being been developed. Subsurface flow is described by the Richards-equation. Flow across both domains is calculated proportional to the pressure-dependent Darcy velocity over an interface and handled by a boundary condition switching algorithm as a post process of the time-stepping scheme for the subsurface problem. The interface consists of elements in the subsurface domain that are in direct contact with segments of the surface domain where an exchange of mass may happen.

An example for the infiltration process of river water over time is shown in Fig. 2.11. Consider a rectangular porous media below a straight river section. The Saint-Venant equations are solved on the surface domain and the calculated water column exerts pressure on the upper boundary of the subsurface domain. This can be modeled via boundary conditions. Pictured in Fig. 2.12 are slices through the subsurface domain that show the time evolution of water pressure in the soil, given as the height h_p of an

equivalent standing water column. The groundwater table is colored green and represents the region where $h_p = 0$.

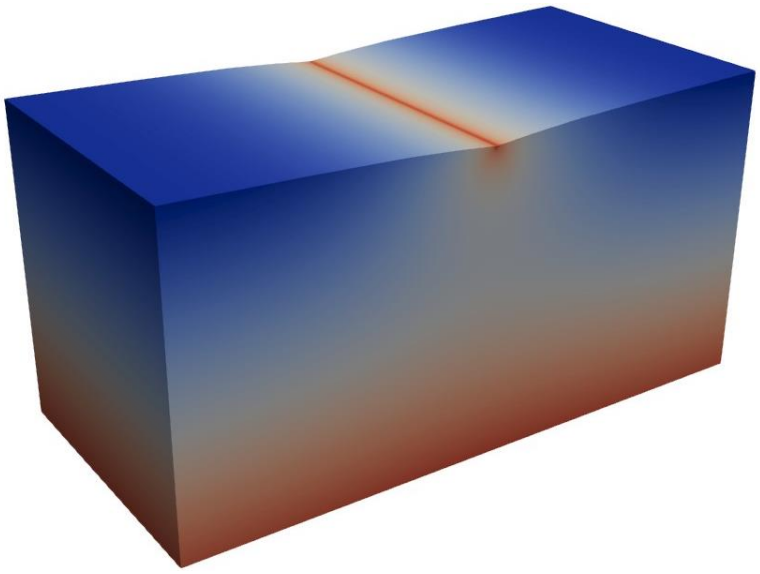

Fig. 2.11 Model of a rectangular porous media below a straight river section.

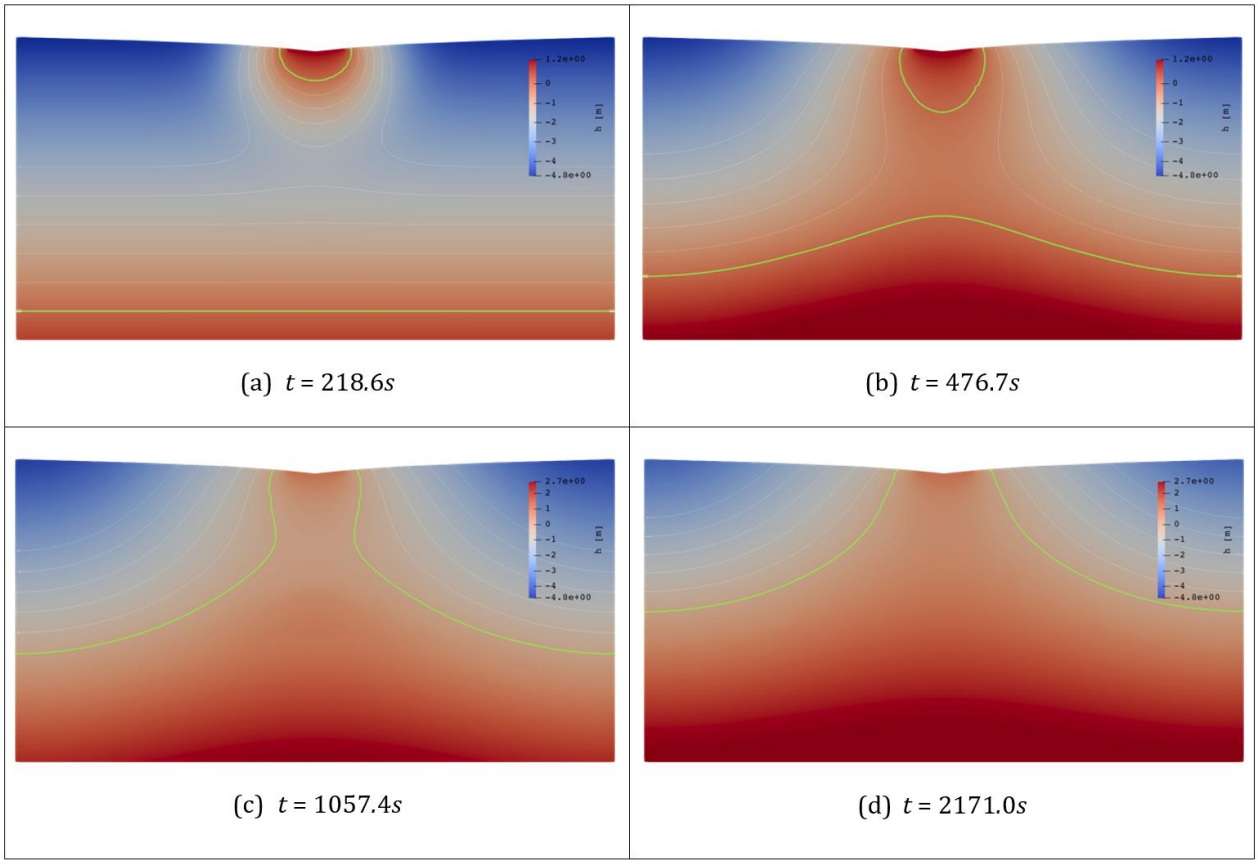

Fig. 2.12 River section over soil consisting of sand. Isolines show regions of constant pressure, where zero-value (green) marks the free surface

2.3.4 Complex river networks

For more complex field scale scenarios, a novel geometric coupling algorithm has been implemented. For a river network that is given in terms of line segments, the algorithm computes intersections with the related triangles. This is illustrated in Fig. 2.13 as an example for the Čihadlo region.

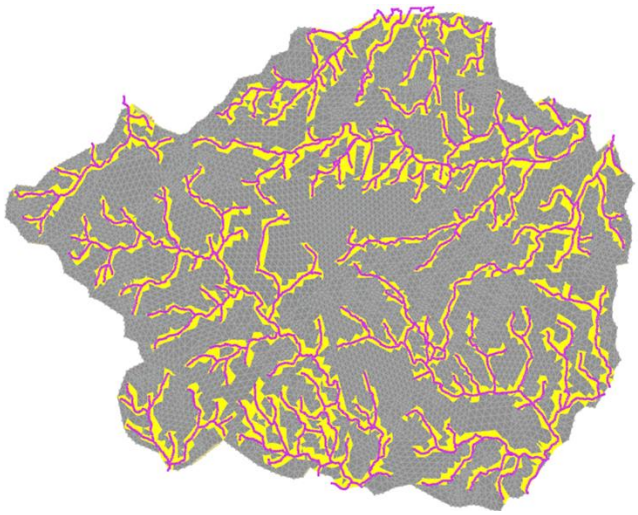

Fig. 2.13 Intersection of the river network (magenta) with the surface of the porous medium (yellow/grey). Contact between surface and subsurface contact is determined in the region of yellow triangles /HIL 22/

2.4 Groundwater flow with phreatic surface in fractured media

Fractures are subregions of the entire simulation domain Ω with a negligible thickness (aperture) but high permeability. Presence of the fractures changes the flow significantly. Due to the technical and numerical difficulties in the full-dimensional resolution of the fractures, they are frequently considered as low-dimensional manifolds where the flow and transport equations are formulated in a special form. One of these approaches has been implemented in d^3f and then transferred to d^3f++, cf. /GRI 10/, /GRI 12/, /STI 12/. The method is based on the resolution of the fracture network by the grid and filling the fractures with the so-called degenerated elements, cf. also /REI 12/ and /REI 20/. Equations of the potential, saline and thermohaline flow are discretized in the full-dimensional and degenerated elements by a FV scheme. This approach allowed additional degrees of freedom in the fracture that proved to be important for the non-linear problems with non-rotation-free velocity field.

However, this approach does not combine with the phreatic surface represented by a moving boundary as used in our previous simulations. Such a coupling would result in an unphysical deformation of the phreatic surface and further numerical artefacts. Instead, one can introduce the saturation S of the porous medium by the fluid phase and formulate the problem analogously to the Richards equation.

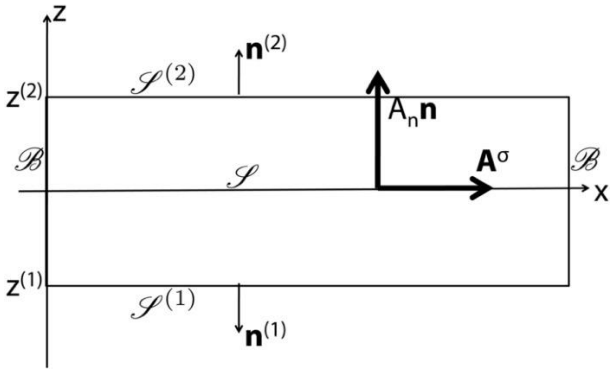

Fig. 2.14 Scheme of the fracture, cf. /GRI 12/

For the saturation S and relative permeability k, one can use in particular the van Genuchten – Mualem law. This law describes the situation well in a more or less homogeneous domain where porosity and permeability have no jumps. Any interfaces, for example the sides of the fracture, would influence the flow due to the capillary forces. If these phenomena become essential, one should consider for ex. the Brooks-Corey law for (2.4).

In the part of the domain where $S = 1$, (2.1) and (2.2) reduce to the usual system of the density-driven flow equations. In this region, $p \geq 0$ and $k = 1$. This changes in the partially saturated part of the domain, where $p < 0$ and therefore $0 \leq S < 1$, as well as $0 < k < 1$. In this part, this model still allows flow. This fact is important for the fractures that can bring a flow to some partially saturated subdomains.

The system (2.1) consists of a special type of convection-diffusion equations and can be generalized for the fractures using the method described in /REI 12/. This method has already been adapted for other flow equations, cf. for ex. /GRI 13/. We demonstrate this technique for the second equation in (2.1), i.e. the Richards equation

$$\partial_t(\Phi S\rho) + \nabla \cdot (\rho \boldsymbol{q}) = 0, \qquad \boldsymbol{q} = -\frac{\boldsymbol{K}k}{\mu}(\nabla p - \rho \boldsymbol{g}). \tag{2.11}$$

Its application to the first equation in (2.1) is completely analogous. Furthermore, for simplicity, we assume that we have only one fracture $\mathcal{F} \subset \Omega$. Generalization to the case of arbitrary fracture networks is obvious. The subdomain enclosing the fracture is denoted by $\mathcal{M}$, so that $\Omega = \mathcal{M} \cup \bar{\mathcal{F}}$. The boundary of this fracture consists of two parallel sides $\mathcal{S}_1$ and $\mathcal{S}_2$, as well as the lateral boundary $\mathcal{B}$: $\partial\mathcal{F} = \mathcal{S}_1 \cup \mathcal{S}_2 \cup \mathcal{B}$, s. Fig. 2.14. As the aperture ϵ of $\mathcal{F}$ (the distance between $\mathcal{S}_1$ and $\mathcal{S}_2$) is negligible, we replace $\mathcal{F}$ in the model by its middle surface $\mathcal{S}$. Under this consideration, $\mathcal{S}_1$ and $\mathcal{S}_2$ lie one upon the other but are not identified. They denote the different interfaces between the fracture and the enclosing medium. We denote by $\widehat{\mathcal{B}} \coloneqq \mathcal{S} \cap \mathcal{B}$ the edge of the low-dimensional representation $\mathcal{S}$ of the fracture $\mathcal{F}$. Furthermore, the enclosing medium $\mathcal{M}$ is also replaced by larger subdomain $\widehat{\mathcal{M}} \coloneqq \Omega \setminus \mathcal{S}$. For every of the components of the solution (the pressure and the mass fraction of the salt), we define two different functions: In $\widehat{\mathcal{M}}$, these are the pressure $p_m: \widehat{\mathcal{M}} \to \mathbb{R}$ and the mass fraction $\omega_m: \widehat{\mathcal{M}} \to \mathbb{R}$ in the enclosing medium. Note that these (continuous) functions have generally two different limits at points $x \in \mathcal{S}$. We denote the limits of p_m at the sides $\mathcal{S}_1$ and $\mathcal{S}_2$ by $p_m^{(1)}$ and $p_m^{(2)}$, respectively. (The same for ω_m.) Furthermore, on $\mathcal{S}$, we define the functions $p_f: \mathcal{S} \to \mathbb{R}$ and $\omega_f: \mathcal{S} \to \mathbb{R}$. We refer to /REI 12/ for a more detailed discussion.

Now, (2.11) should be considered separately on $\widehat{\mathcal{M}}$ and $\mathcal{S}$. Furthermore, conditions on $\mathcal{S}_{1,2}$ must be imposed to relate p_m with p_f, as well as ω_m with ω_f.

On $\widehat{\mathcal{M}}$, we get the equation similar to (2.11):

$$\partial_t(\Phi_m S_m \rho_m) + \nabla \cdot (\rho_m \boldsymbol{q_m}) = 0, \qquad \boldsymbol{q_m} = -\frac{\boldsymbol{K_m} k_m}{\mu_m}(\nabla p_m - \rho_m \boldsymbol{g}), \quad x \in \widehat{\mathcal{M}} \qquad (2.12)$$

where Φ_m and $\boldsymbol{K_m}$ characterize the porous medium in $\widehat{\mathcal{M}}$, $\rho_m = \rho(\omega_m)$, $\mu_m = \mu(\omega_m)$, $S_m = S(p_m)$ and $k_m = k(S(p_m))$.

On the low-dimensional fracture surface $\mathcal{S}$, the following analogue of (2.11) is considered

$$\partial_t\big(\epsilon \Phi_f S_f \rho_f\big) + \nabla_{\mathcal{S}} \cdot \big(\epsilon \rho_f \boldsymbol{q_f}\big) + Q_{fn}^{(1)} + Q_{fn}^{(2)} = 0, \quad x \in \mathcal{S}. \qquad (2.13)$$

Here and below, $\nabla_{\mathcal{S}}$ denote the differential operators on the surface $\mathcal{S}$, Φ_f and $\boldsymbol{K_f}$ characterize the porous medium in $\mathcal{F}$, $\rho_f = \rho(\omega_f)$, $\mu_m = \mu(\omega_f)$, $S_f = S(p_f)$ and $k_f = k(S(p_f))$. The transport velocity $\boldsymbol{q_f}$ along the fracture is defined as

$$\boldsymbol{q}_f = -\frac{\boldsymbol{K_f} k_f}{\mu_f}\left(\nabla_{\mathcal{S}} p_f - \rho_f \boldsymbol{g_f}\right), \quad x \in \mathcal{S}, \tag{2.14}$$

where $\boldsymbol{g_f}$ is the projection of the gravity $\boldsymbol{g}$ to tangential space of $\mathcal{S}$. The terms $Q_{fn}^{(k)}$ describe the mass flux between the fracture and the enclosing medium:

$$Q_{fn}^{(k)} = \rho\left(\omega_m^{(k)}\right) q_{fn}^{(k)} \tag{2.15}$$

with

$$q_{fn}^{(k)} := -\frac{K_{fn} k_{fn}}{\mu\left(\omega_m^{(k)}\right)}\left(\frac{p_m^{(k)} - p_f}{\epsilon/2} - \left(\rho\left(\omega_m^{(k)}\right) - \rho_f\right) g_{fn}^{(k)}\right), \tag{2.16}$$

where $g_{fn}^{(k)}$ is the projection of the gravity $\boldsymbol{g}$ to the outer normal $\boldsymbol{n}^{(k)}$ to $\mathcal{S}_k$; K_{fn} and $k_{fn} = k_{fn}\left(S\left(p_m^{(k)}\right), S\left(p_f\right)\right)$ are the permeability and the relative permeability at the interface $\mathcal{S}_k$ between the fracture and the porous medium. Note that (2.16) contains the correction of the gravity term to avoid the parasitic flow arising due to the replacement of $\mathcal{M}$ by $\widehat{\mathcal{M}}$. Dependence of k_{fn} on both the pressures allows to include the trapping phenomena due to the entry pressure for some particular laws for (2.4).

On the interfaces $\mathcal{S}_1$ and $\mathcal{S}_2$ the continuity of the mass fluxes should be imposed:

$$Q_{fn}^{(k)} = \rho\left(\omega_m^{(k)}\right) \boldsymbol{q_m^{(k)}} \cdot \boldsymbol{n}^{(k)} \tag{2.17}$$

where $\boldsymbol{q_m^{(k)}}$ is the limit of (2.16) at the point $x \in \mathcal{S}_k$ of the interface. Equations (2.12), (2.13)-(2.16) and (2.17), together with the initial and the boundary conditions for $p_{m,f}$ and $\omega_{m,f}$ form a closed system.

For the numerical solution of the presented equations, the fractures must be filled with 2 layers of the degenerated elements and the degrees of freedom should be assigned as described in /REI 12/. This technique is implemented in ug4 as well as in ProMesh, and has proved its efficiency. The same method is used for the flow equations (2.12), (2.13)-(2.16) and for the transport equations for the salt. For the discretization of the equations in $\widehat{\mathcal{M}}$, the full-dimensional vertex-centered finite volume method based on the Donald diagrams is applied. For the numerical treatment of the equations in the de-

generated elements, the low-dimensional version of this FV scheme is used, cf. /REI 12/.

2.5 Technical improvements

2.5.1 Restart with section of higher resolution

Here, the idea was to embed a detailed model of a small part of the domain into a larger-scale model with less resolution. Boundary conditions for the detailed model simulation are taken from the large-scale model. Both models are computed with d³f++. A coupling between both models was implemented, which uses the standard adaptive refinement environment in UG4 /VOG 13/. I. e. the subdomain, where the detailed information or simulation at a finer grid resolution is needed, has to be defined and refined locally. The results of the large, coarsely resolved domain with less hydrogeological information suffices to define boundary conditions for the detailed simulation.

3 Groundwater flow in permafrost conditions

3.1 General remarks

This section addresses the topic of modelling groundwater flow under permafrost conditions in a somewhat holistic manner. It starts in subsection 3.2 with the motivation for the present work and a problem definition, followed by subsection 3.3 with a short description of the physical processes involved. By comparison, much room is given to the discussion of the mathematical model in subsection 3.4 as a clear and comprehensive treatment seems to be missing in the literature. In subsections 3.4.7, the thread is taken up to describe the required implementations in code d³f++ and subsection 3.5 shows the results of model calculations based on benchmarks from the INTERFROST-project /GRE 18/ using the new features.

Note that subsections 3.2 to 3.4 represent a condensed version of the more comprehensive GRS-report 707 (/KRÖ 22/).

3.2 Motivation

Deep geological disposal of nuclear waste implies (1) storage at a depth of several hundred metres below surface and (2) a safety assessment that covers a long period of time. In Germany a time span of 1,000,000 years has to be considered /STA 17/. One of the main concerns for such a repository is the detrimental effect of groundwater on the technical and geotechnical barriers, a second one the migration of radionuclides with the groundwater into the biosphere in case of a possible failure of the waste canisters. For long-term safety considerations, a well-founded knowledge of the local and regional groundwater system is therefore required in any case.

Potential sites for repositories in Germany require a suitable host rock that is a formation with low hydraulic conductivity. In the framework of the ongoing site selection process, 54 % of the area of Germany are presently under investigation /BGE 20/ (see Fig. 3.1, left). During the latest cold period, the Weichselian glacial (Würm glacial stage for the Alpine region), all of Germany with a small exception to the mid-west has experienced either continuous permafrost and or even coverage by an ice shield (see Fig. 3.1, right; e.g. /VAN 93/ and /REN 03/). At one time or another, all potential sites for a nuclear waste repository have thus been under permafrost conditions during the last

100.000 years. It has to be assumed that this will also happen in the future during the lifetime of any geological repository in Germany.

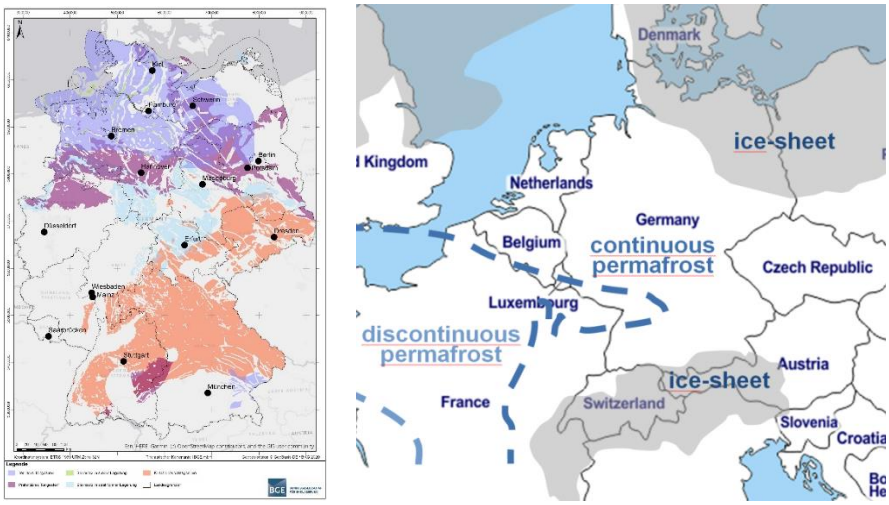

Fig. 3.1 Potential sites for a deep geological repository (left) /BGR 12/ and permafrost conditions during the latest ice age (right), after /VAN 93/ and /REN 03/

Ground freezing to a large lateral as well as vertical extent is the consequence of lasting permafrost conditions. Changes between moderate and cold periods may therefore lead to radical changes in the groundwater flow system with a strong impact on a potential radionuclide migration as illustrated in Fig. 3.2.

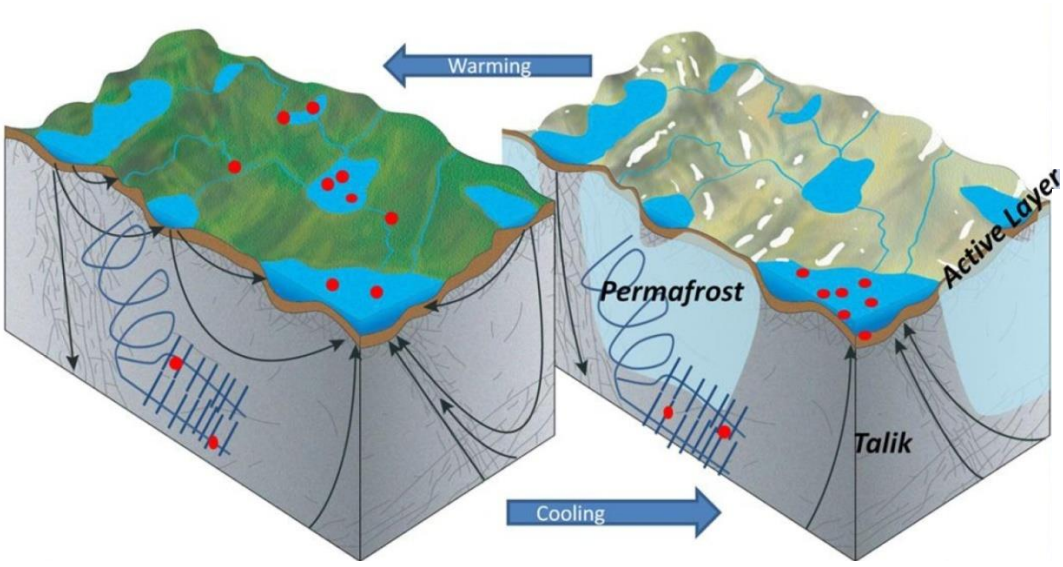

Fig. 3.2 Impact of permafrost on radionuclide migration; from /JOH 16/

The sketch illuminates the situation for a geological repository in granite below a slopy area that includes lakes and rivers. In this situation, groundwater flow is driven by different heights of surface water levels and precipitation, both resulting in hydraulic pressure gradients.

During warmer climates, groundwater flow is characterized by a comparatively shallow flow system where the water can be imagined seeking paths of the least flow resistance. Groundwater taking up radionuclides from a leaking waste canister may therefore distribute them over quite a large area. In general, the flow can be considered to be more or less well known.

Under permafrost conditions, by contrast, many of the shallow flow paths are blocked by the evolving ice. Flow from above ground to the next available aquifer in the subsurface and vice versa is restricted to locations with open taliki - bodies of unfrozen ground occurring in a permafrost area - forcing the water deeper downwards and concentrating a potential outflow of radionuclides to the few open taliki.

Taliki represent a key feature in a groundwater flow system under permafrost conditions. Knowledge of size and location as well as stability of taliki is thus vital for predicting possible radionuclide migration. On the whole, conditions for talik development are investigated in relation to climate warming, though (e.g. /PAR 18/).

Consequences for the potential migration paths of radionuclides in case of a canister breach are therefore presently hard to predict. Highly adverse appears to be the possibility that contaminated waters may be able to reach the surface via open taliki while remaining highly concentrated with pollutants.

Taliki often form below larger surface waters such as lakes and rivers, e.g. /DEL 98/, /KEL 98/, /SKB 06/, raising the suspicion that they are hydrothermal taliki by nature. They are thus not accessible to direct observation but can be detected by laborious field work (e.g. /JOH 16/). Understanding of the mechanisms that create taliki and keep them open over longer times might be gained by numerical modelling, though.

Following this idea implies that the simplest physically conceivable configuration should be investigated in order to get the most meaningful results. The present work is therefore restricted to periglacial permafrost conditions and intends to provide the basis for a

modelling exercise that aims at understanding of the mechanisms about talik forming and talik persistence.

3.3 Relevant physics

Neglecting mechanical effects from expansion during freezing as well as from water flow, ground freezing is a thermal problem that is basically controlled by the mean ground surface temperature, heat production from earth's core and the thermal properties of the geological units (see Fig. 3.3, left).

Much more challenging is the simulation of the development of taliki which is a delicate process and requires a thermo-hydraulic (TH-)coupling. Furthermore, development of an open talik may be influenced by the actual groundwater flow system to an unknown extent in which case talik forming is site specific.

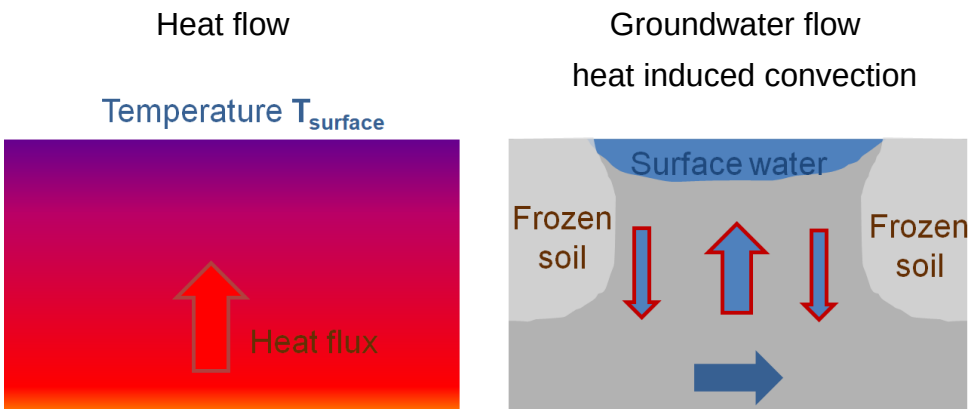

Fig. 3.3 Relevant processes for groundwater flow under permafrost conditions

Groundwater flow in general involves a porous matrix of solids and a theoretically unlimited number of fluids in the pore space. Here, the considerations are restricted to a solid matrix being fully saturated with water for temperatures above 0 °C. For temperatures falling below the freezing point, the water exists partly as a liquid and partly as solid ice where the fraction of water decreases with temperature until basically all water becomes frozen. The relation between temperature and water fraction is called "soil freezing characteristic curve (SFCC)".

Where water and ice coexist, the volume occupied by the two phases can be characterized by the saturation with unfrozen water S_w and the ice saturation S_i, respectively[1], which are defined as the volumetric fraction of the respective phase of the total pore volume.

$$S_w = \frac{V_w}{V_p} \qquad and \qquad S_i = \frac{V_i}{V_p} \tag{3.1}$$

S_w - saturation of the pore space with unfrozen water [-]
S_i - saturation of the pore space with ice [-]
V_w - volume of the unfrozen water [m³]
V_i - volume of the ice [m³]
V_p - pore volume [m³]

Consequently, the two saturations defined in (3.1) add up to 1:

$$S_w + S_i = 1 \tag{3.2}$$

Groundwater flow occurs in the pore space of a porous matrix[2]. The physics described above therefore suggest that the groundwater system under freezing conditions can be regarded as a two-phase, single-component system. The component water exists either in a liquid state as water or in a solid state as ice and phase changes are possible according to the prevailing temperature. Neglecting furthermore the movement of ice, flow of water can be considered to be a special form of unsaturated flow where ice is displacing water like water displaces air in a conventional unsaturated flow problem.

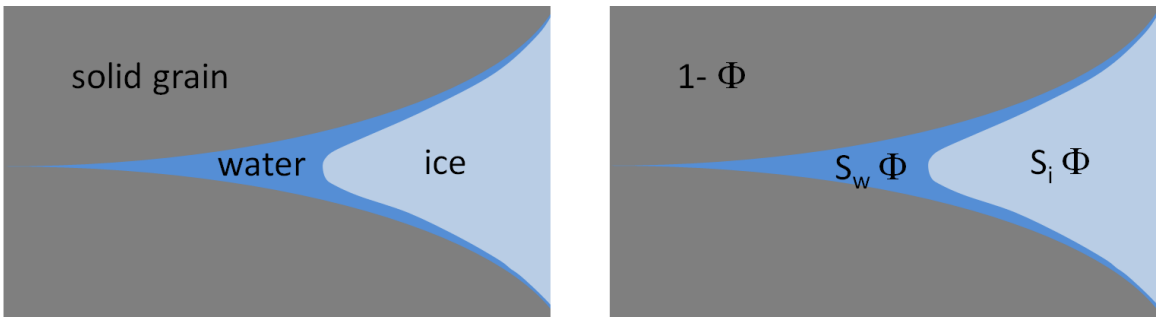

Fig. 3.4 Principle sketch illustrating porosity Φ and saturations S

[1] Note that the indices w for water, i for ice and m for the solid matrix will be used further on.

[2] In a fractured porous medium this applies of course also to the open fractures.

Freezing and melting in the underground implies transient thermal processes that interact with the groundwater flow in a rather complex way. On the one hand, the properties of water that are controlling flow are dependent on the transient temperature field and on the other hand, heat gets transported with the water by advection and possibly by convection. Phase changes draw or release energy from/to the immediate vicinity thereby influencing the temperature field even further. The concomitant volumetric changes cause the water to be either squeezed out during freezing of or to be sucked into the pore space during melting. A model of groundwater flow under freezing conditions thus requires a concept where thermo-hydraulic processes are fully coupled. If porosity changes are considered by frost heave or thawing settlement, a coupling to further mechanical processes may be in order. This, however, is beyond the scope of this report.

3.4 Mathematical model

3.4.1 General remarks

There is already quite an amount of literature covering the topic of groundwater flow under permafrost conditions. A selection of these references has been compiled in /KRÖ 22/ to find out about an appropriate mathematical description. Instead of shedding light upon this task, the compilation left the reader rather confused due to the diversity of approaches, though. In order to gain a maximum of clarity, a mathematical model has therefore been developed from scratch.

General balance equations for flow and heat transport are derived in the following expressively refraining from prematurely introduced assumptions and restrictions. They form a metaphorical “game board” for simulations that needs to be supplemented by a figurative “book of rules” defining (a) the choice of processes that are taken into account, (b) the principles behind the constitutive relations, and (c) the related state variables. The book of rules also requires some “amendments”. These amendments declare the intended range of validity for the numerical model with respect to the primary variables, in the present case: pressure and temperature. These ranges control eventually the degree of complexity that is required for the mathematical formulation of the constitutive equations (CEs) and the equations of state (EOS). The book of rules including the amendments thus defines a particular game i.e. a particular modelling framework.

Since the ranges of validity limit the variation of an EOS within the given bounds, simplifications of the EOS can be introduced. It is assumed here that an EOS varying by less than 1 % might reasonably well be approximated by a constant value. Where such an approximation appears to be feasible, the affected balance equations can be simplified as well. This has been done with a view to the INTERFROST benchmarks mentioned above. The resulting balance equations are then presented in subsection 3.4.7.[3]

3.4.2 Balance equations

A general balance equation for a not yet specified extensive[4] mass-related quantity $Z(t)$ that moves in a velocity field $\boldsymbol{v_a}$, can be derived on general principles (for details see e.g. /KRÖ 22/, /GÄR 87/). It is formulated in terms of the related density $z(\boldsymbol{x}, t)$ of quantity $Z(t)$

$$Z(t) = \int_{V(t)} z(\boldsymbol{x}, t)\, dV \qquad (3.3)$$

$Z(t)$ - extensive variable in $V(t)$ with the appropriate dimension <dim> [<dim>]
$V(t)$ - 3D-domain moving with the flow [m³]
$z(\boldsymbol{x}, t)$ - density of $Z(t)$ [<dim>/m³]

as an integral over a fixed finite control volume G:

$$\int_G \left[\frac{\partial z}{\partial t} + \nabla \cdot (\boldsymbol{v_a} \mathrm{z} + \boldsymbol{J})\right] dV = \int_V \bar{r}\, dV \qquad (3.4)$$

$\boldsymbol{v_a}$ - (interstitial[5]) flow velocity [m/s]
t - time [s]
$\boldsymbol{J}$ - non-advective flow of Z across the surface S [<dim>/(m² s)]
$\bar{r}$ - production of Z in G [<dim>/ (m³ s)]
G - spatially fixed control volume [m³]

Considering the conservation of the mass of water by defining

---

[3] Differently motivated simplifications have also been applied from which other forms of the mathematical model arose. These can be found in /KRÖ 22/.

[4] basically meaning additive like mass or energy

[5] in case of porous media

$$
\begin{aligned}
Z(t) &= m_w(t) \\
z(\boldsymbol{x}, t) &= S_w \Phi\, \rho_w(\boldsymbol{x}, t) \\
\boldsymbol{v} &= \boldsymbol{v_{a\,w}} \\
\boldsymbol{J} &= \boldsymbol{J_w} \\
\bar{r} &= r_{f\,w}
\end{aligned}
\tag{3.5}
$$

m_w - mass of water [kg]
Φ - porosity [-]
S_w - volumetric fraction of the pore volume that is occupied by water [m³/m³]
ρ_w - density of water [kg/m³]
$\boldsymbol{v_{a\,w}}$ - interstitial water velocity [m/s]
$\boldsymbol{J_{f\,w}}$ - non-advective flow of water [kg/(m² s)]
$r_{f\,w}$ - production of water [kg/(m³ s)]

leads to the formulation

$$
\int_G \left[\frac{\partial (S_w \Phi\, \rho_w)}{\partial t} + \nabla \cdot \left(\boldsymbol{v_{a\,w}}\, S_w \Phi\, \rho_w + \boldsymbol{J_{f\,w}} \right) - r_{f\,w} \right] dV = 0 \tag{3.6}
$$

In the same way, a balance equation for the mass of ice can be derived. Adding both equations results in a balance equation for the whole system:

$$
\int_G \left[\frac{\partial (\Phi [S_w\, \rho_w + S_i\, \rho_i])}{\partial t} + \nabla \cdot (\Phi [\boldsymbol{v_{a\,w}}\, S_w\, \rho_w + \boldsymbol{v_{a\,i}}\, S_i\, \rho_i]) + \nabla \cdot \left(\boldsymbol{J_{f\,w}} + \boldsymbol{J_{f\,i}} \right) - r_{f\,w} - r_{f\,i} \right] dV = 0 \tag{3.7}
$$

S_i - volumetric fraction of the pore volume that is occupied by ice [m³/m³]
ρ_i - density of ice [kg/m³]
$\boldsymbol{v_{a\,i}}$ - interstitial ice velocity [m/s]
$\boldsymbol{J_i}$ - non-advective flow of ice [kg/(m² s)]
$r_{f\,i}$ - production of ice [kg/(m³ s)]

The same procedure has been executed for the heat energy as the extensive quantity, again carefully avoiding any premature introduction of assumptions and simplifications. In this case, balance equations must be formulated not only for water and ice but also

for the solid rock, called “matrix” further on, as the matrix is also involved in the spreading of heat.

With a view to heat production, this process is a little less straight forward as there are at least three possible ways to introduce (or loose) heat: a direct source within the domain in question, say by a waste canister, heat entering the domain in conjunction with inflowing water and the latent heat of melting/freezing. Adding all three balance equations reveals

$$\int_G \begin{bmatrix} S_w\,\Phi\rho_w \dfrac{\partial(c_{s\,w}\,T_w)}{\partial t} + S_i\,\Phi\rho_i \dfrac{\partial(c_{s\,i}\,T_i)}{\partial t} + (1-\Phi)\rho_m \dfrac{\partial(c_{s\,m}\,T_m)}{\partial t} \\ +(\boldsymbol{v_{a\,w}} S_w \rho_w \Phi)\cdot\boldsymbol{\nabla}(c_{s\,w}\,T_w) + \boldsymbol{v_{a\,i}} S_i\,\rho_i \Phi\ \cdot\boldsymbol{\nabla}(c_{s\,i}\,T_i) \\ +\nabla\cdot(\boldsymbol{v_{a\,m}}(1-\Phi)c_{s\,m}\,\rho_m T_m) + c_{s\,w}\,T_w \hat{r}_{f\,w} + c_{s\,i}\,T_i \hat{r}_{f\,i} \\ +\nabla\cdot(\boldsymbol{J_{h\,w}} + \boldsymbol{J_{h\,i}} + \boldsymbol{J_{h\,m}}) \end{bmatrix} dV \qquad (3.8)$$

$$= \int_G [r_{h\,w} + r_{h\,i} + r_{h\,m}]\, dV$$

c_{sp} - specific heat capacity of phase p [J/(kg K)]
T_p - temperature of phase p [K]
$\boldsymbol{J_{h\,p}}$ - non-advective flow of heat in phase p [J/(m² s)]
$r_{h\,p}$ - production of heat in phase p [J/(m³ s)]
ρ_p - density of phase p [kg/m³]
$\boldsymbol{v_{a\,p}}$ - velocity of phase p [J/(m² s)]
Index p: w – water, i – ice, m – matrix

Note that up to this point, no adaptation to specifically stated problems has been introduced. By equations (3.7) and (3.8), the above described “game board” is set.

3.4.3 Processes

Now, the book of rules must be compiled. The first chapter simply lists all processes and related conventions involved.

3.4.3.1 Mass balance

In case of the mass balance of water and ice in the pore space, the considered processes are: storage, advection and production of water but no non-advective fluxes like self-diffusion. A mass balance for the matrix has already been dropped which has

strictly speaking introduced a rule already implying a matrix that does not change or move on the macroscopic scale.

3.4.3.2 Heat energy balance

The balance of heat energy comprises storage, convection[6], conduction, thermo-hydraulic dispersion and production.

3.4.4 Constitutive Equations

The next chapter in the book of rules concerns the constitutive equations (CEs). These are material-specific relations of physical quantities that generally describe reactions triggered by any form of initiation. In the end, they basically concern empirical material properties. In this respect, the balance equations presented up to this point are therefore more or less derived on general principles, leaving appropriate functions and material parameters still to be specified.

Due to their empirical nature, the CEs are case-specific. There are either so-called laws like Darcy's law where a general relation must be specified by material-specific parameters or the relation itself is unique. In the latter case, only a general dependence on the primary variables can be given. The CEs required here are listed below:

- Porosity: Simplified to be a constant
- Flow law: Darcy's law using saturation-dependent reduction of the permeability[7]
- Water/ice saturation: A temperature-dependent SFCC
- Relative permeability: A saturation-dependent reduction function for the permeability
- Non-advective heat flow: Fouriers 2nd law
- Hydro-thermal dispersion: heat convection by hydraulic dispersion based on the Scheidegger approach

[6] advective heat transport by a fluid is usually called "convection"

[7] This is quite similar to the conventional unsaturated groundwater flow

3.4.5 Equations of state

The next entry in the book of rules concerns the equations of state (EOS). They relate the state of matter which is described by state variables such as density or thermal conductivity to physical conditions like pressure or temperature[8]. In principle, EOS apply to a vast range of physical conditions that is far too broad to apply to a specific problem. Practical restrictions are therefore provided later by the amendments (see subsection 3.4.6).

Two reports have been written in the past to compile formulations for state variables, /KRÖ 08/ and /KRÖ 10/. While all state variables that are of interest here were covered, the lowest temperature considered in these reports had only been 0 °C. Additional data have therefore been collected for water, ice and rock in the subzero temperature range down to -40 °C and compiled in /KRÖ 22/. Analytical formulations based on these data are combined with the already known formulations for temperatures above 0 °C. As a general illustration, the EOS are depicted in Fig. 3.5 for water and ice under atmospheric pressure in the temperature range of -20 °C < T < +200 °C using these analytical formulations[9]. Since the resulting formulations are quite complex, a set of simpler analytical functions valid for temperatures between -20 °C and +20 °C[10] as well as for pressures of up to 10 MPa are developed as well in order to increase computational efficiency /KRÖ 22/.

3.4.6 Amendments

Practical limits have to be defined that cover the expected conditions for the problem at hand to avoid excessive complexity. However, a careful choice is advisable as such limits also restrict the applicability of a model to other problems.

In the framework of this report, the amendments are being tailored to the international INTERFROST benchmark exercise /GRE 18/ that is strongly restricting the variability of

[8] Another influencing quantity could be the salinity of the groundwater, but salinity as well as other possible physicochemical conditions are left to be incorporated at a later time if need arises.

[9] Note that water under atmospheric pressure changes to vapour at a temperature of 100 °C

[10] 0 °C in case of ice

temperature and pressure. In this case, the ranges of interest with respect to temperature and pressure are defined as

$$-5\,°C < T < +5\,°C$$
$$100\,000\,Pa < p < 100\,883\,Pa \qquad (3.9)$$

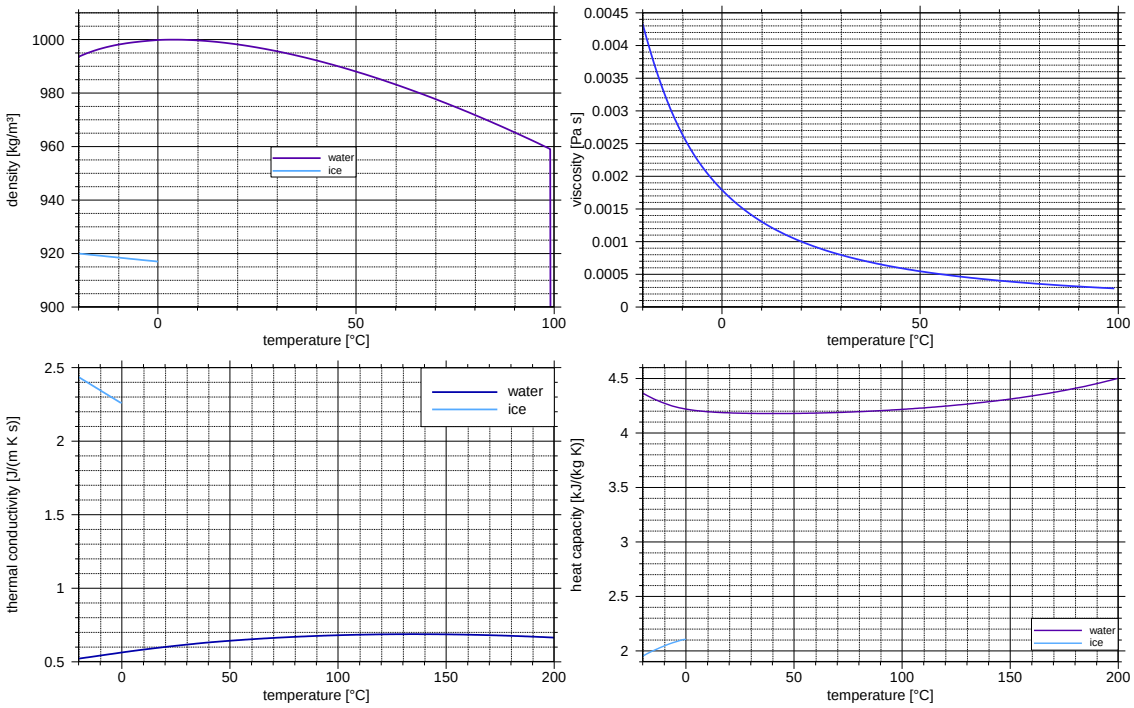

Fig. 3.5 Density (top left), viscosity (top right), thermal conductivity (bottom left), and heat capacity (bottom right) for water and ice, where applicable

3.4.7 Mathematical model for the INTERFROST benchmarks (The Game)

The international INTERFROST-project /GRE 18/ has been set up as a code comparison exercise with respect to groundwater flow under freezing conditions. It was based on several test cases where the latest two were 2D-problems considered to be “more complex scenarios“ that took heat flow, water flow and freezing/melting of the water into account.

The test descriptions did neither include any water or heat sources nor a thermo-hydraulic heat dispersion. The admissible range of pressures is highly restrictive which means that any function of the pressure can be dropped as well. For the rather narrow range of temperatures, many dependencies of the EOS on temperature can be neglected:

$$\Phi = const.$$

$$S_w = S_w(T)$$

$$k_{rw} = k_{rw}(S_w(T))$$

$$\boldsymbol{v_{a\,w}} = \boldsymbol{v_{a\,w}}\left(\boldsymbol{v_{f\,w}}\left(k_{rw}(S_w(T))\right), S_w(T), \Phi, g, \rho_w, \eta_w, p_w\right)$$

$$\boldsymbol{J_{cond\,j}} = \boldsymbol{J_{cond\,j}}(S_j(T)^{11}, \boldsymbol{\Phi}, \lambda_j, T),\ \text{j = w, i, m} \qquad (3.10)$$

$$\boldsymbol{J_{disp\,w}} = 0$$

$$\begin{array}{lll} \rho_w = const. & \rho_i = const. & \rho_m = const. \\ \eta_w = \eta_w(T) & & \\ \lambda_w = \lambda_w(T) & \lambda_i = const. & \lambda_m = const. \\ c_{s\,w} = const. & c_{s\,i} = const. & c_{s\,m} = c_{s\,m}(T) \end{array}$$

All these assumptions allow for simplifying the balance equations (3.7) and (3.8) to

$$-\nabla \cdot \left(\rho_w \frac{k_{rw}}{\eta_w} \boldsymbol{k} \cdot (\boldsymbol{\nabla} p_w - \rho_w \boldsymbol{g}) \right) = -\Phi(\rho_w - \rho_i) \frac{\partial S_w}{\partial T} \frac{\partial T}{\partial t} \qquad (3.11)$$

and

$$\begin{pmatrix} S_w\,\Phi \rho_w c_{s\,w} + S_i\,\Phi \rho_i c_{s\,i} \\ +(1-\Phi)\rho_m \left[T \frac{\partial c_{s\,m}}{\partial T} + c_{s\,m} \right] - L\rho_i \Phi \frac{\partial S_i}{\partial T} \end{pmatrix} \frac{\partial T}{\partial t} + (\boldsymbol{v_{a\,w}} S_w \rho_w \Phi\, c_{s\,w}) \cdot \boldsymbol{\nabla} \mathrm{T} \qquad (3.12)$$
$$-\nabla \cdot [(S_w \Phi\, \boldsymbol{\lambda_w} + S_i \Phi\, \boldsymbol{\lambda_i} + (1-\Phi)\, \boldsymbol{\lambda_m}) \cdot \boldsymbol{\nabla} T] = 0$$

respectively. Balance equations (3.11) and (3.12), constitutive equations and the EOS (3.10) together with the amendments (3.9) now define the “game: modelling INTERFROST benchmarks”.

[11] Where applicable

3.5 Implementation Aspects and Model Validation

The thermo-hydraulic flow model has been investigated in two 2D benchmark experiments from /GRE 18/. This section reports on key findings. More details can be found in /MÖL 22/.

Tab. 3.1 Model parameters /GRE 18/

Symbol	Constant	Value	Unit
ϕ	Porosity	0.37	1
	Conductivity		W / (m K)
λ_w	Water	0.6	
λ_i	Ice	2.14	
λ_s	Soil	9	
	Heat capacity		J / (kg K)
c_w	Water	4,182	
c_i	Ice	2,060	
c_s	Soil	835	
	Density		kg / m^3
ρ_w	Water	1000	
ρ_i	Ice	920	
ρ_s	Soil	2650	
μ	Viscosity	$1.793 \cdot 10^{-3}$	kg / (m s)
L	Latent heat	334,000	J / kg

Constitutive relations are defined according to /MCK 13/: Water saturation is a function of temperature:

$$S_w(T) = \begin{cases} 1 & T > 273.15\text{K} \\ 0.05 + 0.95 \exp\left(-\left\{\frac{T - 273{,}15\text{K}}{0.5\ K}\right\}^2\right) & T \leq 273.15\text{K} \end{cases} \qquad (3.13)$$

and relative permeability for fluid flow depends on saturation:

$$k(S_w) = \max\left\{10^{-6}, 10^{-\phi\ 50\ (1-S_w)}\right\}.$$

3.5.1 TH2 Benchmark

The TH2 benchmark simulates the situation in of a block of ice thawing in rectangular a water channel. The flow conditions are controlled by different pressure gradients. The challenges for this benchmark are (i) to determine the time for thawing, (ii) measuring the amount of water in the system and (iii) to control the net heat flux into the system.

3.5.1.1 Description

The geometry is depicted in Figure 3.6: Initially an ice cube of size 1/3 m x 1/3 m is placed in the first part of a channel, which is 3 m long and 1 m high. The temperature is T=-5 °C for the ice block and T=5 °C for the surrounding water.

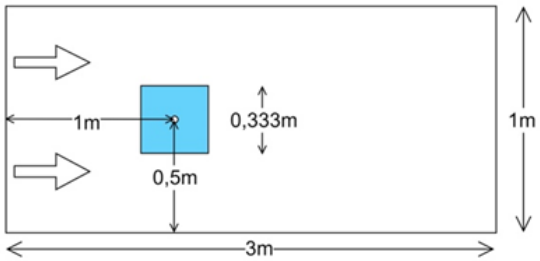

Fig. 3.6 TH2-Benchmark: Sketch of the geometry

Top and bottom wall are considered impermeable. Fluid flow results from a pressure gradient that is applied form left to right: Pressure is set to zero at the outlet on the right side and given by a value corresponding to an elevation that is given by the slope of the plane between inlet and outlet. Various slopes between 0-20 % are considered. While temperature at the inlet is fixed to T=5 °C, a condition guaranteeing zero conductive heat flux is imposed at the outlet, i.e., heat is transported by convection only.

3.5.1.2 Numerical Results

Figure 3.7 illustrates a typical profile. The applied pressure gradient of 3 %, results in a convective flow field around the ice region. Due to melting, the exterior shape of the initial cube turned into a cylinder already. Moreover, temperature in the interior approached T=-1 °C already, which is the offset for latent heat in the constitutive relations.

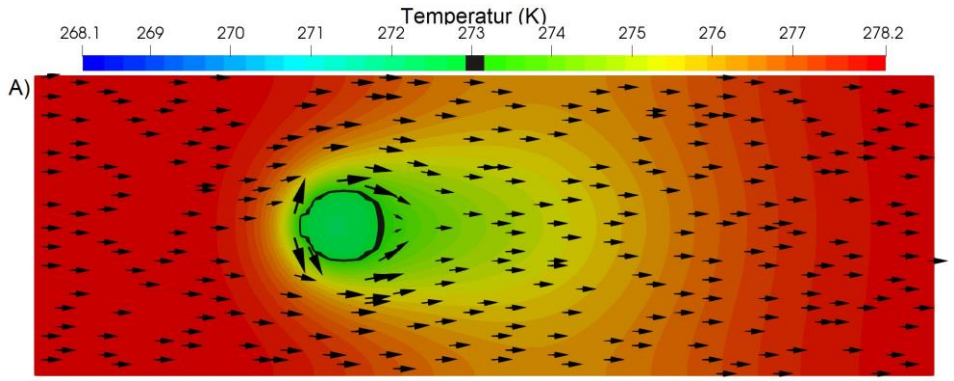

Fig. 3.7 TH2-Benchmark: Illustration of an intermediate step (3 % pressure gradient). Freezing point temperature T=0 °C is indicated by black color.

Figures 3.8, 3.9, and 3.10 provide details on the temporal evolution of different quantities of interest when various pressure gradients (0 %, 1 %, 2 %, 3 %, 6 %, 9 %, 12 %, 15 %, 20 %) are applied.

Minimum temperature in the system is shown in Figure 3.8: In an initial phase, which is similar for all gradients, the system rapidly approaches the zone at T=-1 °C where melting starts. The duration of this melting phase depends on the velocity of the flow: The larger the pressure gradient, the faster cold fluid is transported away from the ice by advection. As a result, the ice cube melts more rapidly.

The melting point can also be identified in Figure 3.9, which illustrates the development over time for the volume of the fluid. Starting from the configuration with the embedded ice cube, the volume gradually approaches the limit of 1.11 $m^3 = \phi * 3\ m^3$.

Finally, the net heat flux is investigated in Figure 3.10: The curves show that for melting the ice, initially heat is imported into the system. Even after the melting point has been reached, it takes some time to replace the cold water by water with the influx temperature of T=5 °C. The larger the pressure gradient, the shorter is the time for a complete washout and the larger is the peak for the net flux.

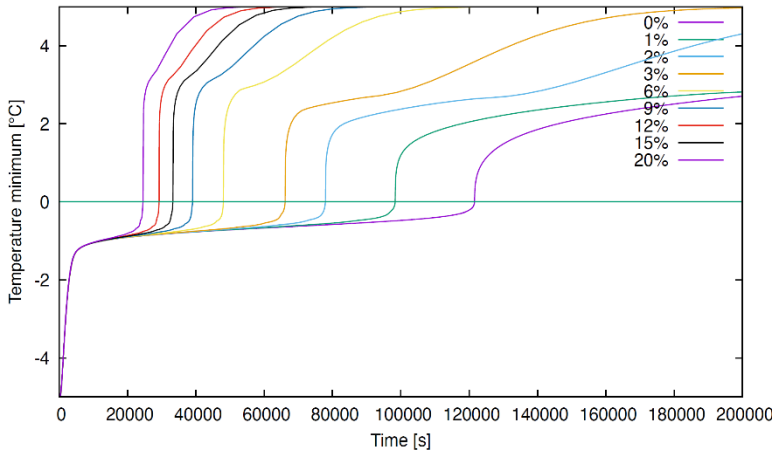

Fig. 3.8 TH2-Benchmark: Illustration of temperature minimum

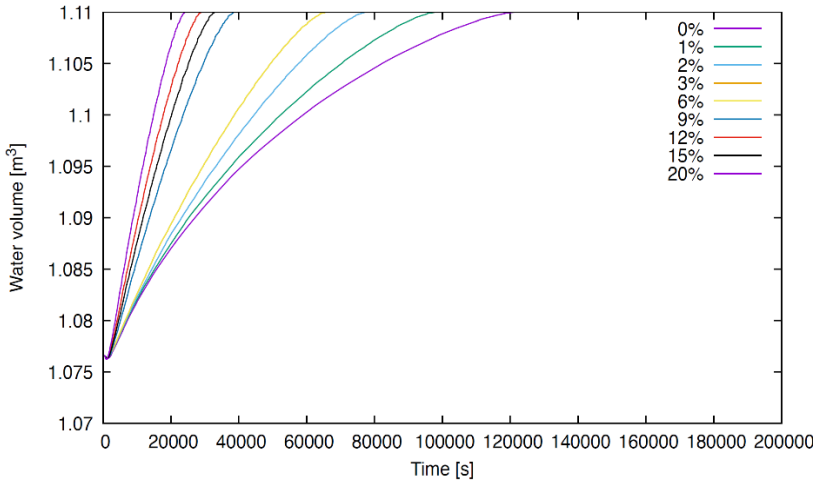

Fig. 3.9 TH2-Benchmark: Illustration of water volume

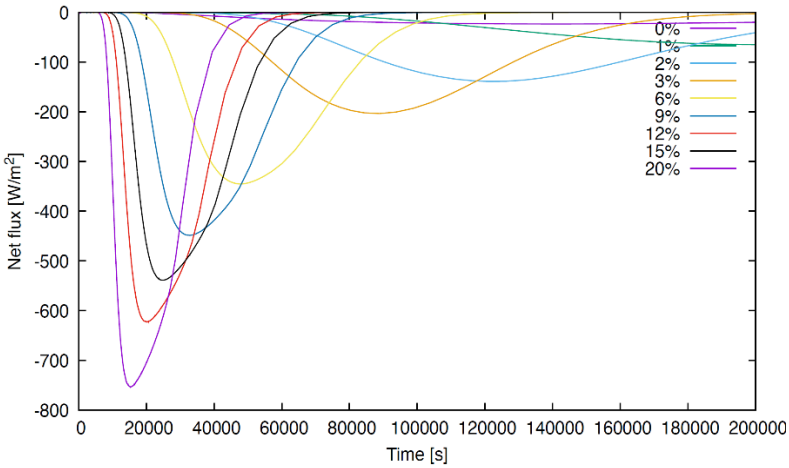

Fig. 3.10 TH2-Benchmark: Illustration of net flux

3.5.2 TH3 Benchmark

The motivation for the TH3 benchmark is modelling a Talik, i.e., an unfrozen area between two frozen zones. Similar to the previous benchmark, a flow from left to right is

imposed. Depending on the strength of the pressure gradient, this results in a *Talik closure* by freezing, or to in a Talik opening due to thawing. Details on benchmark computations are provided below.

3.5.2.1 Description

The primary geometry is a unit square with edge length L_x=L_y=1 m as depicted in Fig. 3.11. Initially the domain is filled with two symmetric spherical regions of ice, which are depicted in blue. The radius of the spheres is R = 0,5099 m; the center lies outside the domain and can be described by the parameters L_{CX} = 0,5 m and L_{CY} = 0,1 m. To the right, the domain is extended by a secondary domain, which has been added for outflow conditions.

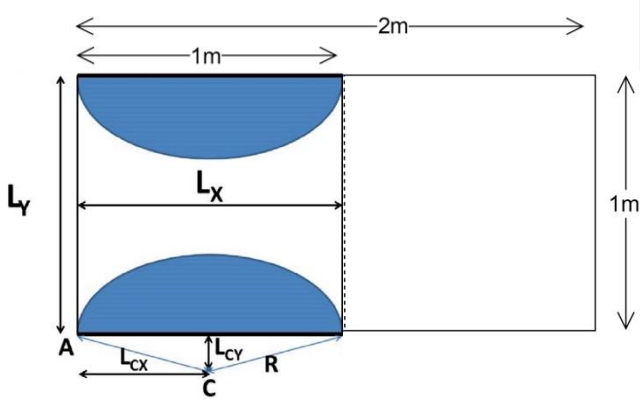

Fig. 3.11 TH3-Benchmark: Sketch of the geometry

Boundary conditions are similar to the TH2 benchmark: From left to right, a pressure gradient is applied by Dirichlet boundary conditions for the pressure. For the temperature the temperature is fixed to T=5 °C for the inlet at the left; the condition for zero conductive at the outlet is modelled by extending the domain to the right. On top and bottom, a Dirichlet boundary condition fixed to T=-5 °C is applied. This model frozen ice in this region. As before, a no flow condition is used for the pressure.

3.5.2.2 Numerical Results

Figure 3.12 shows typical profiles illustrating the evolution: For a pressure gradient of 2 %, the Talik is open initially (A), but then closes due to freezing (B) after some time. Here fluid flow is not strong enough to maintain an open Talik. For a larger pressure gradient of 14 %, the behavior in the initial phase (C) is similar. However, as the flow is stronger now, the Talik widens over time (D) and remains open.

This behavior is investigated in greater detail in Figure 3.13: The diagram shows the temperature at center point between the two ice spheres at position (0.5, 0.5) as a function of time.

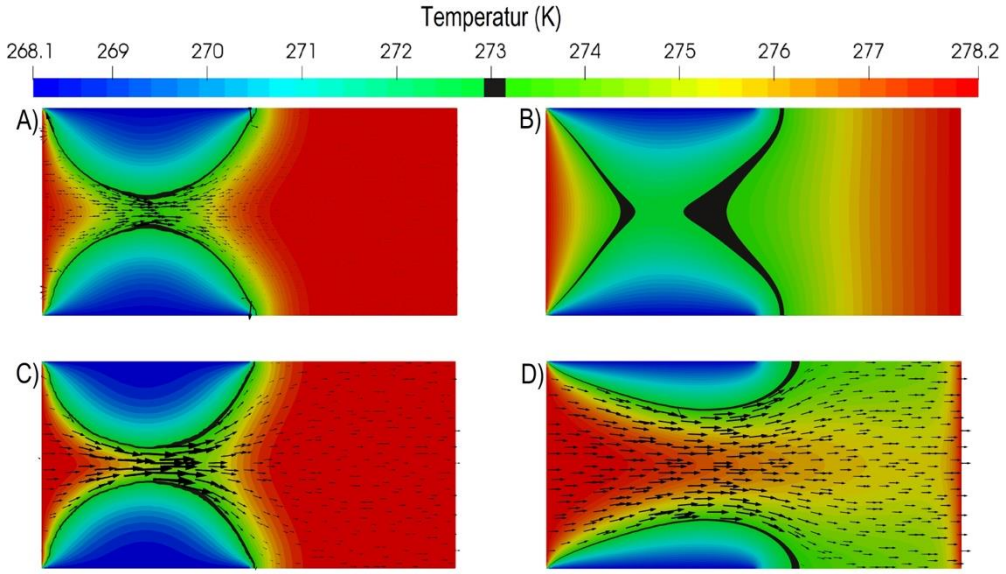

Fig. 3.12 TH3-Benchmark: Visualization of temperature distribution and flow field. Top: Low pressure gradient (2 %) results in a Talik closure; bottom: high pressure gradient (14 %) results in Talik opening.

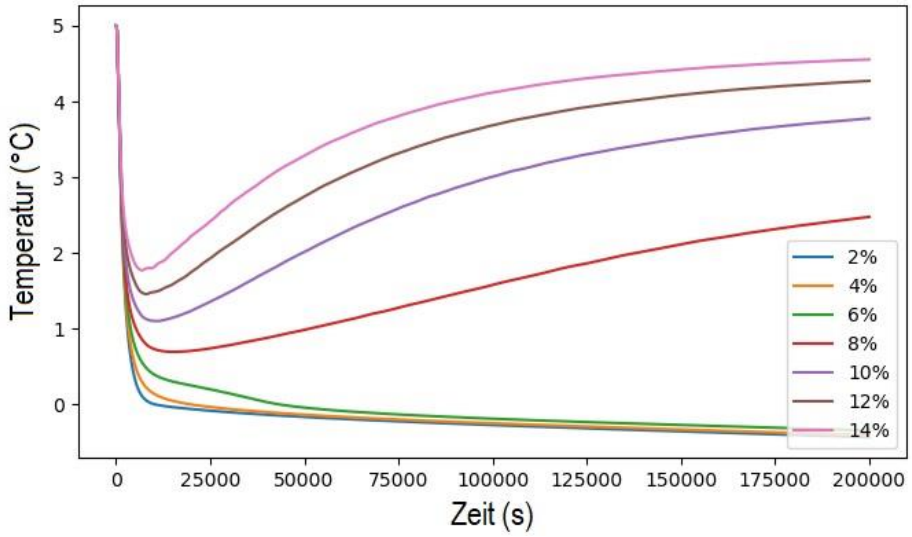

Fig. 3.13 TH3-Benchmark: Talik closure or opening depends on the applied pressure gradient. The critical value is between 6 % and 8 %, which is in agreement with the findings in /GRE 18/.

3.5.3 Discussion

For the model suggested /GRE 18/ the results presented for both the TH2 and TH3 benchmark are in good agreement. It must be kept in mind, however, that this model uses a storage term for the heat equation in simplified form. Further investigations in /SCH 22/ (data not shown) showed that in a full model the retardation effect by latent heat is even larger. Both models are now available in d³f++.

4 Numerical improvements in d³f++

Numerical improvements are of utmost importance for further improvement of d³f++, since more and more detailed simulation are highly demanding. In particular robustness in the parallel case is not yet satisfying. In the present project also has been worked on this issue. As is well known, robustness in multigrid methods can be achieved in several ways. For multigrid to work, two basic properties are necessary. The smoother has to reduce all high-frequency components of the error and the coarse-grid correction has to approximate all the error components which are left after smoothing. If multigrid fails, one of these properties is not fulfilled any more. The concept of robust smoothing for singularly perturbed problems changing type when a critical parameter ε reaches the limit, typically 0, says, that a robust smoother is obtained, if the smoother solves the limiting problem exactly. In many cases, this is easier than it seems. E.g. in case of dominating convection $-\varepsilon\Delta u + \vec{v} \cdot \nabla u$ with small ε a Gauss-Seidel smoother will be exact in the limit case $\varepsilon \to 0$, if we order the grid points in flow direction and use an upwind scheme for the discretisation, as elaborated in BEY 95/. A corresponding method can be used for anisotropic diffusion on structured grids, /WIT 89/.

4.1 Improvement of the robustness of solvers/AMG-GMG-combination

The goal of the present task is to generalise this idea to density-driven flow. To that end, we introduced ordering strategies from /BEY 95/ and /REN 96/. into d³f++. These strategies are already useful. A general reordering algorithm of unknowns was made possible by embedding parts of the boost library into d³f++. This was done in Task 4.2. Based on this work, several reorderings are possible. The biggest problem in this approach is parallelisation, since reordering may interfere with data partitioning for parallelisation. This still works fine with anisotropic problems using a locally adapted gridding in thin layers. This is solved by our current approach. With convection dominated flow, however, using downwind numbering from /BEY 95/, data partitioning may lead to contradicting demands. Here further work is necessary.

4.2 Software integration and re-structuring

To enable general reordering algorithms for the sparse matrices, parts of the boost library were embedded into d³f++. The BGL (Boost Graph Library) interface allows the

execution of generic graph algorithms for matrices stored in the d³f++ sparse matrix format (CSR). This also works for sparse matrices distributed on a parallel computer.

Some algorithms for sorting were rewritten, e.g. the bucket sorter from treedec was newly implemented, removing a bug in the original implementation. This bucket sorter is used in several algorithms in d³f++ now.

Additional methods were implemented, which are useful for working with sparse matrices. For transposing a sparse matrix on a parallel computer, e,g., a new and more elaborate algorithm was implemented which speeds up this operation up to 500 times.

An important part of the restructuring of the software was porting a large part of the functionality which was available only in LUA up to now. Parts of the refine utility and the partitioning utility are now available in C++. The new code has been tested with the d³f++ apps. In total, al large part of the LUA functions has been reimplemented and ported to C++, yielding a substantial improvement over the LUA implementation. For the LUA tables, a solution has been constructed, too. In total the following functions have been ported:

- util.d3f.ComputeFSVolume
- util.d3f.ComputeSDF
- util.d3f.InitLSF
- util.d3f.PrepareLSF
- util.d3f.parse.Upwind
- util.d3f.parse.Gravity
- util.d3f.CreateRiverRechargeObject
- util.d3f.SetFSBoundaryCond
- util.d3f.SetUpFreeSurfaceData (partially)
- util.d3f.solve (partially))
- util.d3f.ComputeFSVolume
- util.d3f.ComputePWFSVolume
- util.d3f.SetFixedLSValues
- util.CreateTimeDisc
- util.CreateDomain
- util.CheckSubsets
- util.SolveLinearTimeProblem
- util.SolveNonLinearTimeProblem

The ported routines have been tested with several of the recent d³f++ test cases. Thus, the restructuring of al large part of the software has been performed successfully.

4.3 Stabilization of the level-set method

In the considered benchmarks, as for ex. Kraví Hora, the thickness of the partially saturated zone is negligible in the scales of the entire model. In this case, from the point of view of modelling and numerical methods, it makes sense to reduce the dimensionality of this zone and consider the so-called phreatic surface that separates the fully saturated subregion from the partially saturated one. The flow is then simulated only in the fully saturated zone, and the phreatic surface is therefore a moving boundary of this subdomain. For the potential flow where the density of the fluid phase is constant, this approach has been discussed in /FRO 12/. Its generalization for the density-driven flow has been implemented in d³f++ and used for the Sandelermöns model, cf. /SCH 18/. However numerical tests for several real-world settings demonstrated an essential restriction in the applicability of this method: If the time step exceeds a certain value, the numerically computed moving boundary suffers of oscillations that lead to a completely wrong numerical solution. This error occurs not only in the position of the phreatic surface but also in the spatial salt distribution in the domain. Furthermore, it affects the convergence behavior of the solvers. Whereas reduction of the time step improves the situation, the stability condition in the simulation of the flow in some aquifers is so restrictive that the long-term predictions become technically almost impossible.

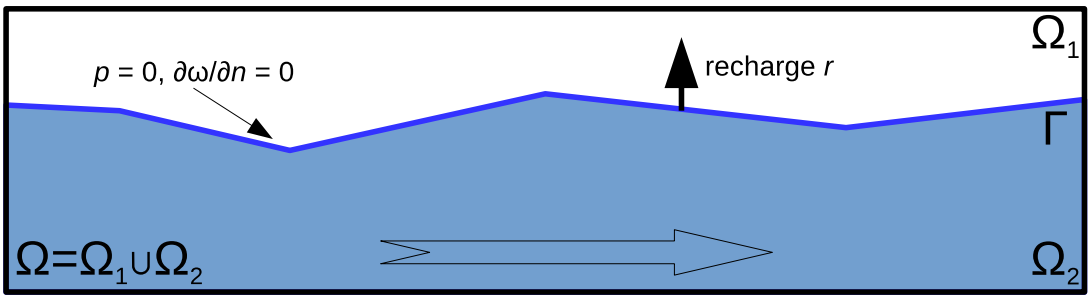

Fig. 4.1 Scheme of the geometry in the modelling of the density-driven flow with a phreatic surface using the level-set method: The phreatic surface Γ separates the subdomains Ω_1 and Ω_2. The flow and transport are computed only in Ω_2 for which Γ is a moving boundary.

It has been found out that the source of the instability is the loose coupling (cf. /NAE 19/) of the flow and transport equations with the level-set equation. This method is only conditionally stable but its choice is dictated by the nature of the level-set method.

In detail, denote the entire simulation domain by $\Omega \subset \mathbb{R}^d$ and the time-dependent phreatic surface by $\Gamma(t) \subset \Omega$. This phreatic surface subdivides Ω into the unsaturated part $\Omega_1(t)$ and the fully saturated part $\Omega_2(t)$, cf. Fig. 4.1. We introduce the level-set function $\psi: [0,T] \times \Omega \to \mathbb{R}$ defined in the entire domain Ω so that for every t, $\psi(t,x) > 0$ for $x \in \Omega_1(t)$, $\psi(t,x) < 0$ for $x \in \Omega_2(t)$ and $\psi(t,x) = 0$ only for $x \in \Gamma(t)$.

For the fluid phase, only in the subdomain Ω_2, we consider equations of the density-driven flow

$$\begin{aligned} &\partial_t(\Phi\rho\omega) + \nabla \cdot (\rho\omega\boldsymbol{q} - \rho D\nabla\omega) = 0, \\ &\partial_t(\Phi\rho) + \nabla \cdot (\rho\boldsymbol{q}) = 0, \end{aligned} \qquad (4.1)$$

where $\boldsymbol{q} = -\frac{\boldsymbol{K}}{\mu}(\nabla p - \rho\boldsymbol{g})$ is the Darcy velocity, $\rho = \rho(\omega)$ the density, $\mu = \mu(\omega)$ the viscosity of the fluid phase, ω the mass fraction of the salt, p the pressure, Φ and $\boldsymbol{K}$ the porosity and the permeability of the matrix. The system of the PDEs (4.1) should be closed by the boundary and initial conditions. In particular, on $\Gamma(t)$, we impose the Dirichlet boundary condition $p = 0$ and the Neumann-0 boundary condition $\frac{\partial\omega}{\partial n} = 0$, cf. Fig. 4.1.

The interface Γ is moving with the linear velocity $\tilde{\boldsymbol{q}} = (\boldsymbol{q} + r\boldsymbol{e}_z)/\Phi$, where r models the groundwater recharge. Note that to describe this motion, it suffice to specify only the normal velocity $\tilde{q}_n = \tilde{\boldsymbol{q}} \cdot \boldsymbol{n}$, evaluated on Γ, where $\boldsymbol{n}$ is the normal to Γ pointing to Ω_1, cf. /FRO 12/. The normal Darcy velocity is well-defined on the boundary (as the normal derivative of the pressure is). Due to the definition of ψ, we have: $\boldsymbol{n} = \nabla\psi/|\nabla\psi|$. The evolution of ψ that provides the desired motion of Γ is modelled by the level-set equation

$$\psi_t + u_n|\nabla\psi| = 0, \qquad (4.2)$$

where the normal velocity field u_n should be consistent with $\tilde{q}_n$ on Γ:

$$u_n = \tilde{\boldsymbol{q}} \cdot \frac{\nabla\psi}{|\nabla\psi|}, \quad x \in \Gamma. \qquad (4.3)$$

However, (4.2) requires global definition of u_n whereas (4.3) provides only a local one. Usage of (4.3) in the entire domain is not possible because $\tilde{\boldsymbol{q}}$ is undefined in Ω_1. Even in Ω_2, taking the values of (4.3) out of the interface would produce undesired artefacts

and would require periodic reinitialization of ψ. Instead, in d³f++, we extend the values of u_n from Γ towards the other parts of the domain.

To this end, at every time t, for the interface $\Gamma(t)$ specified by $\psi(t,x)$, we compute the signed distance function $\hat{\psi}$ by solving the eikonal equation

$$\left|\nabla\hat{\psi}\right| = 1, \quad s.t.\ \hat{\psi}(x) = 0, x \in \Gamma. \tag{4.4}$$

Using $\hat{\psi}$, we then find $u_n: \Omega \to \mathbb{R}$ by solving the stationary hyperbolic equation

$$\frac{\nabla\hat{\psi}}{|\nabla\hat{\psi}|} \cdot \nabla u_n = 0, \quad x \in \Omega \tag{4.5}$$

with the boundary condition (4.3). The overall procedure for the computation of a time step of the computation can be therefore represented as follows:

For the current position of the interface $\Gamma = \Gamma(t_{old})$, specified by $\psi(t_{old}, x)$, compute the new solution of the system (4.1) for ω_{new}, p_{new} and get $\widetilde{\boldsymbol{q}} = \widetilde{\boldsymbol{q}}(\omega_{new}, p_{new})$.

Compute the signed distance function $\hat{\psi}$ by solving (4.4) for $\Gamma = \Gamma(t_{old})$.

Compute $u_n = u_n(t_{new}, x)$ by solving (4.5) with the fixed $\hat{\psi}$ and the boundary condition (4.3) for $\Gamma = \Gamma(t_{old})$ and $\widetilde{\boldsymbol{q}} = \widetilde{\boldsymbol{q}}(\omega_{new}, p_{new})$.

Using this field u_n, do one time step of the level-set equation (4.2) to get $\psi(t_{new}, x)$ and therefore the new position of the interface $\Gamma = \Gamma(t_{new})$.

Using the fixed velocity $\widetilde{\boldsymbol{q}}$ computed at the step 1 of this approach in the steps 2 – 4 causes amplifications of the small oscillations in ψ that arise due to the discretization and floating-point errors if the time step is too long. A remedy would be the monolithic coupling of equations (4.1) and (4.2). However, this is not possible because of the computation of the extended velocity.

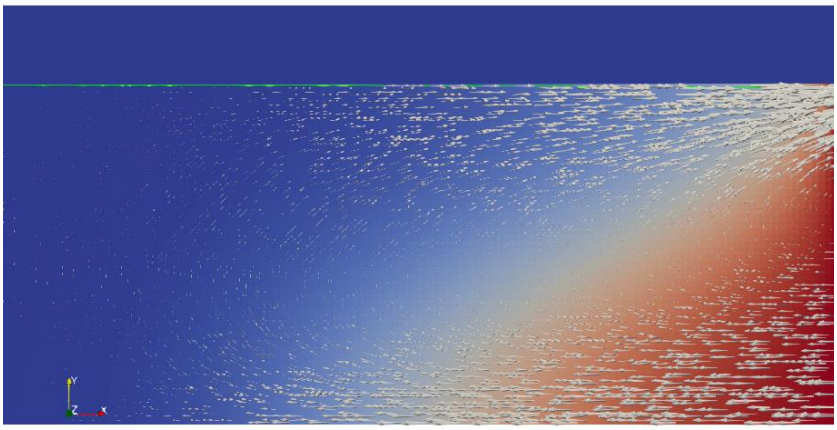

a.

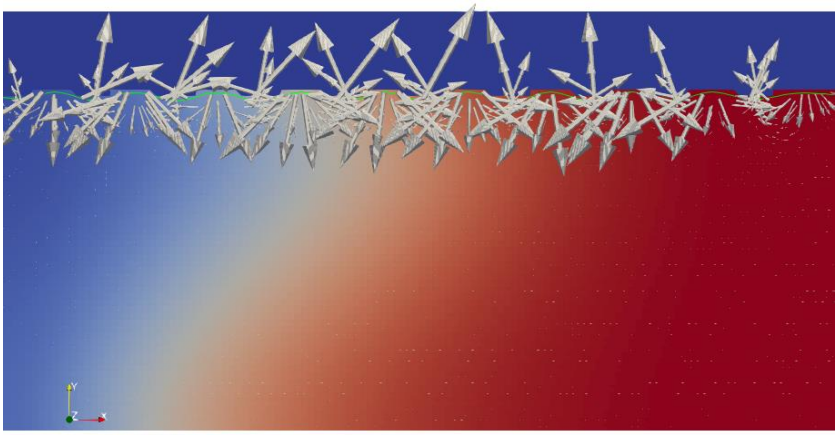

b.

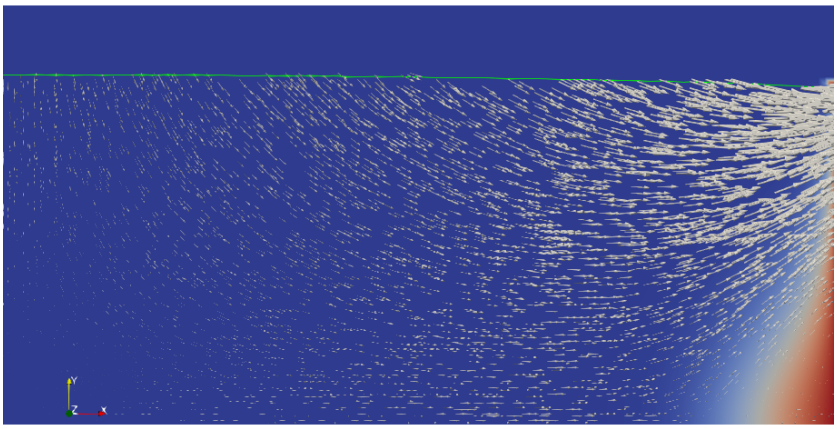

c.

Fig. 4.2 Computation of the Henry problem (no recharge) with the stabilized level-set method with different time step length and values of the stabilization parameter: (a) $\Delta t = 2.5[s]$, $\epsilon = 0.00005$, (b) $\Delta t = 5[s]$, $\epsilon = 0.00015$ and (c) $\Delta t = 5[s]$, $\epsilon = 0.00025$

To avoid this instability, we introduce an additional stabilizing diffusion term in (4.2). Then this equation attains the form

$$\psi_t + u_n|\nabla\psi| - \epsilon\Delta\psi = 0, \qquad (4.6)$$

where $\epsilon \geq 0$ is a small stabilization parameter. Equation (4.6) replaces (4.2) in the computations. Parameter ϵ depends on the spatial and temporal grids. As the grids are refined, ϵ must tend to 0. Note that (4.6) is a convection-diffusion equation, and its numerical solution does not lead to any difficulties in the numerical methods. However, in contrast to (4.2), it requires an implicit discretization of the diffusion term and therefore a linear solver.

The effect of the stabilization is demonstrated in Fig. 4.2. We consider the standard Henry problem but introduce the (initially horizontal) phreatic surface on the upper part of the domain and set the recharge (through the left boundary as well as at the phreatic surface) to 0. Fig. 4.2(a) shows the well-stabilized computation of the flow and transport. (For the time step $\Delta t = 2.5[s]$, this computation shows instabilities without the stabilization.) In this case, the phreatic surface has already reached its steady state, and the flow at it is parallel to it.

However, increasing the time step leads to the instabilities again if the stabilization parameter ϵ is not large enough, s. Fig. 4.2(b). As we see, the oscillations of the numerical phreatic surface led to the spurious currents and non-physical transport of the salt.

Enlarging ϵ stabilizes the solution, s. Fig. 4.2(c). However, one should beware the possible overstabilization if ϵ is increased too much. Fig. 4.2(c) demonstrates this: Whereas the phreatic surface has already achieved its steady state, the flow is not parallel to it. This results numerically in the artificial recharge that causes the non-physical washout of the salt. (Other experiments show that the artificial recharge may be positive or negative.)

Summarizing, the proposed stabilization technique has allowed to overcome the restriction for the time step length and therefore chose the reasonable time step in some benchmarks. However, up to now, the stabilization parameter should be chosen manually, and further research is necessary for determining its optimal value.

4.4 Phase-field modeling of phreatic groundwater surfaces

The level-set method presented in Section 4.3 moved the phreatic surface using an additional auxiliary equation directly. As mentioned earlier, the surface can be described as the level-set $\Gamma = \{x \in \Omega : \mathrm{p}(\mathrm{x}) = 0\}$. The following presentation, this characterization will be used to formulate the problem without an additional level-set. Instead, the movement of the phreatic surface is incorporated into the governing equations directly. This can be achieved using the notion of flow in unsaturated media /BEA 10/, /CON 22a/, /CON 22b/.

4.4.1 Unsaturated porous media

In unsaturated media, the pores are not only filled with water, but contains a certain amount of air. Note that a similar problem was already encountered in Section 3, where, in the context of thermo-hydraulic flow, pores were filled with mixture of water and ice. The key here was to introduce a saturation of water and ice respectively. Similarly, the approach here will be extended to mixtures of water and air.

4.4.1.1 Water content and saturation

For a proper derivation, consider a representative elementary volume (REV) consisting of a matrix space and void space. The void space is partly filled with water and air respectively. These phases are denoted by subscripts $\alpha = w,a$. For this REV, let $\mathrm{V}, \mathrm{V}_0, \mathrm{V}_\alpha$ denote its bulk volume, the volume of the void space and the volume of the α-phase

$$\begin{aligned} \phi &:= \frac{\mathcal{V}_0}{\mathcal{V}}, \quad 0 < \phi \leq 1, \\ S_\alpha &:= \frac{\mathcal{V}_\alpha}{\mathcal{V}_0}, \quad 0 < S_\alpha \leq 1, \\ \theta_\alpha &:= \frac{\mathcal{V}_\alpha}{\mathcal{V}} = S_\alpha \phi, \quad 0 < \theta_\alpha \leq \phi. \end{aligned} \tag{4.7}$$

respectively. For $\alpha = w,a$, we define the non-dimensional quantities /BEA 10/:

By definition the following identity holds:

$\theta_w + \theta_a = \phi, S_a + S_w = 1.$

Depending on the properties of the porous medium, the water saturation can be expected to be bounded from below and above by a *residual saturation* S_r and the *maximum saturation* S_s respectively:

$$0 < S_r \leq S_w \leq S_s \leq 1,$$

Then the *effective water content* $0 \leq \Theta \leq 1$ is defined as

$$\Theta = \frac{S_w - S_r}{S_s - S_r} \qquad (4.8)$$

which yields an equivalent expression for the water saturation $S_w(\Theta) := S_r + (S_s - S_r)\Theta$.

4.4.2 Capillary pressure

The vadose (or unsaturated) zone is the part of the soil matrix which is between the surface and the water table. In this region the water pressure p is less than the atmospheric pressure p_a. This zone must be distinguished from the phreatic (or saturated) zone, where $p > p_a$ and all pores and fractures are filled with water.

Based on the *capillary pressure* p_c

$$p_c := p_a - p.$$

the vadose zone ($p_c > 0$) and the phreatic zone ($p_c < 0$) can be distinguished easily. The region with $p_c = 0$ defines the phreatic surface /CHE 08/. For air, we can assume $\frac{p_a}{p} \ll 1$, which yields the approximation

$$p_c \approx -p.$$

4.4.3 Retention curves

The transport properties in the vadose zone are expressed by the aforementioned saturation S and a relative permeability k. Both are non-dimensional quantities with

$$0 \leq S \leq 1,\ 0 \leq k \leq 1.$$

For S = 1 and k=1 the porous medium is fully saturated. For characterizing the partially saturated vadose zone, constitutive relations are used. These have historically often been defined based the *capillary pressure head*

$$\psi := \frac{p_c}{\gamma}, \gamma := \rho|\mathbf{g}|$$

This quantity corresponds to capillary pressure p_c up to a scaling. The scaling factor is defined using the fresh water density ρ and the acceleration $\mathbf{g}$, i.e., the capillary pressure head has the unit of a length and technically corresponds to the height of the water level in a suction tube filled with fresh water above the phreatic surface.

Exponential model. A simple model, which is primarily of theoretical interest, uses exponential functions /PUL 90/. The saturation is given by (4) in combination with

$$\Theta(\psi) = \begin{cases} \exp(-\alpha\psi), & \text{if } p_c > 0 \\ 1, & \text{if } p_c \leq 0. \end{cases}$$

Similarly, the soil permeability is expressed as $\mathbf{K}_{vad}(\psi) = \mathbf{K}_{sat}k(\psi)$ with

$$k(\psi) = \begin{cases} \exp(-\beta\psi), & \text{if } p_c > 0 \\ 1, & \text{if } p_c \leq 0. \end{cases}$$

Note that $k(\psi) = \Theta(\psi)_{\alpha-}$ and ideally $\beta \geq \alpha > 0$. In particular the case $\alpha = \beta$ is of theoretical interest, as it permits a solution using a Kirchhoff transformation /SRI 91/.

Van-Genuchten-Mualem model. A more realistic model is the Van Genuchten-Mualem-model /MUA 76/, /VAN 80/. In this case, the saturation S is given by (4) in combination with

$$\Theta(\psi) = \begin{cases} \left(\frac{1}{1+(\alpha\psi)^n}\right)^m, & \text{if } p_c > 0 \\ 1, & \text{if } p_c \leq 0, \end{cases}$$

with soil specific model parameters α, n and m. Often $m = 1 - \frac{1}{n}$ is used.

Relative permeability k is then given by the empirical law

$$k(\Theta) = \Theta^{1/2}\left(1 - \left(1 - \Theta^{\frac{1}{m}}\right)^m\right)^2.$$

4.4.4 Relationship to the level-set method

In the special case with ρ =const the second equation in (2.1) reduces to the well-known Richards' equation /RIC 31/. Expressing the derivatives by the chain rule yields

$$\frac{\partial S}{\partial p}\frac{\partial p}{\partial t} + \frac{\partial k}{\partial p}\nabla p \cdot \mathbf{q}_{sat} + k\nabla \cdot [\mathbf{q}_{sat}] = \frac{q_V}{\phi}$$

where $\boldsymbol{q}_{\{\boldsymbol{sat}\}} = -\frac{\boldsymbol{K}}{\mu}(\nabla p - \rho \mathbf{g})$. For the saturated zone, this reduces to a potential equation:

$$\nabla \cdot [\overline{\mathbf{q}}_{sat}] = \frac{q_V}{\phi}$$

For the vadose zone, the exponential model yields:

$$\alpha'(S_s - S_r)\exp(\alpha' p)\frac{\partial p}{\partial t} + \beta' \exp(\beta' p)\nabla p \cdot \mathbf{q}_{sat} + \exp(\beta' p)\nabla \cdot [\mathbf{q}_{sat}] = 0$$

or

$$\frac{\partial p}{\partial t} + \frac{\beta}{\alpha}\frac{\exp\left((\beta-\alpha)p/\gamma\right)}{(S_s - S_r)}\nabla p \cdot \overline{\mathbf{q}}_{sat} + \underbrace{\frac{\gamma}{\alpha}\frac{\exp\left((\beta-\alpha)p/\gamma\right)}{(S_s - S_r)}}_{:=D}\nabla \cdot [\overline{\mathbf{q}}_{sat}] = 0$$

Note that in the vicinity of the free surface, i.e., for $p \to 0$, the exponentials tend to 1. The first two terms resemble a level set equation (4.6) using the pressure p as the level set function. This holds exactly, if

$$\frac{\beta}{\alpha} = (S_s - S_r) \leq 1 \qquad (4.9)$$

The third term can be interpreted as a stabilization term with diffusion constant D. Given (4.13) the approximation

$$D = \frac{\gamma}{\beta}\exp\left(\frac{\beta-\alpha}{\gamma}p\right) \approx \frac{\gamma}{\beta}$$

holds in vicinity of the phreatic surface. This quantity provides a guideline for the amount of diffusive stabilization. Note that it tends to zero for large $\beta \gg \gamma$.

4.5 Numerical Experiments

4.5.1 Henry test case

For a 2D example the Henry problem from Section 4.3 is revisited. However, the influx from the left is replaced by an equivalent recharge from the top. As shown in Fig. 4.3, the characteristic current entering from the sea on the right side persists. The intrusion of salt water is less pronounced than in Fig. 4.2a, however, and strongly reduced in particular in the upper part. The recharge also elevates the phreatic surface. The increase is monotonous from right to left, i.e., from the sea to the impermeable watershed, which is a reasonable physical result.

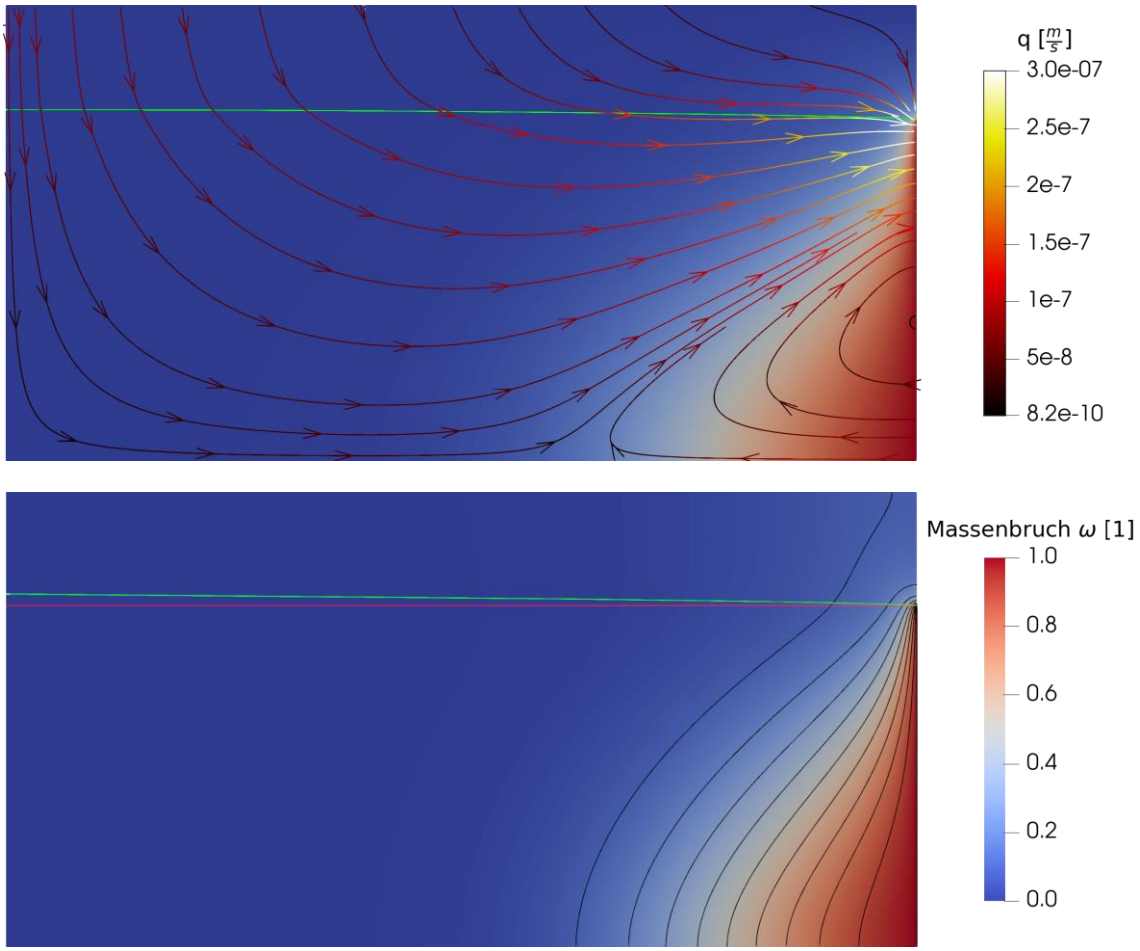

Fig. 4.3 Simulation of the modified Henry problem (w/ recharge) using the phase field formulation for the free surface /CON 22a/. Top: Flow streamlines in steady state (w/ color-coded velocities). Bottom: Due to recharge the free surface moved from its original position (red line) to a slightly elevated level (green line). The black lines represent isolines of the salt mass fraction.

4.5.2 Seawater pumping

The previous experiment may lead to the conclusion, that the free surface tends to stay rather constant. This conjecture is wrong, as can be visualized in a second experiment: To that end, recharge from top is replaced a flux from the left. Moreover, a point sink is placed in the left part of the domain. Extraction rate of the sink and influx form the right are identical. Once the sink attracts salt water, it is deactivated. The results are shown in Fig. 4.4:

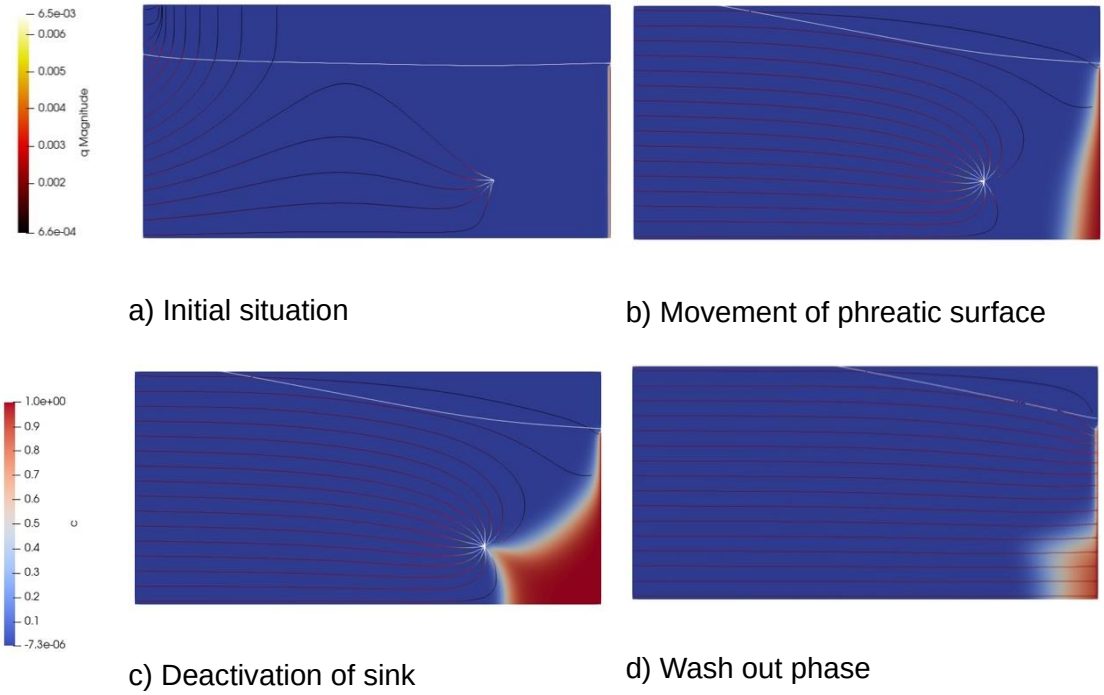

a) Initial situation

b) Movement of phreatic surface

c) Deactivation of sink

d) Wash out phase

Fig. 4.4 Simulation of the Henry problem (w/ pumping) using the phase field formulation for the free surface.

5 Applications and benchmarks

This chapter outlines the application of d³f++ to two groundwater flow models in crystalline rock at regional scales, the Äspö Site Descriptive Model and the former candidate site Kraví Hora in the Czech Republic.

5.1 The Äspö Site Descriptive Model

During the antecedent project GRUSS /SCH 20/ a regional groundwater model including two large deformation zones (DZ) was build up based on information and data provided by SKB (Svensk Kärnbränslehantering AB). It was planned to derive a local model for the Äspö Hard Rock Laboratory (Äspö HRL) from the regional model.

However, the results showed a minor influence of the deformation zones on the flow field. This observation was shared by SKB but there were indications that other regional deformation zones have larger influence. Therefore, it was decided to construct a new regional model as the GRUSS-model seemed to omit significant players in the regional flow.

5.1.1 Model geometries

The code d³f++ provides the possibility to represent fractures filled with a porous medium by low-dimensional structures /SCH 12/. This approach has the advantage, that the triangulation of the fractures is not restricted by their thickness as every fracture is represented by a two-dimensional surface. Furthermore, strong differences between the permeability of the rock matrix and the deformation zones as well as anisotropy can be included easily.

Based on this approach, a new geometry was constructed (cf. Fig. 5.1). The position of the model area and dimensions of the model are described in /SCH 20/. Compared to the model presented in /SCH 20/ the lateral boundaries of the actual model were simplified to reduce the number of elements needed. The complete model containing the hydrogeological units Laxemar/Simpevarp, Äspö, and Regolith, and the network of deformation zones as low-dimensional elements consists of about 183,000 tetrahedral elements. In the following chapters this model is referred to as “DZ model”.

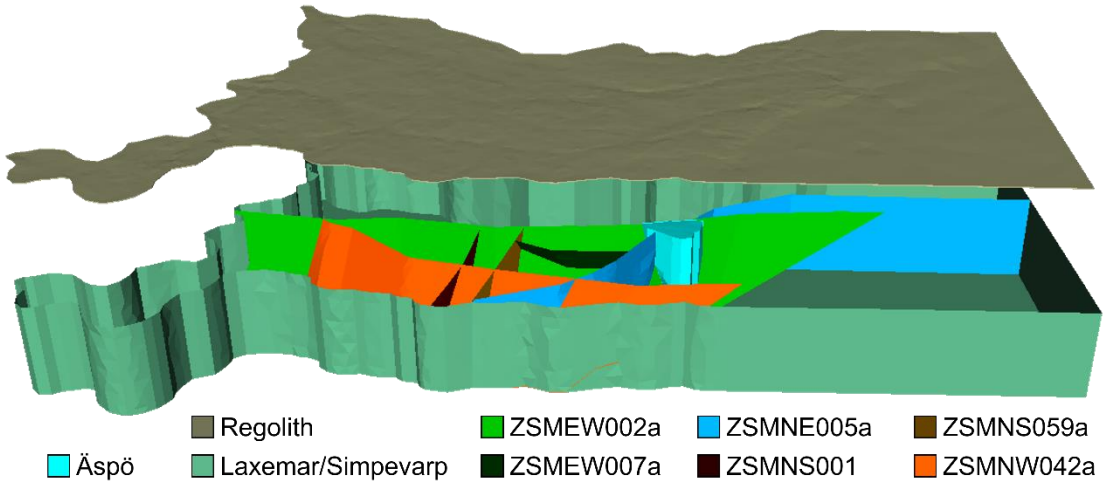

Fig. 5.1 Model geometry with lower-dimensional deformation zones

The hydrogeological unit Laxemar/Simpevarp within the model volume was not displayed to show the position of the deformation zones.

A second model geometry ("FS model") was constructed to perform preliminary simulations with a free surface. The model depth was reduced from 2,100 m to 600 m and an additional layer of 10 m thickness was added above land and islands. This so-called virtual surface layer (VSL) prevented the simulation to abort if the free surface lied temporarily above ground before the equilibrium of the flow field was reached.

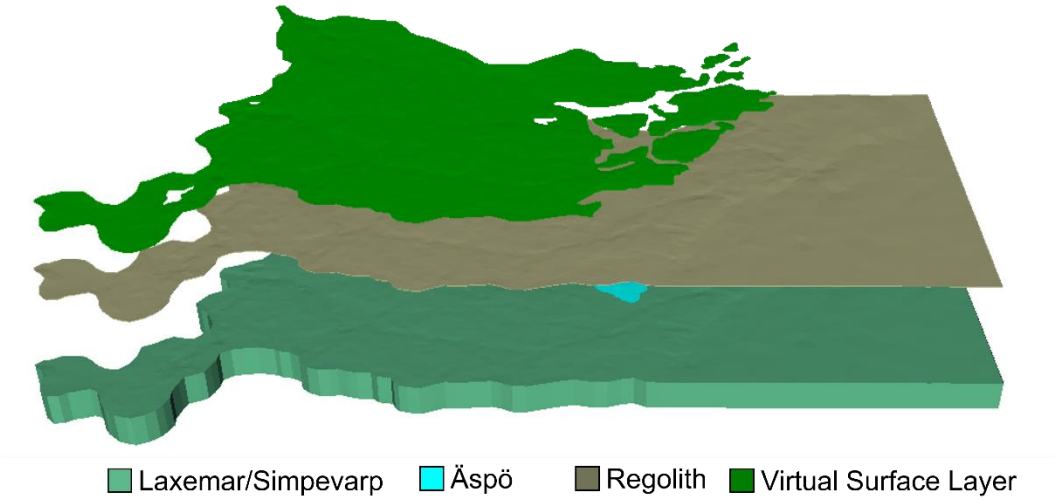

Fig. 5.2 Model geometry for free surface simulations (FS-model)

5.1.2 Parameters, initial and boundary conditions

Depth-dependent permeabilities for the hydrogeological units Laxemar/Simpevarp and Äspö were taken from /SCH 20/. They are assigned to both fracture and free-surface model. The porosity is set to 0.005 for Laxemar/Simpevarp and to 0.3 for Regolith. A uniform permeability of $1.0 \cdot 10^{-13}$ [m^{-2}] is assumed for the regolith. For the FS model, the parameters of Regolith are also assigned to the VSL.

Depth-dependent transmissivity is assumed in DZ-model for the deformation zones based on the following equation /RHE 09/:

$$T = 10^{(a+B \cdot Z)}$$

Here, *a* and *B* are constants while *Z* stands for the width of the deformation zone (values see Tab. 5.1). Additionally, the transmissivity is assumed to be anisotropic for several deformation zones. This applies particularly to ZSMNS001 and ZSMNS059a. These deformation zones are dolerite dykes and have a permeability that is much higher along than across the structure (see Fig. 5.3, note that the lines of these two deformation zones lie almost one above the other). Consequentially, they form hydraulic barriers.

Tab. 5.1 Depth dependent transmissivities

Name	**Width [m]**	**Anisotropy** ($K_{transverse}$: $K_{longitudinal}$)	**a**	**B**
ZSMEW002a	100	1:100	-4.049	0.0019
ZSMEW007a	80		-3.996	0.002158
ZSMNE005a	250		-4.157	0.00255
ZSMNS001	45	1:10,000	-3.680	0.002405
ZSMNS059a	50	1:10,000	-3.652	0.002405
ZSMNW042a	40	1:1,000 (west of ZSMNS059a)	-4.157	0.00255

The transverse permeability of the DZs is in all cases higher than the permeability of the unit Laxemar/Simpevarp and near surface also of the unit Äspö. As the depth-dependence of the latter is less strong than for the permeability of the deformation zones, Äspö has the highest permeability below 700 m b.s.l.. Thus, the deformations should form preferential flow paths within most of the model.

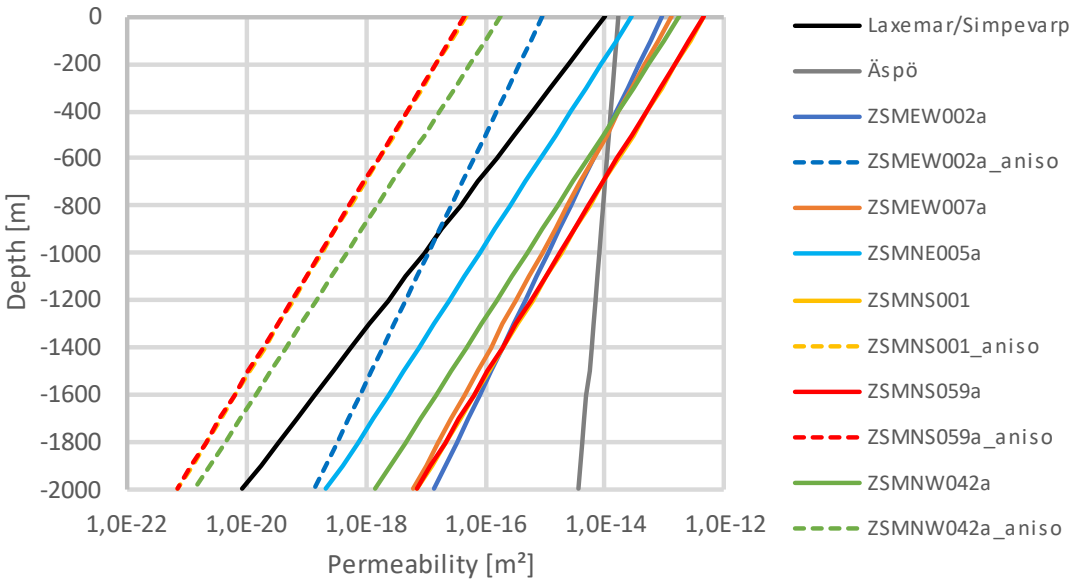

Fig. 5.3 Depth-dependent permeabilities on a logarithmic scale

SKB provided geographic data about rivers and streams but no information about their levels. In the FS model, rivers have the function to drain the area and by this have an impact on the groundwater surface. This effect was achieved by deriving the levels of the rivers and streams from the topography.

The boundary conditions for both models are depicted in Fig. 5.4. The lateral boundaries in the north, south, and west are closed as they form natural watersheds. Hydrostatic pressure was assigned to the eastern boundary as well as to the top boundary in the sea area. For the FS model the free groundwater surface was calculated only below land and islands. It was fixed at sea level at the coast as well as at lake levels below lakes. Groundwater recharge of 180 mm/a was assigned according to /WER 08/.

The initial condition for the free surface was derived from the digital elevation model.

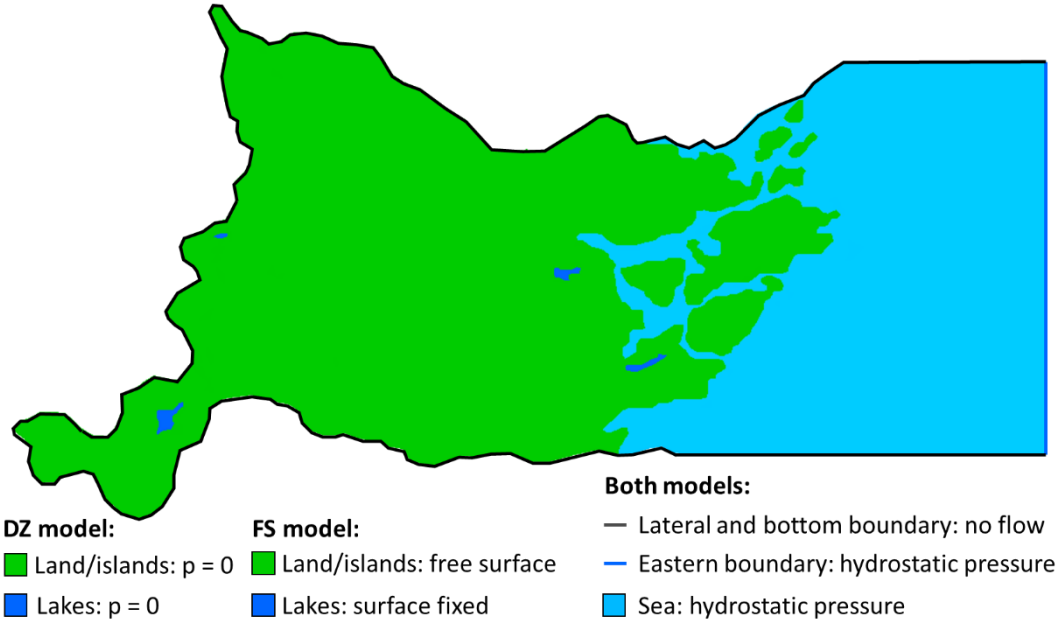

Fig. 5.4 Boundary conditions for both models

5.1.3 Simulation results

For the FS model, the groundwater table lies below the ground surface with few exceptions in topographic depressions, and at the coastline due to technical reasons. The maximum depth of the groundwater table relative to the ground level is about 19 m and, hence, it still lies within the Regolith.

Compared to the topography, the groundwater surface is smoother (cf. Fig. 5.5) but the influence of the topography is visible. The largest differences between the free surface and the topography occur where steep slopes lie in direct neighborhood to a river or stream. There, the groundwater table in the valley lies at river level and – contrary to the steep topography – its surface rises gradually in the direction of the hill. This becomes apparent at the streams in the western part of the model.

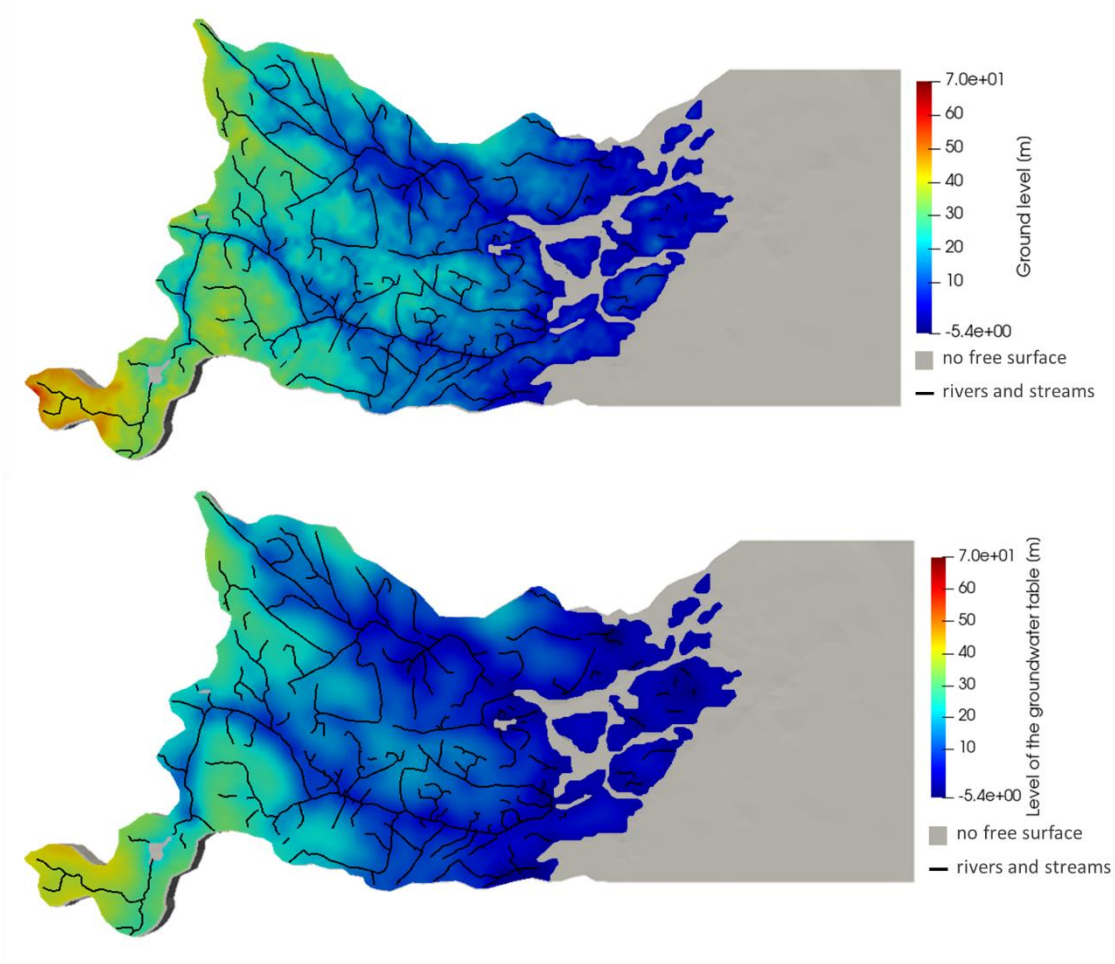

Fig. 5.5 Topography (top) and of the simulated groundwater surface (bottom), both with map of rivers and streams

The simulations resulted in a mostly plausible groundwater surface. The influences of topography and rivers and streams are reflected in its course, and it lies mainly within the unconsolidated rock (Regolith).

For the DZ model, the emphasis of the analyses lay on the effects of the deformation zones on the flow field. Depending on their orientation relative to the main flow directions and in some cases on the anisotropy of the permeability, deformation zones can act as hydraulic barriers or draining structures and might have a major or minor effect on the flow field.

The distribution of the flow velocity in a depth of 500 m (see Fig. 5.6) reveals the position of most deformation zones at first glance by sharp transitions in the flow velocity from one side of the deformation zones to the other. This is most pronounced for the western part of ZSMEW042a while ZSMNS001 can hardly be distinguished at its

northern half. However, the distribution of the flow velocity does not reveal the role the deformation zones play in the regional flow field.

Contrary to that, the stream tracers depicted in Fig. 5.7 provide information about the paths particles would take from their starting points in the vector field of the flow velocity calculated with d³f++. For this purpose, starting points were placed in a depth of 500 m about 150 m to both sides of each deformation zone. The resulting lines show the path a particle would take and the velocity it would have indicated by colour. Due to technical reasons, only flow velocities on the lateral faces of the deformation zones could be considered for the creation of the stream tracers and not the flow within it. Thus, the stream tracers give only information about the flow within the rock matrix and omit the possibility that particles might travel inside the deformation zones. Even if the particle tracers run along the deformation zones this reveals nothing about the flow direction within the deformation zone as the flow on the boundary of a lower-dimensional structure and the flow inside it are strongly decoupled in d³f++.

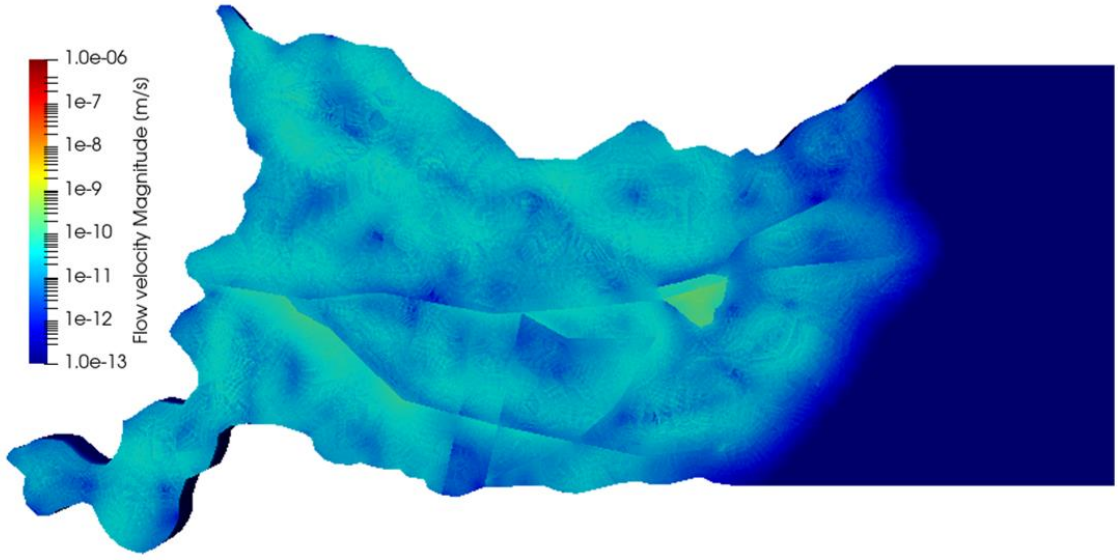

Fig. 5.6 Magnitude of the flow velocity at a depth of 500 m on a logarithmic scale

In the west and southwest of the model area the flow is mainly directed towards the deformation zones whereas the stream tracers diverge from the deformation zones in the east and northeast. This means the deformation zones gather fluid from the west and southwest and release it to the surrounding rock in the east and northeast. All stream tracers are cut where the flow velocity becomes smaller than $1 \cdot 10^{-13}$ m s^{-1}.

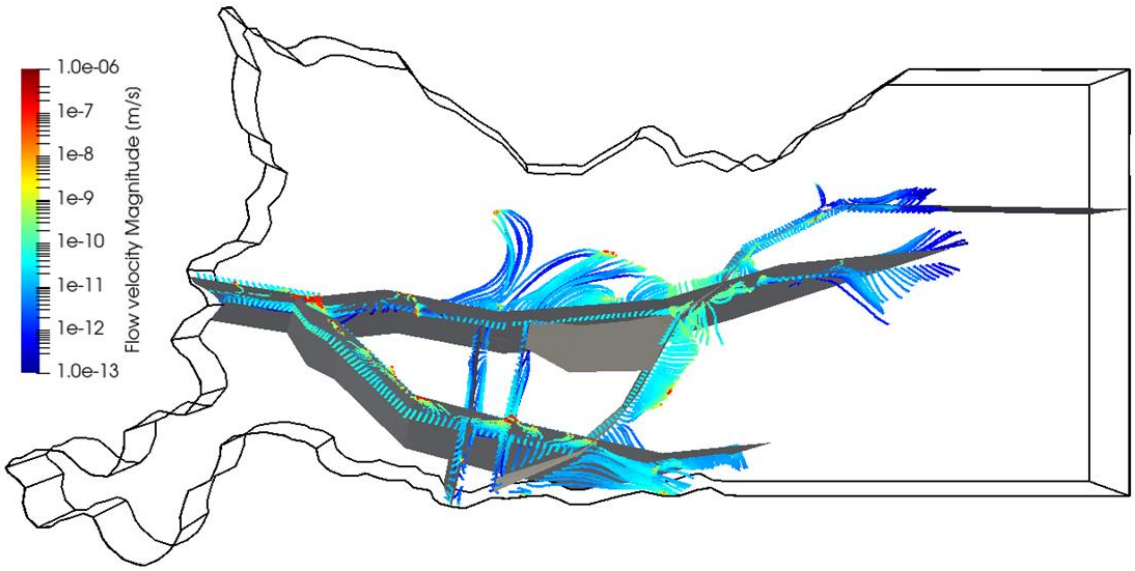

Fig. 5.7 Forward stream tracers placed in a depth of 500 m on both sides of each deformation zone.

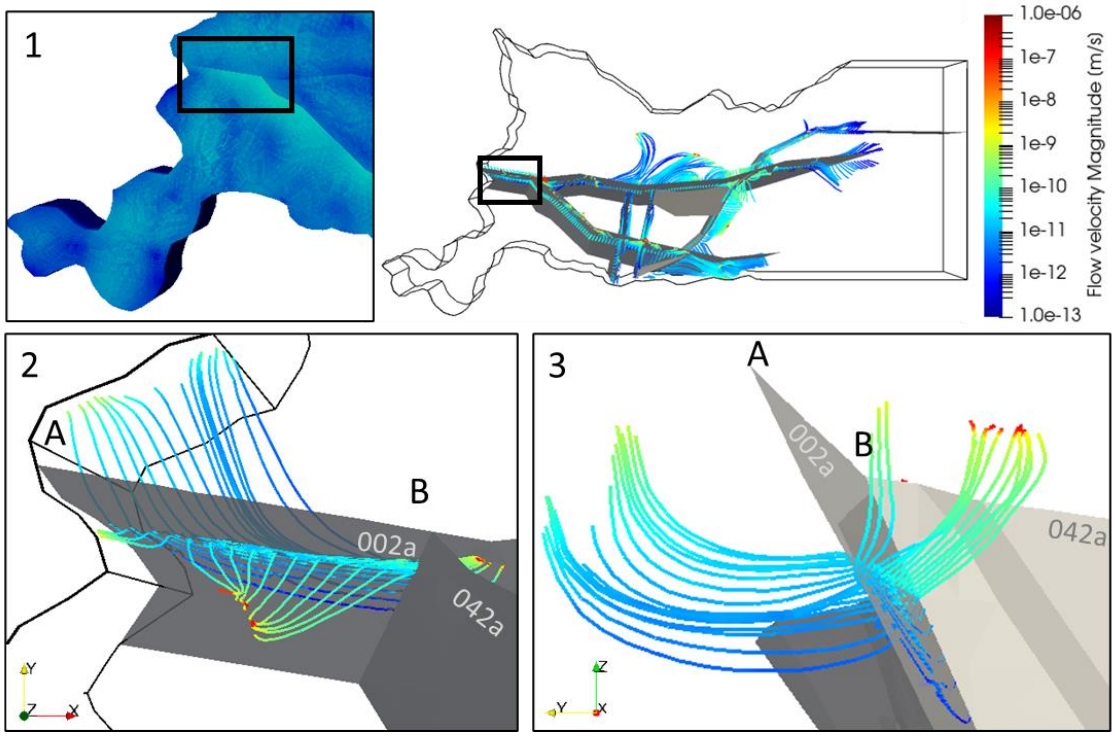

Fig. 5.8 Flow velocity (1) and backward and forward stream tracers starting in a depth of 500 m near the western end of deformation zone ZSMEW002a viewed from above (2) and from west (3)

Four sections of the deformation zones were chosen to analyse the different roles they play within the regional flow field. Depending on their position relative to the main flow

directions and in some cases their anisotropic behaviour, the deformation zones act differently.

At its western end, the flow velocities north and south of ZSMEW002a differ in a depth of 500 m about half an order of magnitude (cf. Fig. 5.8 (1)). Coming from the model surface, fluid flows from both sides toward the deformation zone (cf. Fig. 5.8 (2) and (3)). The fluid from the south covers the shorter distance and reaches the deformation zone at an almost right angle. The stream tracers north of ZSMEW002a are deflected eastwards when approaching the deformation zone. The magnitude of the flow velocity correlates strongly with depth which is plausible because of the depth-dependent permeability of the rock. The stream tracers show that ZSMEW002a gathers fluid from the surrounding rock acting as drainage.

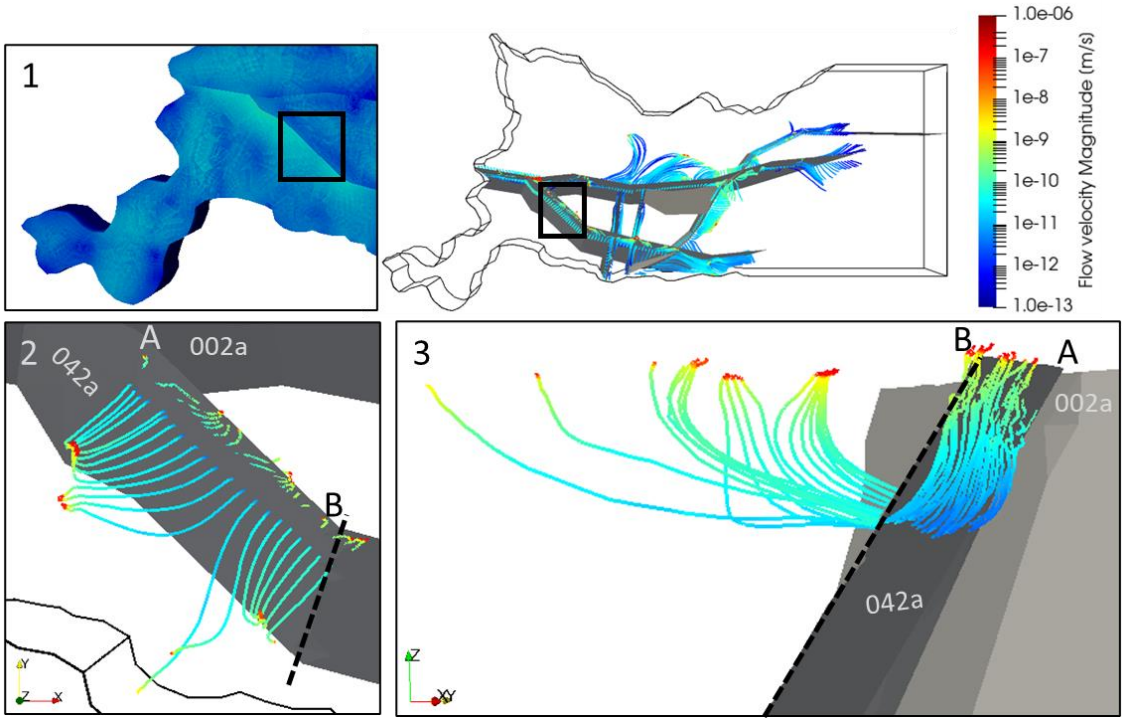

Fig. 5.9 Flow velocity (1) and backward and forward stream tracers starting in a depth of 500 m near deformation zone ZSMNW042a viewed from above (2) and from southeast (3, ZSMNW042a was cut for better visibility of the stream tracers)

A similar effect can be observed at the section of ZSMNW042a in Fig. 5.9. Here, the starting points were placed only on the southwestern side of the deformation zone and the stream tracers were plotted backward and forward. Fluid streams from the southwest to the deformation zone (2), crosses it, approaches the deformation zone again

while flowing upwards (3), and finally reaches the model surface again. As explained before, the flow tracers omit flow within the deformation zone. However, the abrupt decline in the flow velocity of up to one order of magnitude from one side of the deformation zone to the other shows that only a part of the fluid crosses the deformation zone while the rest proceeds within it.

The area between the deformation zones ZSMEW002a, ZSMNW042a, and ZSMNS001 is drained by all three deformation zones (cf. Fig. 5.7) so that only a small proportion is received by the section of ZSMNW042a discussed here (not shown). Thus, this section gathers water mainly from the southwest. The unequal flow from southwest and northeast becomes visible as shadow effect in the flow velocities (cf. Fig. 5.9 (1)).

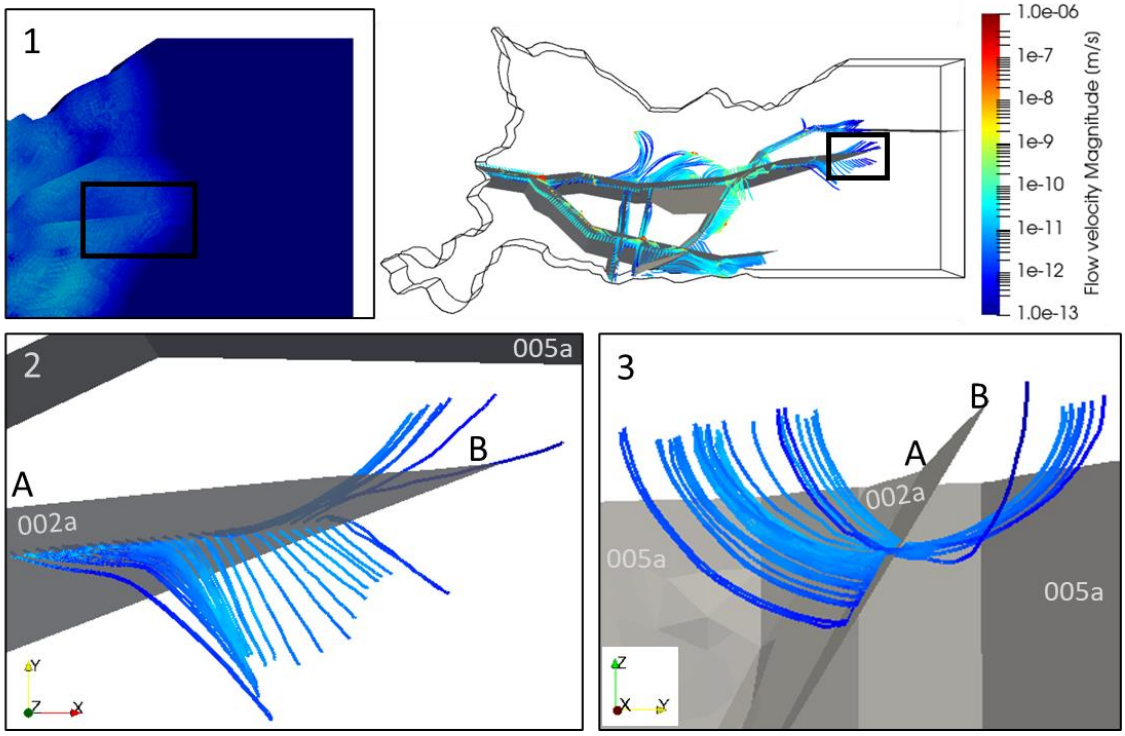

Fig. 5.10 Flow velocity (1) and forward stream tracers starting in a depth of 500 m near the eastern end of deformation zone ZSMEW002a viewed from above (2) and from east (3)

The fluid gathered by the deformation zones in the west and southwest must be released to the surrounding rock from other parts of these structures. The eastern end of ZSMEW002a is such an example (see Fig. 5.10). For clarity reasons only the forward stream tracers were plotted which show that fluid diverges from the deformation zone

while flowing upwards toward the model surface. The flow velocities are some orders of magnitudes smaller than the flow velocities in the draining examples shown before. The reason is that ZSMEW002a forms a dead end within an area with altogether low flow velocities. The flow velocity and direction within the deformation zone (not shown) indicates that the fluid flows mainly up to the regolith rather than leaving into the less permeable rock around the deformation zone. Nevertheless, this section plays its part in the deformation zone network as draining structure.

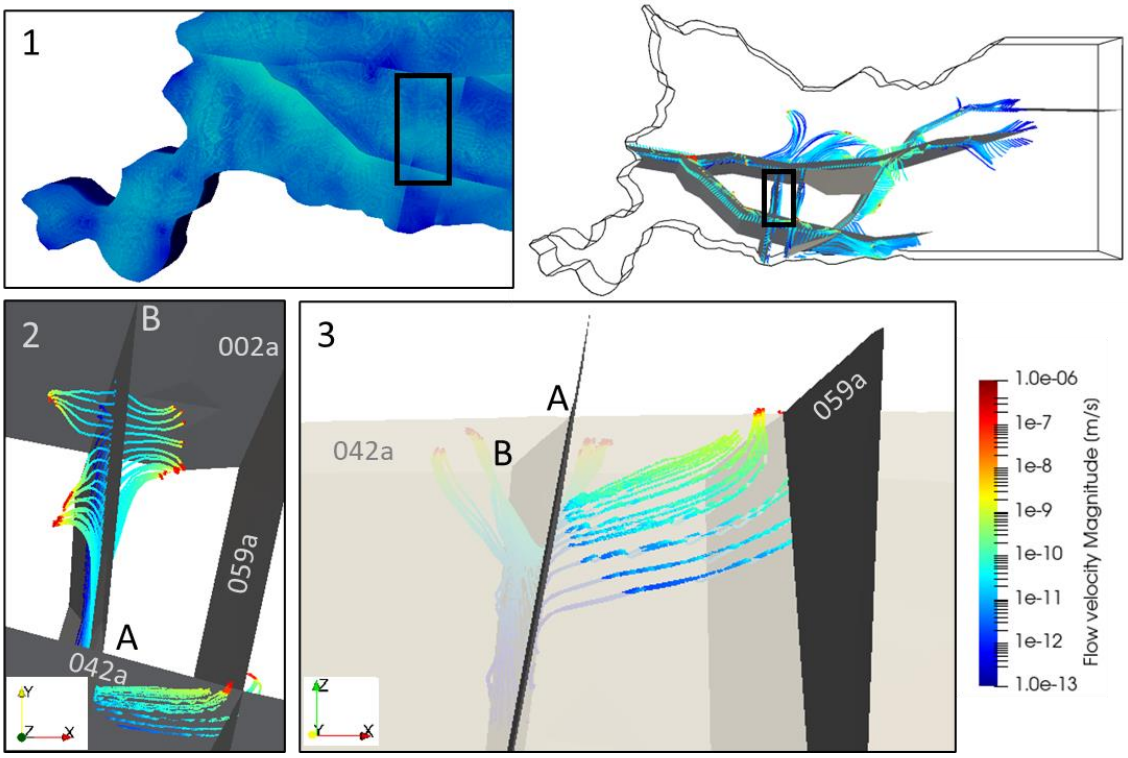

Fig. 5.11 Flow velocity (1) and backward and forward stream tracers starting in a depth of 500 m near deformation zone ZSMEW001 viewed from above (2) and from south (3)

In contrast to the draining effect discussed above, ZSMNS001 plays a different role. Similar to the situation shown in Fig. 5.8 fluid flows from both sides towards the deformation zone (cp. Fig. 5.11). However, the stream tracers diverge while approaching the deformation zone, proceed in a flat angle relative to the deformation zone, and point in the northern part even in the opposite direction than that within the deformation zone (not shown). This shows that the fluid preferentially flows along the deformation zone and not into it. The reason for this is the strong anisotropy of ZSMNS001 which has a longitudinal permeability that is 10^4 times higher than the transversal permeability, and which makes this deformation to a hydraulic barrier.

5.1.4 Summary

The goal of the work with the Äspö site descriptive model was to gain experience with the groundwater modelling in crystalline rock for future work in the site selection process for a long-term repository for highly radioactive waste in Germany. One main characteristic of crystalline is the occurrence of fractures at different scales. In the approach used for this model, the deformation zones that are in fact zones of ductile to brittle deformation of several tens to some hundreds of meters are represented by large lower-dimensional features. This is a simple way to introduce the heterogeneity caused by the deformation zones into the model and it yielded plausible results as shown above. The network of the deformation zone acts mostly as drainage or in the case of the dolorite dykes as hydraulic barrier and thus shows the expected characteristics.

However, an error is introduced by reducing the deformation zones to a lower-dimensional feature as a thickness and therewith a volume is assigned to these features that does not exist physically. The magnitude of this error is not known. It might be negligible when the thickness is considerably smaller than the size of the adjacent elements but should increase with every refinement of the elements. Thus, it would be preferable to use the simple, lower-dimensional description for a coarse grid and switch to a full-dimensional description when the grid is refined.

This idea is intended to be implemented in the following project HYMNE II. The so-called dimension-adaptive extruding should help to bridge between the simple lower-dimensional and the more precise full-dimensional model. Moreover, fracture statistics data published by SKB /RHE 06/, /RHE 08/ will be used to design equivalent porous media (EPM) for the bedrock. In this way, the heterogeneity caused by the small to medium scale fractures shall be introduced into the model.

5.2 Kraví Hora groundwater model

The Czech Radioactive Waste Repository Authority of the Czech Rebublic, SÚRAO, launched in 2014 a large-scale project. The objective was acquiring the knowledge and know-how needed both to form an understanding of the various processes likely to occur within the repository system and to compile conceptual, mathematical and computational models describing the disposal system and predicting its development for safety assessment purposes. As part of this project, nine studies were conducted which were subsequently summarised in the form of safety reports on all candidate deep geological repository sites (Březový potok, Čertovka, Čihadlo, Hrádek, Horka, Janoch, Kraví Hora, Magdaléna and Na Skalním). All candidate sites are situated in a crystalline rock environment. In 2020 the number of potential sites was reduced to four preferred sites for the conducting of geological investigation work, Březový potok (Klatovy Region), Horka (Třebíč Region), Hrádek (Jihlava Region) and Janoch (near NPP Temelin site). The schedule envisages that the Government will select a final and a reserve site in 2025. The actual construction of the repository will commence in 2050 with the start of operation of the facility expected in 2065 at the earliest.

In 2015, SURAO started a project in where regional geological and hydrogeological models were developed for the nine candidate sites mentioned above. Based on this a 3d flow- and transport modelling should be performed to describe the groundwater flow in the geosphere and to identify the main transport pathways. The Czech Geological Survey, the PROGEO consulting engineers, the Libereč Technical University, and ÚJV Řež are taking part in this project. SURAO provided successively site characterizing data to the project partners. The working groups participating build up groundwater flow and transport models based on different numerical codes, MODFLOW /HUG 17/, FEFLOW /WAS 10/ and FLOW123 (ÚJV in-house code, /JAN 19/), and they are exchanging their results at regular meetings. In the course of the German-Czech cooperation in 2015 the GRS suggestion of setting-up a groundwater model for one of these sites also with d³f++ was appreciated, and the Čihadlo site, about 100 km south-east of Prague, was selected and modelled in the project GRUSS /SCH-20/. In the frames of the HYMNE-project, the hydrogeological data of the Kraví Hora site in the northwest of Brno (see Fig. 5.12) were provided by SÚRAO.

Fig. 5.12 Situation of the Kraví Hora site in the map of the Czech Republic (source: SÚRAO)

As well as Čihadlo, also Kraví Hora is situated in crystalline rock, but there is much more geological, hydrogeological and fault lineament information available because of the existence of two former uranium mines in the immediate proximity of the proposed DGR, the Rožná mine in NW and the Olší mine in SE inside the model area, see Fig. 5.13. The local rock units belong to the Moldanubicum and Crystallinium. The naturally fractured rock massif with fault zones with a thickness up to 100 m is covered by a sedimental layer (weathering zone). The existing fault system is in general trending N-NW to S-SE or NW–SE. Permeabilities are assumed to decrease with depth. The most important parts of the mine workings are also influencing the flow regime in the form of higher permeability and porosity parameters in the hydrogeological model.

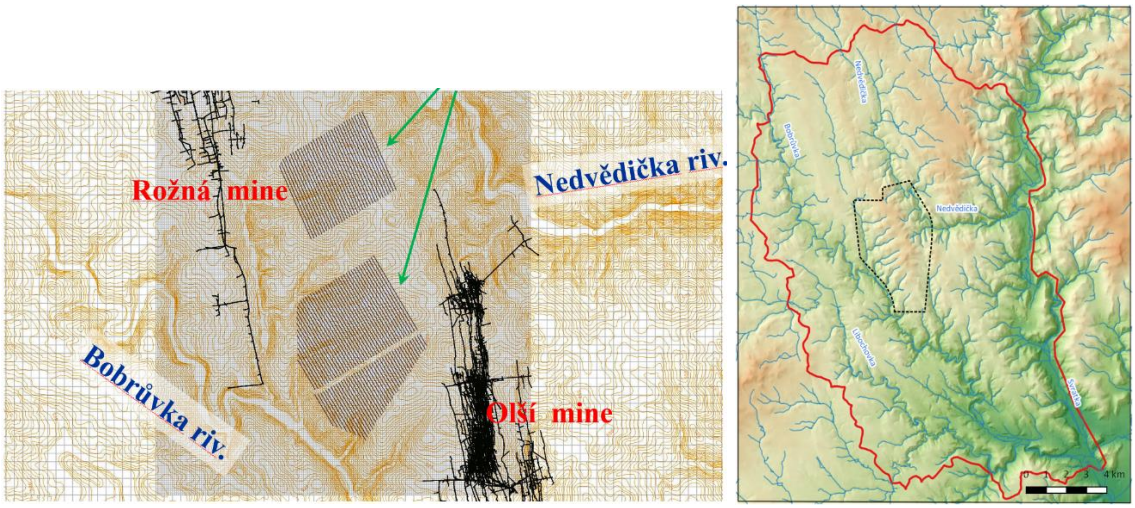

Fig. 5.13 Situation of the candidate site between the two former uranium mines (left) and area of the groundwater model (right), source: PROGEO

The hydrogeological data was provided in the form of MODFLOW input data. These were the model geometry, pointwise permeability and porosity values for an equivalent porous media (EPM) model with 1.76 million grid cells, groundwater heads, recharge data and the river network.

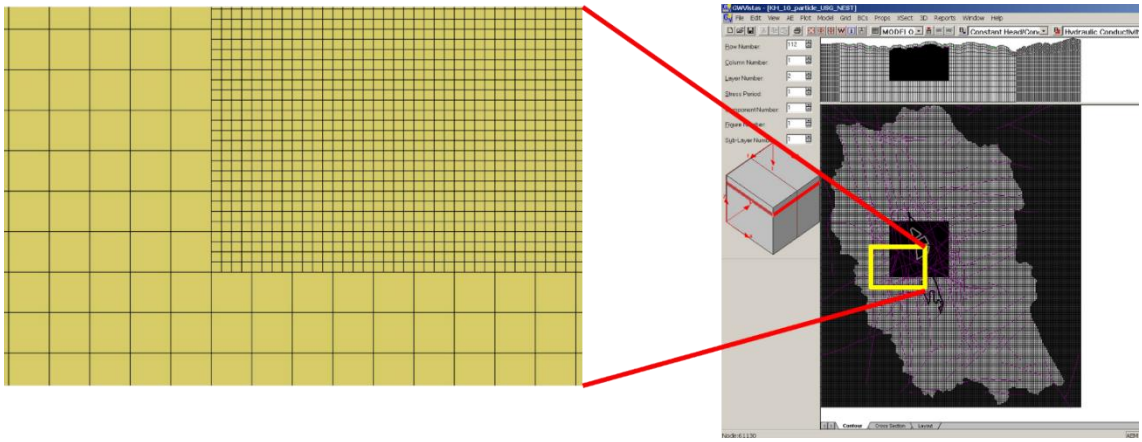

Fig. 5.14 Model area Kraví Hora with fault zones (right) and sketch of the MODFLOW grid (source: PROGEO, J. Uhlik)

The received model data consisted of two parts, a regional model covering an area of about 253.5 km² with a depth of 1.5 km, and a detailed model with an extension of 4.475 km x 5.575 km. The regional model is composed of 13 layers with a grid resolution of 100 m, the detailed model consists of 40 layers with a resolution of 25 m, see Fig. 5.14Model area Kraví Hora with fault zones (right) and sketch of the MODFLOW grid (source: PROGEO, J. Uhlik). To implement the model in d³f++, the data of the two

models had to be separated, transformed and composed again to generate a prism grid, see Fig. 5.15.

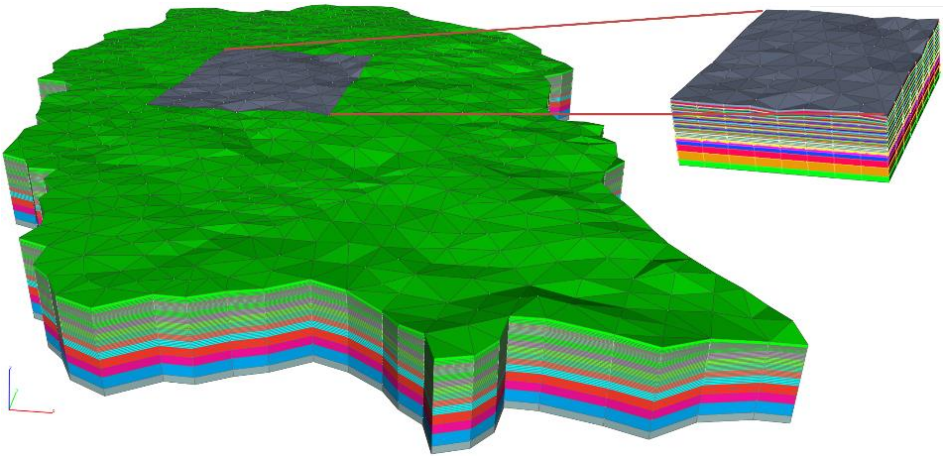

Fig. 5.15 Regional model and embedded detail model in d³f++ (coarse grid)

The isotropic permeability and the porosity data were transformed into 2d raster data and for each of the 53 layers imported into the model, see Fig. 5.16.

The lateral model boundaries are following watersheds and therefore closed for groundwater flow. The bottom of the model domain is also defined as a closed boundary. Groundwater recharge rates vary from 69 to 83 mm/year and are constant in time, see Fig. 5.17. The initial groundwater table is assumed to be close to ground surface.

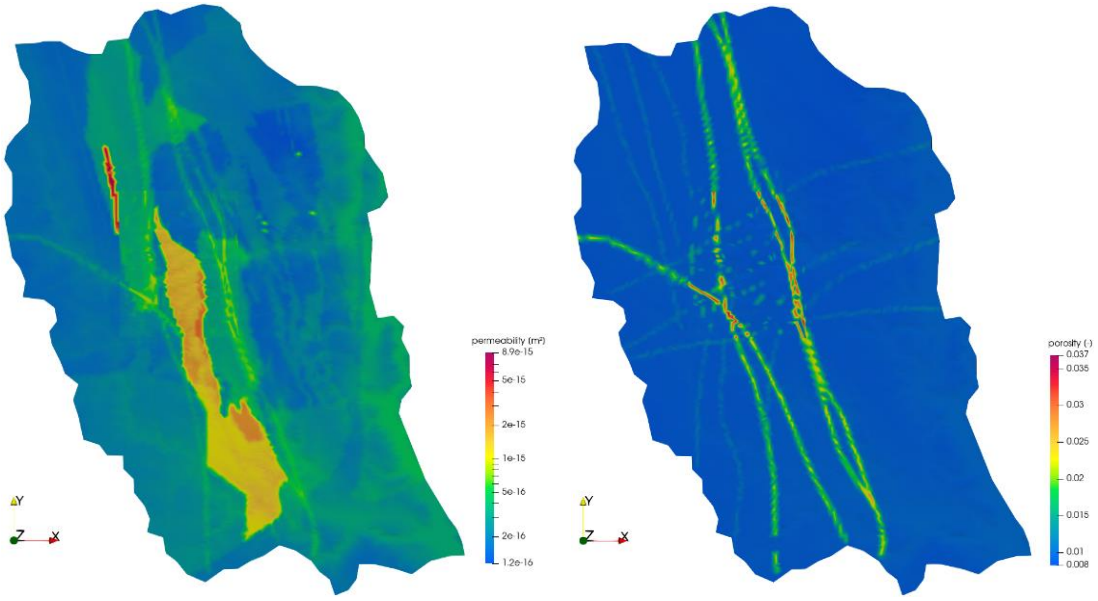

Fig. 5.16 ASCII Raster data for permeability (left) and porosity (right) data exemplarily for layer 4 (regional model) and 41 (detailed part)

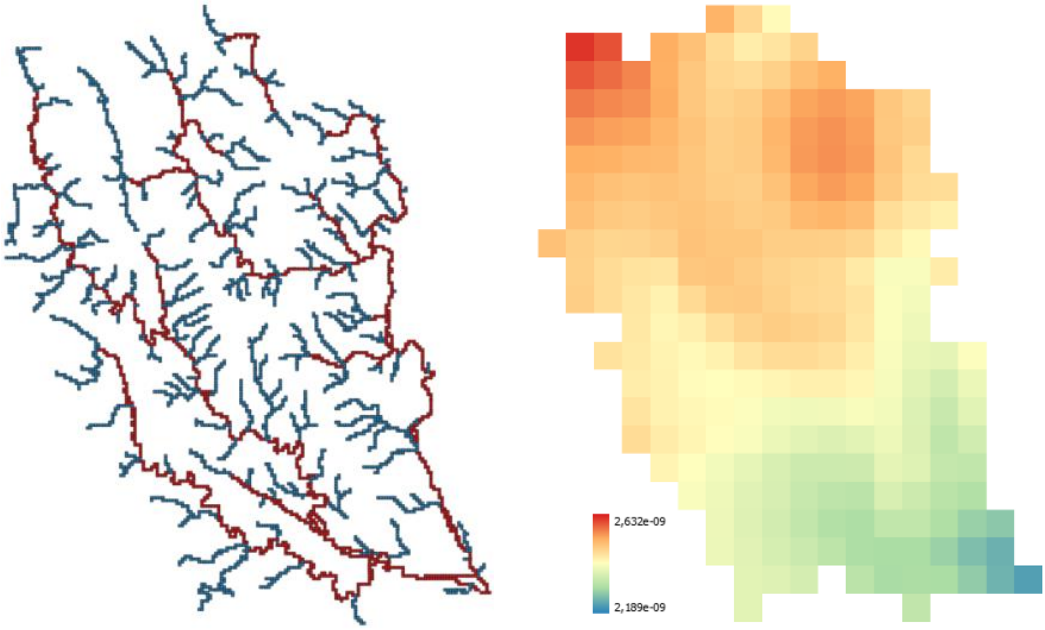

Fig. 5.17 River network (left) and groundwater recharge rates (right) as input for the Kraví Hora model

The d³f++ simulations were performed on multigrid-level 2 with 4.87 millions of elements on 24 computing cores. Fig. 5.18 and Fig. 5.19 illustrate the process of model calibration. A model time of more than 60 years was necessary to reach a steady-state in river draining as well as the fluid volume below the free groundwater surface. The model reproduces very well the groundwater head measures and also the MODFLOW results of PROGEO. The Nash Sutcliffe efficiency coefficient reaches 0.981.

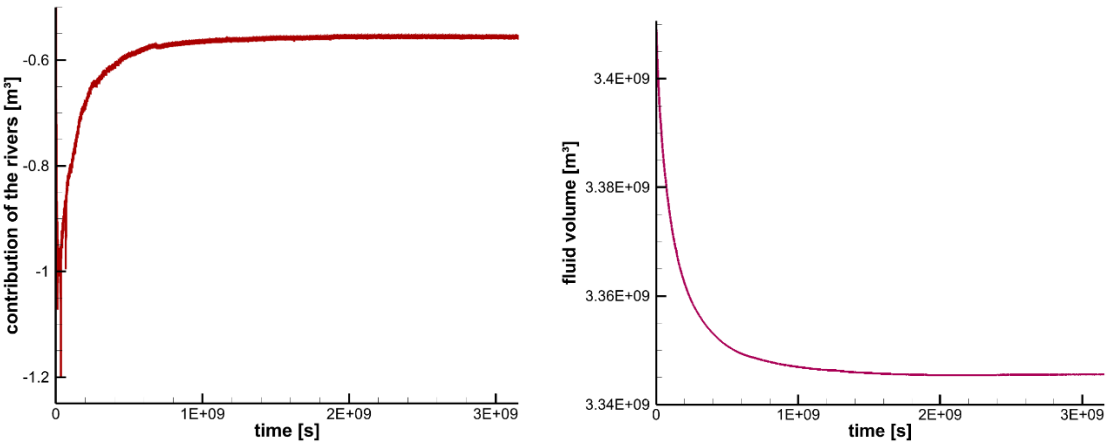

Fig. 5.18 Model calibration: development of river draining (left) and fluid volume below the computed groundwater surface (right) with time

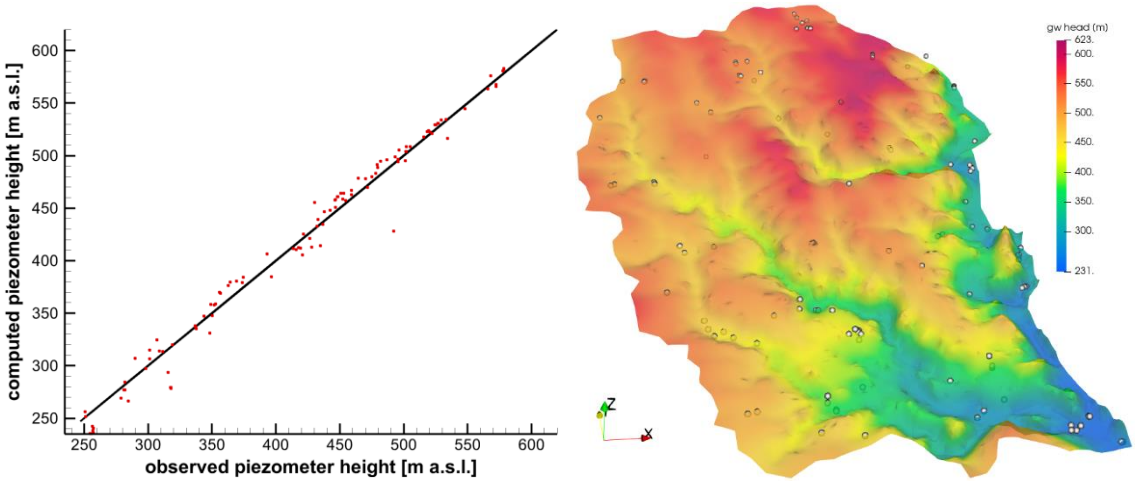

Fig. 5.19 Model calibration: comparison of observed and computed hydraulic heads (2x scaled in vertical direction)

Fig. 5.20 shows the simulated groundwater level at a model time of 100 years. The river network is added for orientation. The resulting groundwater heads are mainly influenced by morphology and river draining.

Concluding can be said that d³f++ is able to simulate large-scale EPM-models with free groundwater table. For a better calibration it would be desirable to enable comparisons also between the draining amounts of the main river catchment areas. The set-up of discrete fracture network (DFN) models would be preferable to benefit of a finer grid resolution, but therefore an explicit knowledge of the fault zones and their statistic properties is needed.

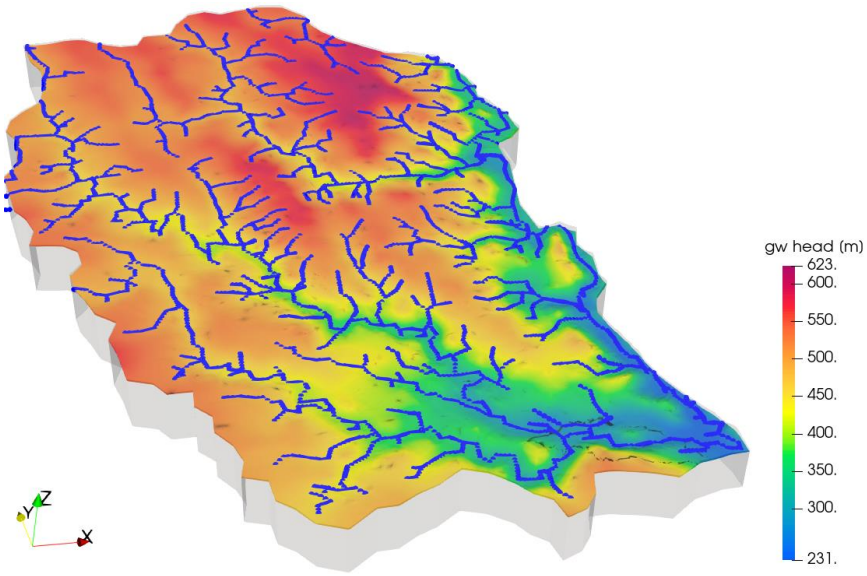

Fig. 5.20 Simulated groundwater level Kraví Hora with river network

6 Summary

The works described in this report were funded by the German Federal Ministry of Economics and Technology (BMWi) with the objective to improve and extent the tools for groundwater flow and transport modelling as an important element of long-term safety assessment for radioactive waste repositories. The growing and varying demands on groundwater flow and transport modelling, such as growing extension and complexity of the models and the mapping of new physical processes in the equations, evoke constantly rising requirements for code enhancement and improvement.

All potential sites for a nuclear waste repository in Germany have been under permafrost conditions during the last 100.000 years. It has to be assumed that this will also happen in the future during the lifetime of any geological repository. Therefore, the topic of modelling groundwater flow under permafrost conditions is addressed here. The motivation and physical as well as mathematical models are discussed in this report, and balance equations as well as formulations for the state variables are derived. The permafrost model was implemented in d³f++. Two benchmarks of the INTERFROST program /GRE 18/ were successfully simulated.

d³f++ was originally developed for the modelling of confined aquifers. Subsequently, level-set methods were adapted and implemented to enable the code for the modelling of a free groundwater surface. In the last years free surfaces are gaining more and more importance, especially in groundwater modelling at a regional scale as in the case of Kraví Hora, the Äspö SDM model, and also in saltwater intrusion models in coastal zones. Therefore, a lot of work was done for a substantially stabilization of the levelset method, among other things by introducing an artificial stabilizing diffusion term into the level-set equation. This enables the successful application of the code to complex models of thousands of square kilometers, especially under density-driven flow conditions.

In the case of crystalline rock models, e. g. the Äspö-SDM model, it cannot be ruled out that the groundwater surface may sink into the fractured rock. But it has proved almost impossible to combine the level-set method with lower dimensional discrete fracture models. Therefore, a second free surface model, based on Richard’s equation combined with density-driven flow, was developed and implemented in d³f++.

Drainage by the receiving waters plays a crucial role for the groundwater balance. River draining was already implemented in d³f++ during the H-DuR project /SCH 16/. But the water levels of the rivers are generally not known or only known at only few gauging stations. In some cases, the runoff via the receiving waters can be quantified by measures or by using appropriate surface runoff models. This variable, on the other hand, could not be used for d³f++ to date. Therefore, a river flow model, based on the Saint Venant equation, has been developed, implemented and successfully tested.

An intelligent, efficient model calibration plays an essential role, especially in the reliability of forecasts. The implementation of a new inverse modelling tool is presented in this report. This tool was not only successfully tested by a 2d test case but also applied to a 3d field-scale model.

The growing extension and complexity of the models require steadily further speed-up and robustness of the solvers. At the other hand, recent scientific advances in the field of numerics have to be adopted, and code adaptions are crucial for profiting of new hardware developments. Various advancements of the solvers were performed.

A demonstration of the capability and efficiency of d³f++ in regional-scale modelling is important for a broad acceptance and application of the code. In the scope of this work d³f++ was applied to two 3d groundwater flow models at regional scale in crystalline rock. The first of them is the Äspö Site Descriptive Model (SDM) over an area of about 250 km², situated in fractured granite, covered by a thin sedimental layer. A 3d model with deformation zones and free groundwater surface was successfully set-up. As the second application the Kraví Hora candidate site in the Czech Republic was modeled, covering an area of about 250 km² in granite with a huge system of fault zones. Following the work of the PROGEO colleagues, an equivalent porous media (EPM) approach was chosen. The result was a plausible model, and groundwater heads are corresponding very well with the results of PROGEO.

In summary, the range of applications of d³f++ has been enlarged to permafrost phenomena, and the applicability to density-driven flow models with free groundwater surface and river discharge at a regional scale was significantly enhanced. Efficiency, robustness and stability of the numerical solvers could be substantially improved. Finally, the application of d³f++ to three regional-scale models from the field of radioactive waste disposal in crystalline rock contributes to the qualification of the code and to a growing confidence in groundwater modelling as part of long-term safety assessment.

The increasing capability of the code opens up doors to an increasing variety of applications on all scales of research for radioactive waste repositories. This work contributes substantially to the ongoing development of tools for the assessment of long-term safety of geological repositories for radioactive waste.

References

/BEA 10/ Bear, J., Cheng, A. H.-D.: Modeling Groundwater Flow and Contaminant Transport. Springer, Netherlands. doi:10.1007/ 978-1-4020-6682-5, 2010.

/BEY 95/ Downwind numbering: robust multigrid for convection-diffusion problems. Appl. Numer. Math. 23, pp. 177-192, 1997.

/BGR 12/ BGR: Karte der untersuchungswürdigen Wirtsgesteinsformationen – Ergebnisse der regionalen BGR-Studien. Webpages of BGR, 2012. https://www.bgr.bund.de/DE/Themen/Endlagerung/Downloads/Charakterisierung_Wirtsgesteine_geotech_Barrieren/4_Wirtsgesteinsuebergreifend/Karte_Wirtsgesteinsformationen_Dtl.html (as of 15.06.2021)

/BGE 20/ Bundesanstalt für Endlagerung mbH (BGE): Zwischenbericht Teilgebiete gemäß §13 StandAG. Geschäftszeichen: SG01101/16-1/2-2019#3 – Objekt-ID: 755925 – Revision: 000, BGE, Peine, 2020.

/CHE 08/ Chesworth, Ward, Marta Camps Arbestain, Felipe Macías, Otto Spaargaren, Otto Spaargaren, Y. Mualem, und H. J. Morel-Seytoux. „Capillary Pressure“. In *Encyclopedia of Soil Science*, herausgegeben von Ward Chesworth, 81–91. Encyclopedia of Earth Sciences Series. Dordrecht: Springer Netherlands, https://doi.org/10.1007/978-1-4020-3995-9_87, 2008.

/CON 22a/ Niklas Conen: Simuation dichtegetriebener Strömungen in ungesättigten porösen Medien, B.Sc. thesis, GU Frankfurt, 2022.

/CON 22b/ Niklas Conen: Hydrochemische Modellierung des Stickstoffeintrags durch landwirtschaftliche Nutzflächen in Regionen mit Trinkwasserbrunnen, B.Sc. thesis, GU Frankfurt, 2022.

/DEL 98/ Delisle, G.: Numerical simulation of permafrost growth and decay. Journal of Quarternary Science 13 (4), 325-333, 1998.

/FEI 99/ Fein, E.; Schneider, A. (eds.): d³f – Ein Programmpaket zur Modellierung von Dichteströmungen. Abschlussbericht. Gesellschaft für Anlagen- und Reaktorsicherheit (GRS) gGmbH, GRS-139, Braunschweig 1999.

/FEI 04/ Fein, E. (ed.): Software Package r³t. Model for Transport and Retention in Porous Media. Gesellschaft für Anlagen- und Reaktorsicherheit (GRS) gGmbH, GRS-192, Braunschweig 2004.

/FRO 12/ Frolkovic, P.: Application of level set method for groundwater flow with moving boundary. Advances in Water Resources 47, 56-66, DOI: 10.1016/j.advwatres.2012.06.013, 2012.

/GÄR 87/ Gärtner, S.: Zur diskreten Approximation kontinuumsmechanischer Bilanz-gleichungen. Bericht Nr. 24/1987, Institut für Strömungsmechanik und Elek-tronisches Rechnen im Bauwesen, Universität Hannover, 1987.

/GRE 18/ Grenier, C., Anbergen, H., Bense, V., Chanzy, Q., Coon, E., Collier, N., Costard, F., Ferry, M., Frampton, A., Frederick, J., Gonçalvès, J., Holmén, J., Jost, A., Kokh, S., Kurylyk, B., McKenzie, J., Molson, J., Mouche, E., Orgogozo, L., Pannetier, R., Rivière, A., Roux, N., Rühaak, W., Scheidegger, J., Selroos, J.-O., Therrien, R., Vidstrand, P., Voss, C.: Groundwater flow and heat transport for systems undergoing freeze-thaw: Intercomparison of numerical simulators for 2D test cases. Advances in Water Resources 114 (2018) 196–218, Elsevier, 2018.

/GRI 10/ Grillo, A., Logashenko, D., Stichel, S., Wittum, G.: Simulation of Density-Driven Flow in Fractured Porous Media. Advances in Water Resources 33 (12), 1494-1507, 2010, DOI: 10.1016/j.advwatres.2010.08.004

/GRI 12/ Grillo, A., Lampe, M., Logashenko, D., Stichel, S., Wittum, G.: Simulation of salinity- and thermohaline-driven flow in fractured porous media. Journal of Porous Media 15 (5), 439-458, 2012, DOI: 10.1615/JPorMedia.v15.i5.40

/GRI 13/ Grillo, A., Logashenko, D., Stichel, S., Wittum, G.: Forchheimer's correction in modelling flow and transport in fractured porous media. Computing and Visualization in Science 15(4), 169-190, 2012, DOI: 10.1007/s00791-013-0208-1

/HIL 22/ Julian Hilbert: Modellierung und Simulation eines Flussnetzwerkes über einem porösen Medium, M.Sc. thesis, 2022.

/HUG 17/ Hughes, J.D., Langevin, C.D., and Banta, E.R., 2017, Documentation for the MODFLOW 6 framework: U.S. Geological Survey Techniques and Methods, book 6, chap. A57, 40 p., https://doi.org/10.3133/tm6A57.

/JAN 19/ Jankovský, F., Zuna, M., Havlová, V., Fisher, C., Kulenkampff, J., Kotowski, J., Polak, M., Hokr M., Cernik, M.: Contaminant migration in fractured rocks: insights from tracer tests in core scale Geophysical Research Abstracts, Vol. 21, EGU2019-10839, 2019.

/JOB 16/ Jobmann, M. (ed.): Site-specific evaluation of safety issues for high-level waste disposal in crystalline rocks. Final Report. DBE TECHNOLOGY GmbH, TEC-28-2015-AB, Peine, 2016.

/JOH 02/ Johannsen, K., Kinzelbach, W., Oswald, S., Wittum, G.: The saltpool benchmark problem - numerical simulation of saltwater upconing in a porous medium. *ADVANCES IN WATER RESOURCES* 25 (2002), 335–348

/JOH 16/ Johansson, E.: The influence of climate and permafrost on catchment hydrology. Thesis, Department of Physical Geography, Stockholm University, 2016.

/KEL 98/ Keller, S.: Permafrost in der Weichsel-Kaltzeit und Langzeitprognose der hydrogeologischen Entwicklung der Umgebung von Gorleben / NW-Deutschland. Z. Angew. Geol. 48, 111-119, 1998.

/KRE 15/ Kreye, P.: Mesoskalige Bodenwasserhaushaltsmodellierung mit Nutzung von Grundwassermessungen und satellitenbasierten Bodenfeuchtedaten. Dissertation an der TU Braunschweig, Braunschweig, 2015.

/KRÖ 08/ Kröhn, K.-P.: Values required for the simulation of CO_2-storage in deep aquifers. FKZ 03 G 0622 B (BMWI), Gesellschaft für Anlagen- und Reaktorsicherheit (GRS) gGmbH, GRS-236, GRS Braunschweig, 2008.

/KRÖ 10/ Kröhn, K.-P.: State Variables for Modelling Thermohaline Flow in Rocks.FKZ 02 E 10336 (BMWi), Gesellschaft für Anlagen- und Reaktorsicherheit (GRS) gGmbH, GRS-268, Braunschweig, 2010.

/KRÖ 22/ Kröhn, K.-P.: Basics for Groundwater flow under permafrost conditions in the context of radioactive storage. FKZ 02 E1 1809 A-B (BMWi), Gesellschaft für Anlagen- und Reaktorsicherheit (GRS) gGmbH, GRS-707, Braunschweig, 2022.

/MÖL 22/ Patrik Möller: Modellierung und Simulation thermohydraulischer Strömungen, B.Sc. thesis, GU Frankfurt, 2022.

/MCK 13/ McKenzie, J.M., Voss, C.I. Permafrost thaw in a nested groundwater-flow system. Hydrogeol J 21, 299–316. doi: 10.1007/s10040-012-0942-3, 2013.

/MUA 76/ Mualem Y. A new model for predicting the hydraulic conductivity of unsaturated porous media. Water Resources Research.12(3):513–22, 1976.

/NAE 19/ Nägel, A., Logashenko, D., Schroder, J. B., Yang, U., M.: Aspects of Solvers for Large-Scale Coupled Problems in Porous Media, Transport in Porous Media volume 130, 363–390, 2019, DOI: 10.1007/s11242-019-01323-w, 2019.

/NOS 12/ Noseck, U., Becker, D., Brasser, T., Flügge, J., Fahrenholz, Ch., Herbert, H., Ionescu, A., Kröhn, K.-P., Kull, H., Meleshyn, A., Mönig, J., Röhlig, K., Rübel, A., Rothfuchs, T.; Wolf, J.: Scientific basis for a safety case of deep geological repositories. Final report, FKZ-02 E 10548 (BMWi), Gesellschaft für Anlagen- und Reaktorsicherheit (GRS) gGmbH, GRS-298, 2012.

/PAR 18/ Parazoo, N.C., Koven, C.D., Lawrence, D.M., Romanovsky, V., and Miller, C.E.: Detecting the permafrost carbon feedback: talik formation and increased cold-season respiration as precursors to sink-to-source transitions. The Cryosphere, 12, 123–144, 2018, https://doi.org/10.5194/tc-12-123-2018.

/PUL 90/ Pullan AJ. The quasilinear approximation for unsaturated porous media flow. Water Resources Research 26(6):1219–34, 1990.

/REI 12/ Reiter. S., Logashenko, D., Grillo, A., Wittum, G.: Preparation of grids for simulations of groundwater flow in fractured porous media. Computing and Visualization in Science 15 (4), 209-225, 2012, DOI: 10.1007/s00791-013-0210-7

/REI 20/ Reiter. S., Logashenko, D., Vogel, A., Wittum, G.: Mesh generation for thin layered domains and its application to parallel multigrid simulation of groundwater flow. Computing and Visualization in Science 23, 2, 2020, DOI: 10.1007/s00791-020-00322-5

/REN 96/ Rentz-Reichert, H., Wittum, G.: A Comparison of Smoothers and Numbering Strategies for Laminar Flow Around a Cylinder. In: Hirschel, E.H. (eds) Flow Simulation with High-Performance Computers II. Notes on Numerical Fluid Mechanics (NNFM), vol 48. Vieweg+Teubner Verlag. https://doi.org/10.1007/978-3-322-89849-4_10. 1996.

/REN 03/ Renssen, H. and Vandenberghe, J.: Investigation of the relationship between permafrost distribution in NW Europe and extensive winter sea-ice cover in the North Atlantic Ocean during the cold phases of the Last Glaciation. Quaternary Science Reviews 22, 209-223, 2003.

/RHE 06/ Rhén, I., Forsmark, T., Forssman, I., Zetterlund, M.: Evaluation of hydrogeological properties for Hydraulic Conductor Domains (HCD) and Hydraulic Rock Domains (HRD), Laxemar subarea – version 1.2, SKB Report R-06-22, Svensk Kärnbränslehantering AB, Stockholm, 2006.

/RHE 08/ Rhén, I., Forsmark, T., Hartley, L., Jackson, P., Roberts., D., Swan, D., Gylling, B.: Hydrogeological conceptualization and parameterization, Site descriptive modelling SDM-Site Laxemar, SKB Report R-08-78, Svensk Kärnbränslehantering AB, Stockholm, 2008.

/RHE 09/ Rhén, I., Forsmark, T., Hartley, L., Joyce, S., Roberts, D., Gylling, B., Marsic, N.: Bedrock hydrogeology: Model testing and synthesis – Site descriptive modelling, SDM-Site Laxemar, SKB Report R-08-91, Svensk Kärnbränslehantering AB, Stockholm, 2009.

/RIC 31/ Richards LA. CAPILLARY CONDUCTION OF LIQUIDS THROUGH POROUS MEDIUMS. J Appl Phys.;1(5):318–33, Nov. 1931.

/SCH 12/ Schneider, A. (ed.): Enhancement of d³f und r³t (E-DuR). FKZ 02 E 10336 (BMWK), final report, Gesellschaft für Anlagen- und Reaktorsicherheit (GRS) gGmbH, GRS-292, Braunschweig, 2012.

/SCH 13/ Schneider, A. (Hrsg.), Representation of inhomogeneities in the flow and transport codes d³f and r³t, Gesellschaft für Anlagen- und Reaktorsicherheit (GRS) gGmbH GRS 311, Braunschweig, 2013.

/SCH 16/ Schneider, A. (ed.): Modeling of Data Uncertainties on Hybrid Computers (H-DuR). FKZ 02 E 11062A (BMWi), final report, Gesellschaft für Anlagen- und Reaktorsicherheit (GRS) gGmbH, GRS-392, Braunschweig, 2016.

/SCH 17/ Schneider, A., Gehrke, A., Kröhn, K.-P., Zhao, H.: Qualification of the Code d³f++. FKZ 02E11213 (BMWi), final report, Gesellschaft für Anlagen- und Reaktorsicherheit (GRS) gGmbH, GRS-448, Braunschweig, 2017.

/SCH 18/ Schneider, A. et al.: Modeling saltwater intrusion scenarios for a coastal aquifer at the German North Sea. E3S Web of Conferences 54, 00031, DOI: 10.1051/e3sconf/20185400031, 2018.

/SCH 20/ Schneider, A., Britz, S., Gehrke, A., Kröhn, K.-P., Lampe, M., Nägel, A., Reiter, S., Wittum, G., Zhao, H.: Groundwater Flow and Transport in Complex Real Systems.FKZ 02 E 11476A-B (BMWK), final report, Gesellschaft für Anlagen- und Reaktorsicherheit (GRS) gGmbH, GRS-566, Braunschweig, 2020.

/SCH 20a/ Schön, T.: Kalibrierung von Grundwassermodellen mit freier Oberfläche. Master thesis, Goethe-Universität, Frankfurt am Main, 2020.

/SCH 22/ Schöniger, H. M., Langmann, T. et al.: Implementing strategic development goals in coastal aquifer management. Final report of the GRoW joint project go-CAM (BMBF, 02WGR1427B). https://bmbf-grow.de/de/system/files?file=document/Schlussbericht_%20go-CAM_final_reduziert.pdf (2022).

/SKB 06/ Svensk Kärnbränslehantering AB (SKB): Climate and climate-related issues for the safety assessment SR-Can. Technical report TR-06-23, Svensk Kärnbränslehantering AB, Stockholm, 2006.

/SRI 91/ Srivastava, R-, Yeh, TCJ. Analytical solutions for one-dimensional, transient infiltration toward the water table in homogeneous and layered soils. Water Resources Research 27(5):753–62, 1991.

/STA 17/ Deutscher Bundestag: Gesetz zur Suche und Auswahl eines Standortes für ein Endlager für hochradioaktive Abfälle (Standortauswahlgesetz - StandAG). Decision of the Deutscher Bundestag, 2017.

/STI 12/ Stichel, S., Logashenko, D., Grillo, A., Reiter. S., Lampe, M., Wittum, G.: Numerical Methods for Flow in Fractured Porous Media. In J. M. P. Q. Delgado (ed.), Heat and Mass Transfer in Porous Media, Advanced Structured Materials, Vol. 13, Springer-Verlag, 2012, pp. 83-113, DOI: 10.1007/978-3-642-21966-5_4

/VAN 80/ van Genuchten, M.Th. A Closed-form Equation for Predicting the Hydraulic Conductivity of Unsaturated Soils. Soil Science Society of America Journal 44(5):892–8, 1980.

/VAN 93/ Vandenberghe, J., Pissart, A.: Permafrost changes in Europe during the Last Glacial. Permafrost and Periglacial Processes 4, 121–135, 1993.

/VOG 13/ Vogel, A., Reiter, S., Rupp, M., Nägel, A., Wittum, G.: UG 4: A novel flexible software system for simulating PDE based models on high performance computers. Computing and Visualization in Science 16 (4): 165-179, 2013.

/WAS 10/ FEFLOW 6 User Manual. www.feflow.info DHI-WASY, Berlin, 2010.

/WER 08/ Werner, K., Öhman, J., Holgersson, B., Rönnback, K., Marelius, F.: Meteorological, hydrological, and hydrogeological monitoring data and near-surface hydrogeological properties data from Laxemar- Simpevarp, Site descriptive modelling SDM-Site Laxemar. SKB Report R-08-73, Svensk Kärnbränslehantering AB, Stockholm, 2008.

/WIT 89/ Wittum, G.: On the robustness of ILU-smoothing. SIAM J. Sci. Stat. Comput., 10, 699-717, 1989.

/WOL 18/ Wolf, J.: INIS - Verbundprojekt NAWAK - Entwicklung nachhaltiger Anpassungsstrategien für die Infrastrukturen der Wasserwirtschaft unter den Bedingungen des klimatischen und demografischen Wandels, Schlussbericht Teilvorhaben 1 (unveröffentlicht), FKZ 033W007A, 78, 79, 2018.

Table of figures

List of tables

HYMNE

Hydrogeological Modelling at a Regional Scale

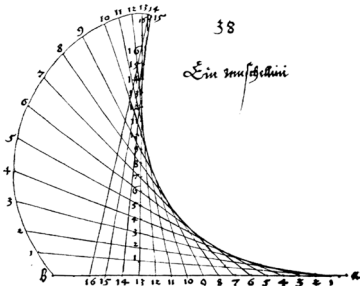

GRS - 750